University of Groningen

Semiconductor Nanoparticles Synthesized by Magnetron-Sputtering Inert Gas Condensation

Zhu, Xiaotian

IMPORTANT NOTE: You are advised to consult the publisher's version (publisher's PDF) if you wish to cite from it. Please check the document version below.

Document Version
Publisher's PDF, also known as Version of record

[Link to publication in University of Groningen/UMCG research database](#)

Semiconductor Nanoparticles Synthesized by Magnetron-Sputtering Inert Gas Condensation

For optoelectronic and phase-change applications

Xiaotian Zhu

university of
groningen

Semiconductor Nanoparticles Synthesized by Magnetron-Sputtering Inert Gas Condensation

For optoelectronic and phase-change applications

PhD thesis

to obtain the degree of PhD at the
University of Groningen
on the authority of the
Rector Magnificus Prof. C. Wijmenga
and in accordance with
the decision by the College of Deans.

This thesis will be defended in public on

Tuesday 28 September 2021 at 11.00 hours

by

Xiaotian Zhu

born on 17 July 1991
in Liaoning Province, China

Supervisors
Prof. G. Palasantzas
Prof. B.J. Kooi

Assessment Committee
Prof. M.A. Loi
Prof. M.A. Stöhr
Prof. H.J.W. Zandvliet

1

1

INTRODUCTION

1

Abstract

The quantum mechanical coupling of hundreds to thousands of atoms is necessary to develop the band structure of solid.[1] As bulk materials are scaled down to the nanoscale, novel properties can be expected, such as size-dependent band gap caused by quantum confinement effect[2], improved catalytic properties caused by the large surface area and rich surface structure[3], and plasmonic effects caused by localized collective electron oscillation[4]. In this regime, nanoparticles (NPs) are regarded as fundamental and functional building blocks of nanotechnology, providing appealing possibilities for the advancement of novel devices, such as tailoring the electronic structure without changing the chemical composition. This chapter is dedicated to the introduction of nanoparticle synthesis and possible applications relevant to the content of this thesis.

1.1 Synthetic method of semiconductor nanoparticles

1.1.1 Gas-phase routine

magnetron-sputter inert gas condensation

The cluster beam source based on magnetron sputtering has emerged as one of the feasible techniques for synthesizing ligand-free NPs, which enables the synthesis of various nanostructures not only single-element NPs but also multi-component NPs including nanoalloy[5] and phase-separated structures such as core/shell, core-satellite[6], and Janus NPs[7]. Typically, the magnetron-sputtering cluster source, which was developed by Haberland,[8] can be divided into five regimes. Initially, the supersaturation vapor of target atoms is formed by inert gas (generally Ar) sputtering facilitated with the magnetron. When the degree of supersaturation in the gas is sufficient, nucleation will occur, resulting in the formation of solid embryos. Since such embryos are thermodynamically unstable, further condensation with additional atoms leads to the formation of a stable cluster. When such clusters reach the critical size, coagulation of such clusters results in the formation of condensed nanoparticles. Subsequently, as a result of the pressure difference between the aggregation and deposition chambers, nanoparticles will expand through the aperture into the deposition chamber and land on the substrate. In this case, the desirable size of the nanoparticles can be achieved by interrupting the condensation process in the aggregation chamber, e.g. by tuning the gas flow driving the nanoparticles into the deposition chamber.

Figure 1.1 illustrates the schematic representation of an inert-gas condensation NP deposition system based on magnetron sputtering (Mantis Nanogen 50 deposition system), which generally can be divided into four parts including the aggregation zone, shell coater, quadrupole mass-filter (QMF), and the main deposition chamber.[9] In practice, one or more targets could be placed on the magnetron heads that are connected with the DC or RF source, where the aggregation length is adjustable by a linear translator mounted behind the

1

magnetron heads. To achieve the plasma, argon (Ar) gas, where the flow rate can be regulated by a mass flow controller, is pumped into the reactor and ionized into excited species (Ar^+) by the DC or RF source. Because of the magnetic field of the magnetron head, the plasma electrons are confined around the target surface area resulting in the enhancement of ionization for inert gas atoms (Ar). In this case, the dense gas ions (Ar^+) are accelerated to collide with the target surface, releasing free atoms and resulting in a supersaturated gas phase. As mentioned above, the free atoms from the target are then subjected to the creation of unstable seed nuclei, nucleation, and condensation to form the nanoparticles. Furthermore, the shell coater can post-modify the structure of nanoparticles, and the desired size of nanoparticles can be selected by the QMF. Specifically, a Si-core/ Ag-satellite hybrid structure was obtained by sputtering the Ag atoms in shell coater, which provides an additional degree of freedom in nanoparticle design.[10] If the charge is supposed to be carried by the nanoparticles in the beam, the mass, or the size of the nanoparticles can be selected by the inline QMF. The QMF consists of four cylindrical rods to which the electrical field pulses can be applied. Since the nanoparticle with different mass-to-charge ratios have different perpendicular velocities in the electrical field, the desired size of nanoparticles can be passed through the aperture by applying a certain electrical field, while the others deviate from their original trajectories and, as a result, are filtered out.[11]
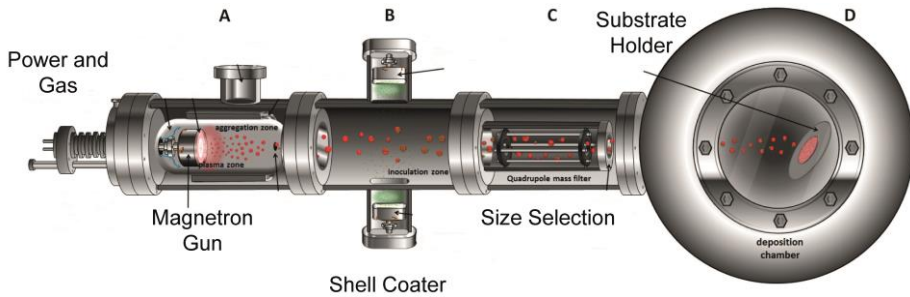
Figure 1.1 Schematic representation of magnetron-sputter inert-gas condensation NP deposition system. Adopted from Ref[9]

The main benefit of such synthesis route is its intrinsic flexibility. The size and crystalline state of as-deposited nanoparticles can be tuned by regulating the deposition parameters such as the magnetic field strength, gas flow rate, and magnetron power. In addition, the multi-component nanoparticles with tunable composition, sharpness, and crystallinity can be achieved by using section targets and multiple sputtering sources, opening up nearly unlimited possibilities for the design and facile synthesis of customized nanoparticles.[9] Moreover, since all synthetic procedures are performed in vacuum, it is consistent with current fabrication techniques for semiconductor nanocrystals (NCs). Also, in contrast to wet-chemical approaches, gas-phase synthetic methods are not constrained by the boiling point of the organic solvent, which can readily achieve the synthesis of materials with strong covalent bonding.

nonthermal plasma synthesis

Nonthermal plasma is an additional viable gas-phase synthesis technique for nanoparticles. The nonthermal plasmas are generated by applying an electric field to the rarified gas, which accelerates the electrons to high enough energies to electronically excite and ionize the surrounding gas atoms.[12] The energetic electrons then dissociate the gas precursor (SiH_4 and GeH_4) into the neutral and charged radicals, which can then be used for the formation of nanoparticles. In contrast to the typical plasma deposition techniques, the main

1

characteristics of nonthermal plasma are that the species in the plasma are in a non-equilibrium state. Specifically, the electrons in the nonthermal plasma are very 'hot', but the heavy species, such as ions, atoms, and molecules, remains at modest temperature.[13] In such a case, the formation of nanoparticles in nonthermal plasma can be attributed to the chemical nucleation process rather than the condensation from a supersaturated atomic vapor. Figure 1.2 displays the general design of a nonthermal plasma reactor for nanocrystal synthesis. Specifically, the quartz tube reactor is enclosed by a ring electrode pair that can be used in conjunction with a radiofrequency supply to dissociate the precursor gases into the radicals, and then the radical-nucleated nanocrystals pass through an orifice to the substrate. Various nanocrystals materials, including elemental[14] and alloy[15] group IV nanocrystals, doped group IV nanocrystals[16], and compound semiconductor nanocrystals[17], have been successfully synthesized using the nonthermal plasma method.
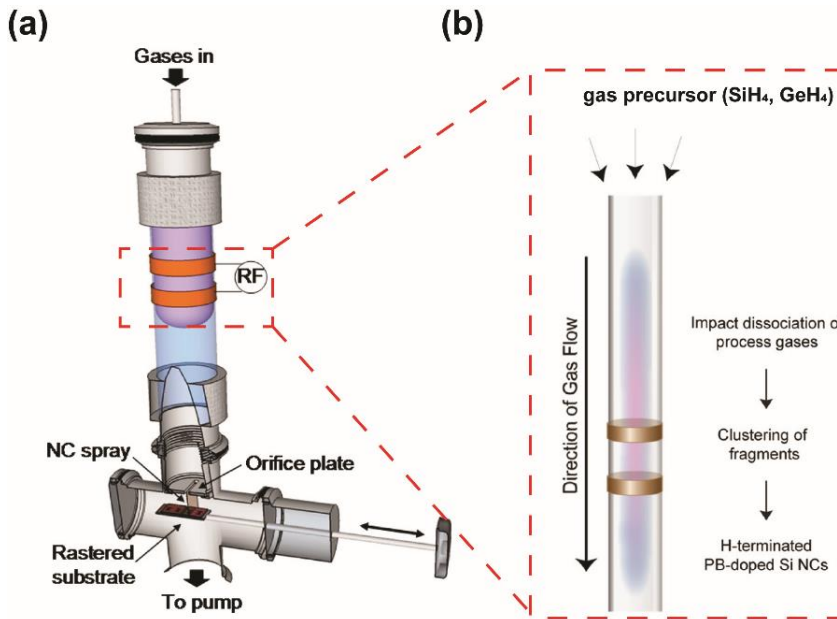
Figure 1.2 (a)Schematic representation of nonthermal plasma nanocrystal synthesis system and (b) detailed scheme of the reaction region of the system. Adopted from Ref.[18,19]

Aside from the benefits comparable to the inert-gas condensation method, such as solvent and ligand-free NP production, other appealing features include: charging of nanoparticles, which reduces or prevents nanoparticle agglomeration, and the large disparity between the chemical potentials of the gaseous growth species and the species attached to the nanoparticle surface, which facilitates doping of the NPs.[13] Furthermore, since the synthesis could be carried out at ambient pressure and room temperature, the apparatus based on the nonthermal plasma process can be comparatively straightforward as opposed to the magnetron-sputtering inert-gas condensation. Also, the syntheses yield of nonthermal plasma systems can be higher than that of the magnetron-sputtering inert-gas condensation technique, enabling for fabrication of nanoparticles-based devices. However, the synthetic precursors,

1

such as silane (SiH_4) and germane (GeH_4), for nonthermal plasma methods are toxic and costly, restricting the integration to modern industrial techniques.

1.1.2 Solution-phase processing

Since the solution-phase routine for nanoparticle synthesis is not the focus of this thesis, a brief introduction is given in this section, and in-depth reviews can be found elsewhere in the literature[20,21] for the interested reader. Solution-phase strategies for producing nanoparticles include metathesis, hydrolysis, thermal decomposition, and reduction in low and high temperatures. Colloidal solution-phase synthesis is the most fundamental synthetic method, aiming to control the divergent stages of nucleation from the resulting development of the embryonic particles (LaMer mechanism[22]) in the solution containing precursors. However, the colloidal synthesis of nanoparticles is heavily dependent on the advances of the requisite precursor chemistries, which results in vastly different synthetic conditions for the synthesis of different materials nanoparticles. For instance, due to the strong covalent Ge-Ge bond, a relatively high synthesis temperature is necessary to nucleate and crystallize the Ge nanocrystals, restraining the available organic solvent options. Furthermore, the ligands or organic solvents of nanocrystals may influence the understanding of the intrinsic properties of nanocrystals in certain cases. However, the scalable processing, readily modified surface of nanoparticles, and relatively simple apparatus are all benefits of solution-phase synthetic methods compared with gas-phase deposition methods.

1.2 Application of gas-phase nanoparticles

1.2.1 Infrared quantum dots

The quantum confinement effect, which allows the optical and electronic properties of semiconductor nanocrystals (NCs) to be tuned by controlling the size of NCs, has driven the development and exploration of semiconductor nanocrystals as emerging candidate materials for novel optoelectronic application such as light-emitting device (LED), photovoltaic cells, and

photodetectors.[23,24] In particular, infrared quantum dots (QDs) are the semiconductor nanocrystals with optical band gap energies in the infrared region of the electromagnetic spectrum, including near-infrared (NIR, 0.7 ~ 1.4 µm), short-wavelength infrared (SWIR, 1.4 ~ 3 µm), mid-wavelength infrared (MWIR, 3 ~8 µm), and long-wavelength infrared (LWIR, 8~ 15 µm), which can absorb or emit the infrared photons.[21] As it is shown in Figure 1.3 (a), the infrared QDs can be classified into the following groups based on elemental composition: group IV[25,26] (Si, Ge, GeSn), IV-VI[27] (PbS, PbSe, PbTe), III-V[28] (InAs), II-VI[29] (HgTe), I-VI[30] (Ag$_2$S, Ag$_2$Se), ternary I-III-VI[31] (CuInSe$_2$), and newly emerging metal-halide perovskite Cs$_x$FA$_{1-x}$PbI$_3$[32], where the tunable bandgap energies of these nanocrystals cover the infrared spectrum.

Quantum confinement refers to the effect that the exciton in semiconductor nanocrystals is squeezed when the size of nanocrystals is comparable with their exciton Bohr radius, resulting in the bandgap energy of the nanocrystals to be higher than that of the corresponding bulk materials. The energy of excitons in nanocrystals can be simply described by the particle-in-box model for which the ground state energy is

$$E_{box} = -\frac{\hbar^2 k^2}{2m^* a^2} \tag{1.1}$$

and m^*, a, $\hbar$, and k are the effective mass of the particle, the edge length of the box, reduced Planck constant, and wavenumber, repectively. Therefore, the conduction (E_c) and valence (E_v) band of the nanocrystals can be modified as:

$$E_c^{conf} = E_g + \frac{\hbar^2 k^2}{2m_e^* d^2} \tag{1.2}$$

$$E_v^{conf} = \frac{\hbar^2 k^2}{2m_h^* d^2} \tag{1.3}$$

where d (nm) is the diameter of the nanocrystals, E_g is the bandgap energy of the bulk materials, and the m_e^* and m_h^* are the effective mass of electrons and holes respectively. In this case, the bandgap energy of the nanocrystals can be expressed as:

1

$$E_g^{conf} = E_g + \frac{\hbar^2\pi^2}{2d^2}\left(\frac{1}{m_e^*} + \frac{1}{m_h^*}\right). \tag{1.4}$$

Equation (1.4) demonstrates that the bandgap energy of nanocrystals will be increased with the reduction of the NC's size. The Tight-binding (TB) model, as a semi-empirical method, has recently been shown to accurately predict the confinement bandgap energy for semiconductor nanocrystals, which can be applied for the calculation of the edge states of various nanostructures (films, wires, and dots), including the spin-orbit coupling.[33,34] The TB model fixes the particle-in-box model's overestimation of the bandgap energy for smaller nanocrystals, where electronic wave functions leakage outside the NC is more significant. Particularly, the TB model for the germanium (Ge) spherical nanocrystals is gives:

$$E_v(d) = E_{g(bulk)} + \frac{15143.8}{d^2 + 6.465d + 2.546}\ meV \tag{1.5}$$

$$E_c(d) = \frac{11863.7}{d^2 + 2.391d + 4.252}\ meV \tag{1.6}$$

where d *(nm)* is the diameter of Ge NCs.

Moreover, apart from the quantum confinement effect, the benefit of carrier multiplication or impact ionization for semiconductor nanocrystals, as shown in Figure 1.3(B), can increase the efficiency of NC-based solar cells by exploiting the extra energy of a hot photo-excited electron in generating a second electron-hole pair rather than heating the device.[35]

1
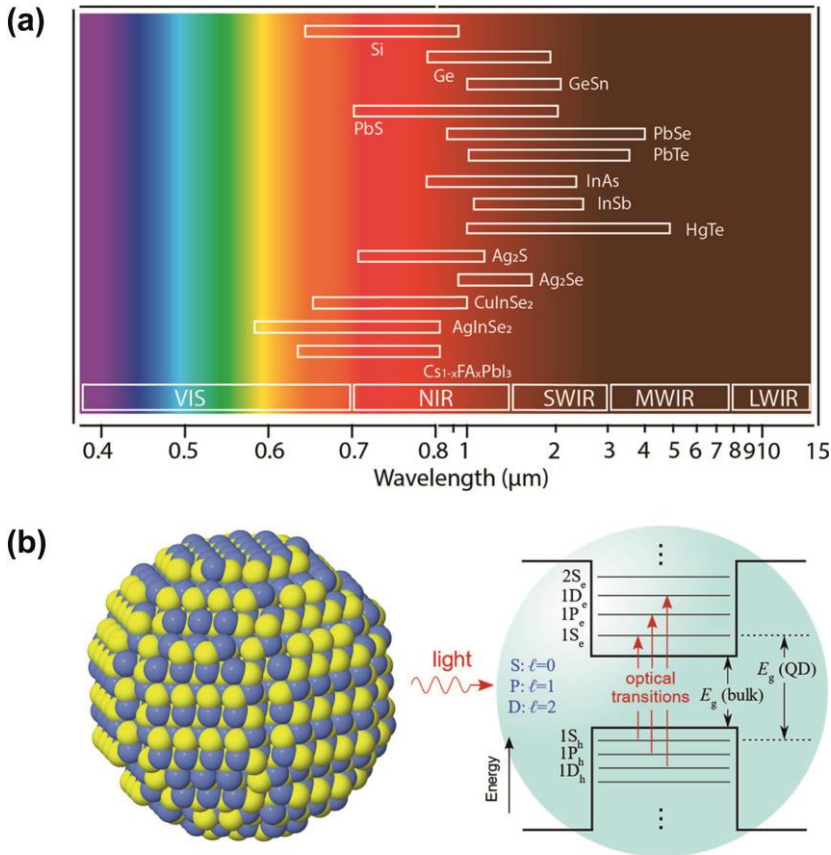
Figure 1.3 (a) Emission wavelength range of typical infrared nanocrystals, (b)scheme of the structure of nanocrystal and lowest electron and hole levels in nanocrystals. Adopted from Ref.[21,26]

Among the infrared semiconductors, due to the low toxic properties of group IV semiconductor materials (Si, Ge, and their alloys), the group IV nanocrystals have attracted interest for integration into the existing Si-based semiconductor industry. However, the nature of the indirect band structure for bulk Si and Ge hinders their application in optoelectronic and photonic devices.[36] Numerous theoretical studies indicate that an indirect-to-direct transition could be

1

achieved by quantum confinement[37] and alloying with tin (Sn)[38,39] . As it is shown in Figure 1.4, the following section is devoted to a brief overview of the group IV nanocrystals e.g. mode of Si, Ge, SiGe, and GeSn.

Firstly, silicon (Si) is the semiconductor material that has been most widely used in the semiconductor industry. However, due to the above-mentioned indirect band structure, Si is not widely known as an excellent optoelectronic material, and the efficiency of existing Si-based optoelectronic devices like solar cells has reached a bottleneck.[40] Nevertheless, the discovery of photo-luminescence from nano-crystalline Si reveals that the photo-electronic properties of Si can be improved by scaling down at the nanoscale.[41] After years of research, quantum confined Si NCs have been successfully synthesized by the gas-phase method. For instance, Zhao et al. reported that Si NCs with good size control could be deposited by magnetron-sputter inert gas condensation.[42]

Secondly, germanium, as another attractive semiconductor material, has been scaled down to a nanocrystal in 1982 by Hayashi et al, demonstrating that the optical properties of Ge are size-dependent.[43] Furthermore, since the Bohr exciton radius of Ge (~ 12 nm) is much larger than that of Si (~ 4 nm), which means that the quantum confinement effect can be readily accomplished in Ge, and the carriers mobility of Ge is also higher than that of Si[44], the Ge NCs have received increased attention as alternatives to existing optoelectronic devices.

To our knowledge so far, we were the first to demonstrate that magnetron-sputter inert gas condensation can be used to synthesize Ge NCs with tunable size. Finally, aside from manipulating the size of nanocrystals, alloying can smoothly vary the properties from those of one material to another by tuning the composition of nanocrystals.[45] In particular, since the separation between the indirect (L) and direct (Γ) valleys in the conduction band can be reduced by alloying Si and Ge with Sn, the direct bandgap structure could be achieved until the Sn content exceeds a certain level. However, since the binary phase diagrams of both Si-Sn and Ge-Sn reveal immiscibility over the entire composition range, the main difficulty of alloying group IV materials is to

develop a synthetic method to produce the desired structures. Due to its far-from equilibrium growth processing, it has been demonstrated that inert gas condensation based on magnetron sputtering can be a feasible synthesis method for immiscible elements.[7,46]
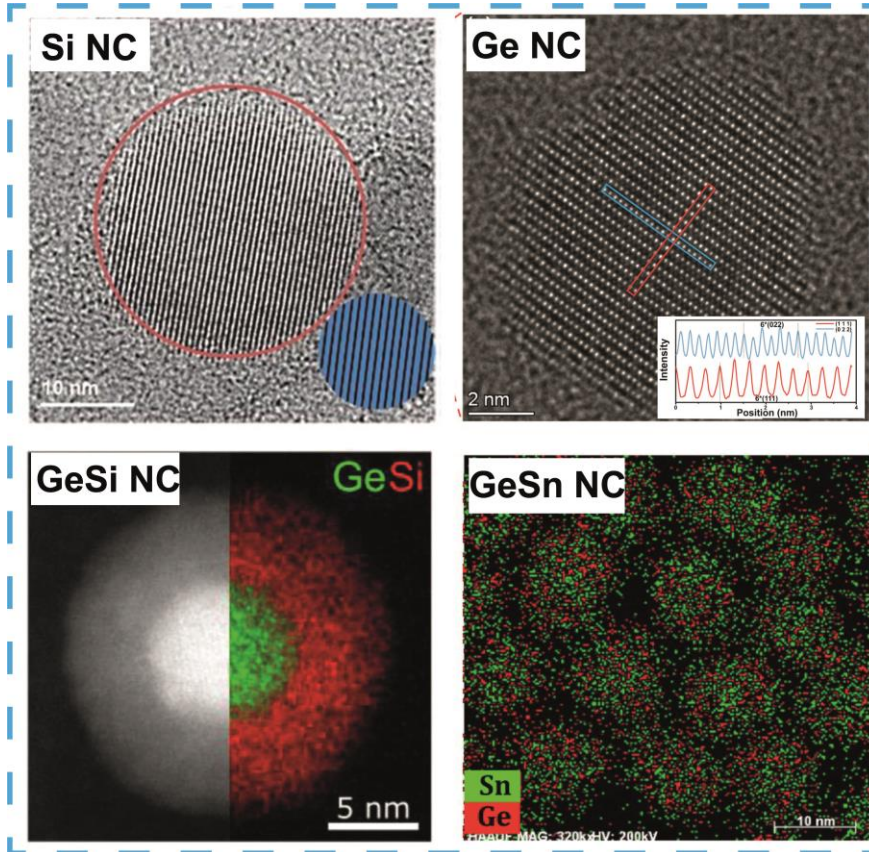

Figure 1.4 TEM images of typical Group IV nanocrystals. Adopted from Ref.[35,47–49]

1.2.2 Phase change materials

Typical phase change materials (PCMs) are those that have two relatively stable phases (although one is meta-stable), such as amorphous and crystalline

1

phases, which are widely used in data storage application. The following are the essential conditions for PCMs to be used in data storage: (1) distinct electrical and optical contrast between the amorphous and crystalline states; (2) high-speed crystallization for rapid memory switching at elevated temperature (e.g. nanosecond switching at 500 ℃); (3) good data retention, e.g. long thermal stability of the amorphous phase (e.g. 10 years at 80 ℃); (4) excellent endurance (high cyclicity, e.g. 10^8 times); (5) low melting temperature (e.g. 600 for low power switching between crystalline and amorphous phases) and (6) low threshold voltage switching for phase-change random access memory (PCRAM).[50] The demand for data storage and processing, which are generated by mobile electronics, high-definition video devices, and artificial intelligence, is growing at an unprecedented rate for such an information technology era.[51] Down-scaling the storing unit provides a promising method to increase the storage capacity, which will bridge the gap between the data generation and storage availability.[52] Furthermore, it offers more appealing device properties, such as high-speed switching and low power consumption per bit.[53] In this case, the gas-phase nanoparticles can be seen as the three-dimensional nanoscale model for studying the fundamental properties of phase-change materials. As it is shown in Figure 1.4, gas-phase GeSbTe nanoparticles with different sizes were deposited by magnetron-sputtering inert gas condensation, and the size-dependent crystallization temperature was characterized by in-situ transmission electron microscopy and differential scanning calorimetry (DSC), indicating a fragile-to-strong (FS) crossover of the as-deposited amorphous GST NPs in the super-cooled liquid state.[54,55]
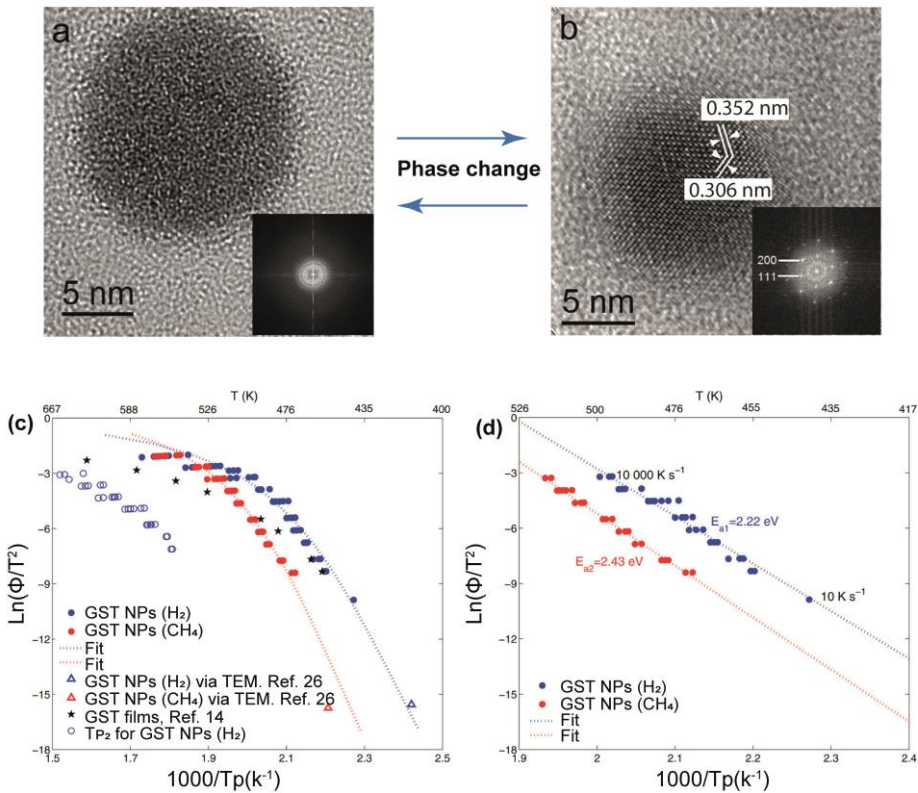
Figure 1.5 High-resolution TEM (HRTEM) images of the amorphous (a) and crystalline (b) $Ge_2Sb_2Te_5$ (GST) nanoparticles and insets are Fast Fourier transform images respectively. (c, d) Study of crystallization kinetics for different size GST nanoparticles. Adopted from Ref.[54,55]

1.3 Motivation and Thesis outline

Third-generation solar cells are devices that outperform the theoretical conversion efficiency limit for a single (bandgap) energy threshold material, known as Shockley-Queisser (SQ) limit. One of the technologies to address such issues is bandgap engineering in tandem or stacked cells. A promising approach here is to used nanoparticles (NPs). If the size of the NPs is less than its Bohr exciton radius (λ_B), the quantum confinement effect causes a band

1

widening for nanoparticles, which allows bandgap engineering. Germanium (Ge) nanocrystals (NCs) are attractive materials for optoelectronic applications because of their size-dependent optical properties. This also directly implies that a synthesis method that allows size and morphology control of the NCs is essential for further technology development and applications.

Understanding the size-dependent electronic properties of individual semiconductor nanocrystals (NCs) is important for designing novel nanoscale devices based on NCs. Therefore, the charge transfer that takes place at the interface between the NCs layer and carrier transportation layer of the device plays a crucial role in the overall efficiency of the device, which is affected by the Fermi level alignment between the different layers of the device. In this thesis, semiconductor nanoparticles has been used as a three-dimensional model to investigate the novel physical and chemical properties of semiconductor materials.

After this general introduction in Chapter 1, **Chapter 2** presents the general experimental techniques used in this thesis including (a) the magnetron-sputter cluster beam source for tunable size semiconductor nanoparticles deposition, (b) electron microscopy that was used to characterize structure, size distribution, and composition of as-deposited nanoparticles, and (c) scanning probe microscopy, specifically atomic force microscopy and Kelvin probe force microscopy, for measuring the size distribution and electrostatic properties of nanoparticles.

Chapter 3 illustrates a single step gas-phase processing route based on high-pressure magnetron sputtering for ligand-free and tunable size synthesis of Ge NCs. Furthermore, the as-deposited Ge NCs have been systematically characterized by High-Resolution Transmission Electron Microscopy (HRTEM), X-ray photoelectron spectroscopy (XPS), Raman spectroscopy, and Absorption spectroscopy. Consequently, the in-depth analysis of the high-resolution TEM data reveals the complete morphology of the as-deposited Ge NCs, which include single crystal, partially amorphous, polycrystalline NPs,

and NPs with an oxidation shell. The quantum confinement effect for Ge NCs was demonstrated by UV-vis-NIR absorption spectroscopy. The latter indicated that the bandgap of the Ge NCs, which was also modeled using both the effective mass and tight-binding models, was increased from ~ 0.8 to 1.1 eV for NC sizes in the range ~15 to 7 nm making them promising for a wide range of optoelectronic applications taking into account the comparisons with the theoretical models and other experimental results.

Chapter 4 presents an investigation of the electronic properties of individual Ge NCs with different sizes by Kelvin probe force microscopy (KPFM). Specifically, the size of as-deposited Ge NCs was tuned by helium gas flow rates and variable magnetic field configuration above the target surface during the deposition. Moreover, the effect of these two parameters on size control was discussed in detail from the perspective of the growth kinetics mechanism. The variation of local surface potential for different size Ge NCs deposited on n-type silicon substrate was measured by KPFM. The observed contact potential difference (CPD) of different size Ge NCs reveals the evolution of the Fermi level of the Ge NCs as a function of NCs size. Subsequently, based on quantum confinement theory, the disparity of the Fermi level between the Ge NCs and n-type silicon will decrease as the NC size reduced. Consequently, the amount of charge transferred from the substrate to the Ge NCs will decrease, which explains the observed experimental results very well.

Chapter 5 provides a proof-of-concept that the amorphous state of antimony (Sb) can be stabilized by scaling down to nanoscale in three-dimensional. In particular, synthesis by magnetron-sputtering inert gas condensation shows that the size and crystalline or amorphous phase of the Sb NPs can be tuned well. The phase states of as-deposited Sb NPs can be readily tuned by discharge current used in the nanocluster source, and as-deposited Sb NPs with crystalline and amorphous phase have a different shape as characterized by HRTEM. Furthermore, the diameter of Sb NPs decreases by reducing the discharge current. Finally, the crystallization temperature of as-deposited Sb

1

NPs was investigated by in-situ heating in TEM, which indeed proves that the stability of the amorphous phase of Sb can be significantly improved by nanoscale confinement.

Reference

 (1) Talapin, D. V.; Lee, J. S.; Kovalenko, M. V.; Shevchenko, E. V. Prospects of Colloidal Nanocrystals for Electronic and Optoelectronic Applications. *Chem. Rev.* **2010**, *110* (1), 389–458.

 (2) Li, L. S.; Hu, J.; Yang, W.; Alivisatos, A. P. Band Gap Variation of Size- and Shape-Controlled Colloidal CdSe Quantum Rods. *Nano Lett.* **2001**, *1* (7), 349–351.

 (3) Cargnello, M.; Doan-Nguyen, V. V. T.; Gordon, T. R.; Diaz, R. E.; Stach, E. A.; Gorte, R. J.; Fornasiero, P.; Murray, C. B. Control of Metal Nanocrystal Size Reveals Metal-Support Interface Role for Ceria Catalysts. *Science (80-.).* **2013**, *341* (6147), 771–773.

 (4) Wang, H.; Brandl, D. W.; Le, F.; Nordlander, P.; Halas, N. J. Nanorice: A Hybrid Plasmonic Nanostructure. *Nano Lett.* **2006**, *6* (4), 827–832.

 (5) Bohra, M.; Grammatikopoulos, P.; Singh, V.; Zhao, J.; Toulkeridou, E.; Steinhauer, S.; Kioseoglou, J.; Bobo, J.-F.; Nordlund, K.; Djurabekova, F.; et al. Tuning the Onset of Ferromagnetism in Heterogeneous Bimetallic Nanoparticles by Gas Phase Doping. *Phys. Rev. Mater.* **2017**, *1* (6), 066001.

 (6) Singh, V.; Cassidy, C.; Grammatikopoulos, P.; Djurabekova, F.; Nordlund, K.; Sowwan, M. Heterogeneous Gas-Phase Synthesis and Molecular Dynamics Modeling of Janus and Core-Satellite Si-Ag Nanoparticles. *J. Phys. Chem. C* **2014**, *118* (25), 13869–13875.

 (7) Krishnan, G.; Verheijen, M. A.; ten Brink, G. H.; Palasantzas, G.; Kooi, B. J. Tuning Structural Motifs and Alloying of Bulk Immiscible Mo−Cu Bimetallic Nanoparticles by Gas-Phase Synthesis. *Nanoscale* **2013**, *5* (12), 5375.

 (8) Haberland, H.; Mall, M.; Moseler, M.; Qiang, Y.; Reiners, T.; Thurner, Y. Filling of Micron-sized Contact Holes with Copper by Energetic Cluster Impact. *J. Vac. Sci. Technol. A Vacuum, Surfaces, Film.* **1994**, *12* (5), 2925–2930.

 (9) Grammatikopoulos, P.; Steinhauer, S.; Vernieres, J.; Singh, V.; Sowwan, M. Nanoparticle Design by Gas-Phase Synthesis. *Adv. Phys. X* **2016**, *1* (1), 81–100. https://doi.org/10.1080/23746149.2016.1142829.

 (10) Cassidy, C.; Singh, V.; Grammatikopoulos, P.; Djurabekova, F.; Nordlund, K.; Sowwan, M. Inoculation of Silicon Nanoparticles with Silver Atoms. *Sci. Rep.* **2013**, *3* (1), 3083.

 (11) Ganeva, M.; Peter, T.; Bornholdt, S.; Kersten, H.; Strunskus, T.; Zaporojtchenko, V.; Faupel, F.; Hippler, R. Mass Spectrometric Investigations of Nano-Size Cluster Ions Produced by High Pressure Magnetron Sputtering. *Contrib. to Plasma Phys.* **2012**, *52* (10), 881–889.

 (12) Kortshagen, U. Nonthermal Plasma Synthesis of Semiconductor Nanocrystals. *J. Phys. D. Appl. Phys.* **2009**, *42* (11), 113001.

 (13) Kortshagen, U. R.; Sankaran, R. M.; Pereira, R. N.; Girshick, S. L.; Wu,

1

J. J.; Aydil, E. S. Nonthermal Plasma Synthesis of Nanocrystals: Fundamental Principles, Materials, and Applications. *Chem. Rev.* **2016**, *116* (18), 11061–11127.

(14) Mangolini, L.; Thimsen, E.; Kortshagen, U. High-Yield Plasma Synthesis of Luminescent Silicon Nanocrystals. *Nano Lett.* **2005**, *5* (4), 655–659.

(15) Pi, X. D.; Kortshagen, U. Nonthermal Plasma Synthesized Freestanding Silicon-Germanium Alloy Nanocrystals. *Nanotechnology* **2009**, *20* (29), 295602.

(16) Stegner, A. R.; Pereira, R. N.; Klein, K.; Lechner, R.; Dietmueller, R.; Brandt, M. S.; Stutzmann, M.; Wiggers, H. Electronic Transport in Phosphorus-Doped Silicon Nanocrystal Networks. *Phys. Rev. Lett.* **2008**, *100* (2), 026803.

(17) Felbier, P.; Yang, J.; Theis, J.; Liptak, R. W.; Wagner, A.; Lorke, A.; Bacher, G.; Kortshagen, U. Highly Luminescent ZnO Quantum Dots Made in a Nonthermal Plasma. *Adv. Funct. Mater.* **2014**, *24* (14), 1988–1993.

(18) Holman, Z. C.; Kortshagen, U. R. A Flexible Method for Depositing Dense Nanocrystal Thin Films: Impaction of Germanium Nanocrystals. *Nanotechnology* **2010**, *21* (33), 335302.

(19) Limpens, R.; Pach, G. F.; Neale, N. R. Nonthermal Plasma-Synthesized Phosphorus-Boron Co-Doped Si Nanocrystals: A New Approach to Nontoxic NIR-Emitters. *Chem. Mater.* **2019**, *31* (12), 4426–4435.

(20) Carolan, D. Recent Advances in Germanium Nanocrystals: Synthesis, Optical Properties and Applications. *Progress in Materials Science*. Pergamon October 1, 2017, pp 128–158.

(21) Lu, H.; Carroll, G. M.; Neale, N. R.; Beard, M. C. Infrared Quantum Dots: Progress, Challenges, and Opportunities. *ACS Nano*. 2019, pp 939–953.

(22) Lamer, V. K.; Dinegar, R. H. Theory, Production and Mechanism of Formation of Monodispersed Hydrosols. *J. Am. Chem. Soc.* **1950**, *72* (11), 4847–4854.

(23) Nozik, A. J.; Beard, M. C.; Luther, J. M.; Law, M.; Ellingson, R. J.; Johnson, J. C. Semiconductor Quantum Dots and Quantum Dot Arrays and Applications of Multiple Exciton Generation to Third-Generation Photovoltaic Solar Cells. *Chem. Rev.* **2010**, *110* (11), 6873–6890.

(24) Dai, X.; Zhang, Z.; Jin, Y.; Niu, Y.; Cao, H.; Liang, X.; Chen, L.; Wang, J.; Peng, X. Solution-Processed, High-Performance Light-Emitting Diodes Based on Quantum Dots. *Nature* **2014**, *515* (7525), 96–99.

(25) Wolf, O.; Dasog, M.; Yang, Z.; Balberg, I.; Veinot, J. G. C.; Millo, O. Doping and Quantum Confinement Effects in Single Si Nanocrystals Observed by Scanning Tunneling Spectroscopy. *Nano Lett.* **2013**, *13* (6), 2516–2521.

(26) Zhu, X.; Ten Brink, G. H.; De Graaf, S.; Kooi, B. J.; Palasantzas, G. Gas-Phase Synthesis of Tunable-Size Germanium Nanocrystals by Inert Gas Condensation. *Chem. Mater.* **2020**, *32* (4), 1627–1635.

(27)   Hendricks, M. P.; Campos, M. P.; Cleveland, G. T.; Plante, I. J. La; Owen, J. S. A Tunable Library of Substituted Thiourea Precursors to Metal Sulfide Nanocrystals. *Science (80-.).* **2015**, *348* (6240), 1226–1230.

(28)   Franke, D.; Harris, D. K.; Chen, O.; Bruns, O. T.; Carr, J. A.; Wilson, M. W. B.; Bawendi, M. G. Continuous Injection Synthesis of Indium Arsenide Quantum Dots Emissive in the Short-Wavelength Infrared. *Nat. Commun.* **2016**, *7* (1), 12749.

(29)   Sagar, L. K.; Walravens, W.; Maes, J.; Geiregat, P.; Hens, Z. HgSe/CdE (E = S, Se) Core/Shell Nanocrystals by Colloidal Atomic Layer Deposition. *J. Phys. Chem. C* **2017**, *121* (25), 13816–13822.

(30)   Zhang, Y.; Hong, G.; Zhang, Y.; Chen, G.; Li, F.; Dai, H.; Wang, Q. Ag 2 S Quantum Dot: A Bright and Biocompatible Fluorescent Nanoprobe in the Second Near-Infrared Window. *ACS Nano* **2012**, *6* (5), 3695–3702.

(31)   Li, L.; Daou, T. J.; Texier, I.; Chi, T. T. K.; Liem, N. Q.; Reiss, P. Highly Luminescent Cuins 2/ZnS Core/Shell Nanocrystals: Cadmium-Free Quantum Dots for in Vivo Imaging. *Chem. Mater.* **2009**, *21* (12), 2422–2429.

(32)   Hazarika, A.; Zhao, Q.; Gaulding, E. A.; Christians, J. A.; Dou, B.; Marshall, A. R.; Moot, T.; Berry, J. J.; Johnson, J. C.; Luther, J. M. Perovskite Quantum Dot Photovoltaic Materials beyond the Reach of Thin Films: Full-Range Tuning of A-Site Cation Composition. *ACS Nano* **2018**, *12* (10), 10327–10337.

(33)   Niquet, Y. M.; Allan, G.; Delerue, C.; Lannoo, M. Quantum Confinement in Germanium Nanocrystals. *Appl. Phys. Lett.* **2000**, *77* (8), 1182–1184.

(34)   Niquet, Y.; Delerue, C.; Allan, G.; Lannoo, M. Method for Tight-Binding Parametrization: Application to Silicon Nanostructures. *Phys. Rev. B - Condens. Matter Mater. Phys.* **2000**, *62* (8), 5109–5116.

(35)   Efros, A. L.; Brus, L. E. Nanocrystal Quantum Dots: From Discovery to Modern Development. *ACS Nano* **2021**, *15* (4), 6192–6210.

(36)   Doherty, J.; Biswas, S.; Galluccio, E.; Broderick, C. A.; Garcia-Gil, A.; Duffy, R.; O'Reilly, E. P.; Holmes, J. D. Progress on Germanium−Tin Nanoscale Alloys. *Chem. Mater.* **2020**, *32* (11), 4383−4408.

(37)   Takagahara, T.; Takeda, K. Theory of the Quantum Confinement Effect on Excitons in Quantum Dots of Indirect-Gap Materials. *Phys. Rev. B* **1992**, *46* (23), 15578–15581.

(38)   Lee, M. H.; Liu, P. L.; Hong, Y. A.; Chou, Y. T.; Hong, J. Y.; Siao, Y. J. Electronic Band Structures of Ge1-XSnx Semiconductors: A First-Principles Density Functional Theory Study. *J. Appl. Phys.* **2013**, *113* (6), 63517.

(39)   Demchenko, D. O.; Tallapally, V.; Esteves, R. J. A.; Hafiz, S. din A.; Nakagawara, T. A.; Arachchige, I. U.; Ozgur, U. Optical Transitions and Excitonic Properties of Ge 1-x Sn x Alloy Quantum Dots. *J. Phys. Chem. C* **2017**, *121* (33).

(40)   Ni, Z.; Zhou, S.; Zhao, S.; Peng, W.; Yang, D.; Pi, X. Silicon Nanocrystals: Unfading Silicon Materials for Optoelectronics. *Materials Science and*

1

Engineering R: Reports. Elsevier Ltd October 1, 2019, pp 85–117.

(41) Pavesi, L.; Dal Negro, L.; Mazzoleni, C.; Franzò, G.; Priolo, F. Optical Gain in Silicon Nanocrystals. *Nature* **2000**, *408* (6811), 440–444.

(42) Zhao, J.; Singh, V.; Grammatikopoulos, P.; Cassidy, C.; Aranishi, K.; Sowwan, M.; Nordlund, K.; Djurabekova, F. Crystallization of Silicon Nanoclusters with Inert Gas Temperature Control. *Phys. Rev. B* **2015**, *91* (3), 035419.

(43) Hayashi, S.; Ito, M.; Kanamori, H. Raman Study of Gas-Evaporated Germanium Microcrystals. *Solid State Commun.* **1982**, *44* (1), 75–79.

(44) Kamata, Y. High-k/Ge MOSFETs for Future Nanoelectronics. *Materials Today*. Elsevier January 1, 2008, pp 30–38.

(45) Erogbogbo, F.; Liu, T.; Ramadurai, N.; Tuccarione, P.; Lai, L.; Swihart, M. T.; Prasad, P. N. Creating Ligand-Free Silicon Germanium Alloy Nanocrystal Inks. *ACS Nano* **2011**, *5* (10), 7950–7959.

(46) Krishnan, G.; de Graaf, S.; ten Brink, G. H.; Persson, P. O. Å.; Kooi, B. J.; Palasantzas, G. Strategies to Initiate and Control the Nucleation Behavior of Bimetallic Nanoparticles. *Nanoscale* **2017**, *9* (24), 8149–8156.

(47) Kabashin, A. V.; Singh, A.; Swihart, M. T.; Zavestovskaya, I. N.; Prasad, P. N. Laser-Processed Nanosilicon: A Multifunctional Nanomaterial for Energy and Healthcare. *ACS Nano*. American Chemical Society September 24, 2019, pp 9841–9867.

(48) Hunter, K. I.; Held, J. T.; Mkhoyan, K. A.; Kortshagen, U. R. Nonthermal Plasma Synthesis of Core/Shell Quantum Dots: Strained Ge/Si Nanocrystals. *ACS Appl. Mater. Interfaces* **2017**, *9* (9), 8263–8270.

(49) Ramasamy, K.; Kotula, P. G.; Fidler, A. F.; Brumbach, M. T.; Pietryga, J. M.; Ivanov, S. A. Sn_xGe_{1-x} Alloy Nanocrystals: A First Step toward Solution-Processed Group IV Photovoltaics. *Chem. Mater.* **2015**, *27* (13), 4640–4649.

(50) Lencer, D.; Salinga, M.; Wuttig, M. Design Rules for Phase-Change Materials in Data Storage Applications. *Adv. Mater.* **2011**, *23* (18), 2030–2058.

(51) Zhang, W.; Mazzarello, R.; Wuttig, M.; Ma, E. Designing Crystallization in Phase-Change Materials for Universal Memory and Neuro-Inspired Computing. *Nat. Rev. Mater.* **2019**, *4* (3), 150–168.

(52) Hamann, H. F.; O'Boyle, M.; Martin, Y. C.; Rooks, M.; Wickramasinghe, H. K. Ultra-High-Density Phase-Change Storage and Memory. *Nat. Mater.* **2006**, *5* (5), 383–387.

(53) Xiong, F.; Liao, A. D.; Estrada, D.; Pop, E. Low-Power Switching of Phase-Change Materials with Carbon Nanotube Electrodes. *Science (80).* **2011**, *332* (6029), 568–570.

(54) Chen, B.; Ten Brink, G. H.; Palasantzas, G.; Kooi, B. J. Crystallization Kinetics of GeSbTe Phase-Change Nanoparticles Resolved by Ultrafast Calorimetry. *J. Phys. Chem. C* **2017**, *121* (15), 8569–8578.

(55) Chen, B.; Ten Brink, G. H.; Palasantzas, G.; Kooi, B. J. Size-Dependent and Tunable Crystallization of GeSbTe Phase-Change Nanoparticles. *Sci. Rep.* **2016**, *6* (1), 39546.

1

2

EXPERIMENTAL METHODS

2

Abstract

This chapter outlines the techniques utilized for the synthesis of nanoparticles, and the subsequent experimental methods employed for sample characterization and data processing. Nanoparticles were deposited by a cluster source that combined high pressure magnetron sputtering and inert gas condensation. Transmission electron microscopy (TEM) and scanning probe microscopy (SPM) were used to determine the morphology, structure, and electrostatic properties of nanoparticles.

2.1 Nanoparticles Synthesized by Inert Gas Condensation

Since the basics of nucleation and cluster growth during inert gas condensation have been introduced in chapter 1, this section focuses on the nanoparticles deposition system employed in this thesis, which is a home-modified Nanosys50 from Mantis Deposition Ltd. The instrumental system, as depicted in Figure 2.1, consists of two chambers: the aggregation chamber where magnetron sputtering, nucleation and cluster growth occur, and the main chamber where the as-synthesis nanoparticles can be deposited on substrates. In addition, a quartz crystal microbalance (QCM) is installed inside the main chamber to track the yield of nanoparticle deposition by measuring the frequency shift of the QCM. Two Leybold turbo molecular pumps with a capacity of 300 lt/s are employed to evacuate the two chambers, and a Varian LTH 100 scroll vacuum pump is used to back the evacuation. The main and aggregation chamber can reach pressures of 1×10^{-8} and 1×10^{-6} mbar, respectively, and the pressure value can be read on the Mantis controller (Figure 2.1(b)).
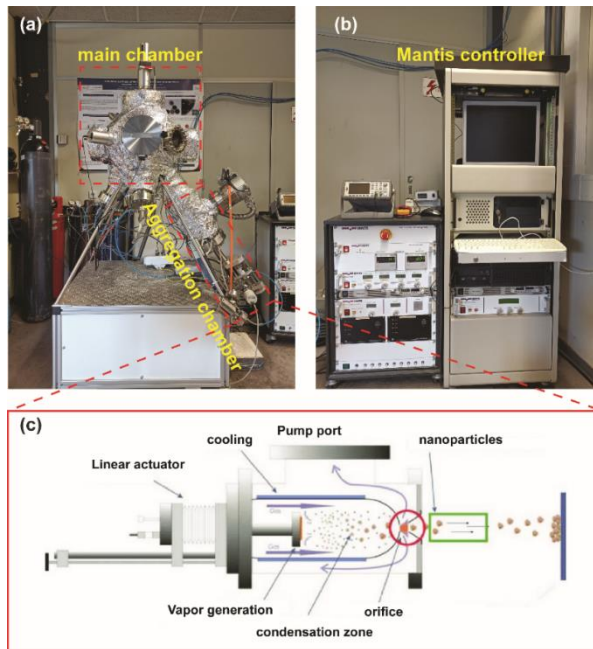
2

27

2

Figure 2.1 The nanoparticle deposition system (a), and the associated controller (b). (c) schematically illustration of aggregation chamber.

The magnetron sputtering system, as illustrated in Figure 2.1 (c), consists of the following components: a magnetron head, a double gas inlet system, water cooling system for both the magnetron head and the aggregation chamber wall. The magnetron employs disk plane targets that are 2 inches in diameter, with an anode that is mounted on top and connected to a TDK-Lambda Genesys Gen 600-1.3 programmable DC power supply with a range of up to 600 V and 1.3 A. A programmable DC voltage is applied between the cathode (target) and the anode (copper cap), and the discharge power is adjustable using a built-in voltage and current limiter.

As supersaturation is reached, nucleation and cluster growth occurs resulting in the formation of nanoparticles with the desired size. Due to the differential pressure between the two chambers, the as-synthesized nanoparticles are transported by the inert gas flow to the main chamber and land on the

substrates. Though adjusting the deposition parameters, the size of as-deposited nanoparticles can be easily controlled. According to our observation, using helium gas as a drift gas and copper backing plates to tune the strength of the magnetic field we can achieve a significant effect on size of the as-deposited nanoparticles. The reason is that helium gas has a lower viscosity than argon, which improves transportation efficiency. Since a thick backing plate can result in a weaker magnetic field of magnetron, which cause a lower ionization and higher diffusion rate of atoms away from the plasma region, the sputtering can be accomplished at a low rate with the sparse plasma leading to smaller in size nanoparticles. In addition, the crystalline structure of as-deposited nanoparticles can also be controlled by adjusting the deposition parameters.

2.2 Transmission Electron Microscopy

Transmission Electron microscopy (TEM) is a very powerful technique for the local analysis of nanostructure, chemical composition, and crystallography of materials. Compared with optical microscopy, the illumination source of TEM generates electrons of which the wavelength is much shorter (e.g. 2.5 pm at 200 kV) than the wavelength of visible light (400 – 700 nm), which in principle, allows to resolve the sub-nanoscale structure of materials based on the Rayleigh criterion. Nevertheless, the practical spatial resolution of TEM cannot reach the fundamental diffraction limit ($0.61\lambda/\sin\alpha$ with λ the wave length of the electrons used and α the half opening angle of the objective lens used) due to several aberrations. According to the geometry of the lens, the monochromatic aberration of microscopy can be divided into spherical aberration, coma, astigmatism, field curvature, and distortion. Among these aberrations, the spherical aberration of the electromagnetic lens is the most effective factor limiting the resolution of TEM, since it cannot be readily corrected by combining negative and positive lens like in (visible) light microscopy. The spherical aberration of a TEM could not be corrected until the

design of the hexapole spherical aberration corrector proposed by Beck.[1] After that, the development of the hexapole corrector system allowed TEMs to reach the sub-Angstrom resolution.[2,3] Also, modern TEMs can be integrated with other spectroscopies such as energy dispersive x-ray spectroscopy (EDS) and electron energy loss spectroscopy (EELS), which can be used to determine the local chemical composition of materials. In addition, the invention of cryogenic TEM (cryo-TEM) extended the application of TEM to the biology.

2.2.1 The theory of beam interaction with the specimen

As it is shown in Figure 2.2, various signals can be generated by the interactions between the incident electron beam with the atoms of the specimen, which is known as electron scattering. These signals can be divided into two categories, elastically scattered electrons and inelastically scattered electrons, based on energy loss after the interaction. The elastically scattered electrons, which consist of direct transmission electrons, coherent elastic scattered electrons, and incoherent elastic scattered electrons, refer to the electrons with constant velocity and wavelength. For conventional TEM which used the plane wave as the illumination source, imaging is primarily performed by the elastically scattered electrons. On the contrary, the inelastically scattered electrons refer to both the energy and direction that have been changed after the interaction, in which the loss energy can be used to generate characteristic X-ray, secondary electrons, Auger electrons, and backscattered electrons. In particular, the characteristic X-ray generated from the interaction can be exploited in X-ray energy dispersive spectrometry (EDS) for determining the composition of samples. Also, the energy loss of the inelastically scattered electrons can be measured by an electron spectrometer to form the electron energy loss spectrum (EELS), which can interpreted in terms of inelastic interactions including phonon excitations, band transitions, and plasmon excitations.
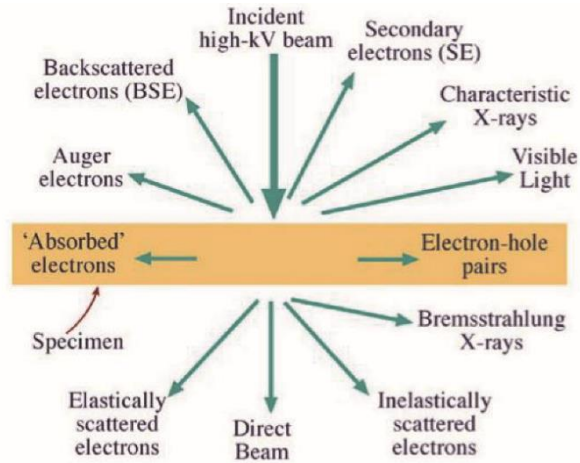
Figure 2.2 Different kinds of signals generated after the interaction between the electrons with a thin specimen. Adapted from Williams and Carter.[4]

2.2.2 Operation Modes

As shown in Figure 2.3, the TEM can be operated in two typical modes: transmission mode and scanning transmission mode. In transmission mode, which also refers to the conventional TEM (left panel of Figure 2.3), electrons generated from the electron gun and accelerated by the high-tension voltage are adjusted into a parallel beam wave above the sample surface by a series of condenser lenses. After illuminating the thin sample, the incident plane wave is converted into the exit wave, which is subsequently magnified by the objective lens and a set of projection lenses, and forms the final image on the charge-coupled device (CCD) camera. Correspondingly, in scanning transmission mode, also known as the scanning transmission electron microscopy (STEM), the incident electron beam will be formed into a tiny illuminating spot by several condenser lenses, which are generally known as the electron probe. The electron probe can scan over the sample surface in a raster fashion by a pair of scanning coils, in which the incident electron probe will be scattered by the sample. As shown in Figure 2.3 (right panel), various

signals (intensities) generated by the scattering of the electrons can be collected at different angle ranges in the far-field diffraction plane and displayed as a function of the probe location.[5]
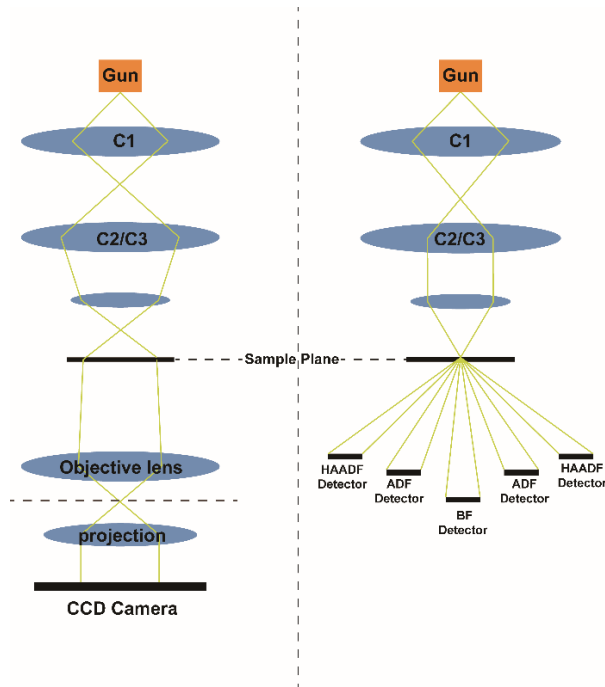

Figure 2.3 Schematic diagram of conventional TEM (left panel) and STEM (right panel) modes in TEM.

The theory of STEM mode

In STEM mode, the size of the converging electron probe, which is constrained by the condenser lens and aperture, determines the spatial resolution limit of the microscopy.[5] The wave function of the electron probe formed by the condenser lens without any aberration can be described as:

$$\varphi_{probe}(x) = FT\big(\varphi_{in}(\boldsymbol{k})\big) \tag{2.1}$$

$$\varphi_{in}(\boldsymbol{k}) = A(\boldsymbol{k}) \times I_0(\boldsymbol{k}) \tag{2.2}$$

where the $\boldsymbol{k}$ is the wave vector in reciprocal space, $A(\boldsymbol{k})$ is the aperture function,

φ_{in} describes the wave function of incident wave and $I_o(\mathbf{k})$ describes the parallel electron wave and FT the representative Fourier transform. In this case, the size of the electron probe can be decreased by increasing the size of the condenser aperture, which results in the decrease of the depth of focus. Due to the presence of aberrations, the wave function of the electron probe is modified to:

$$\varphi_{probe}(\mathbf{x}) = FT\left[\varphi_{in}(\mathbf{k}) \times \exp\left(i\chi(\boldsymbol{\omega})\right)\right] \tag{2.3}$$

where the $\chi(\omega)$ describes the aberration function and $\omega = \lambda\,\mathbf{k}$. Based on the common notation, the aberration function ($\chi(\omega)$) in terms of ω and its complex conjugate $\bar{\omega}$ can be written as:

$$\chi(\omega) = Re\{\frac{1}{2}\omega\bar{\omega}C_1 + \frac{1}{2}\bar{\omega}^2 A_1 + \omega^2\bar{\omega}B_2 + \frac{1}{3}\bar{\omega}^3 A_2 + \frac{1}{4}(\omega\bar{\omega})^2 C_3 + \omega^3\bar{\omega}S_3$$
$$+ \frac{1}{4}\bar{\omega}^4 A_3 + \omega^3\bar{\omega}^2 B_4 + \omega^4\bar{\omega}D_4 + \frac{1}{5}\bar{\omega}^5 A_4 + \frac{1}{6}\omega\bar{\omega}^3 C_5 + \frac{1}{6}\bar{\omega}^6 A_5$$
$$+ \cdots\}$$

where the index of each coefficient is the order of the corresponding ray aberration instead of wave aberration.[6] For instance, C_1 and C_3 correspond to the amount of defocus and spherical aberration, respectively. Figure 2.4 illustrates the phase changes induced by individual axial aberration coefficients up to the fifth order. In practice, the ideal phase from 0 to $\pi/4$ ($\pi/4$-limit), which is the tabular region in the phase plates, will be selected by using the effective condenser aperture.
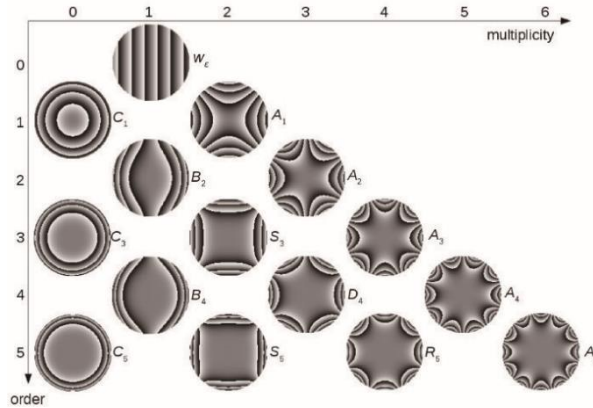
2

Figure 2.4 The simulation results of the phase variation of the electron beam caused by different order aberration, adapted from[7].

In contrast with conventional TEM, the image in STEM mode can be formed by collecting scattered electrons at various angles ranges with different detectors, which do not need the "post-specimen" lenses for image magnification. Since not a parallel but strongly converged beam is used, extended diffraction disks instead of sharp diffraction spots are generated. The non-diffracted beam generates the so-called bright-field (BF) disk. According to the collecting angle of the detectors, the types of images can be listed as follows:

(i)   BF imaging in which the transmitted electrons within the BF disk are collected.

(ii)   Annular dark-field (ADF) image, which is formed by collecting electrons at relatively high scattering angles beyond the BF disk. Where the angles exceed 60 mrad, it is commonly referred to as a high angle annular dark-field (HAADF) image.

(iii)   Annular bright-field (ABF) image, which excludes the center electrons of the BF disk as compared to the BF model.

Since the HAADF mode of STEM is the most popular and widely used approach for imaging, we will go over it in detail below. In HAADF mode, the image is

produced by collecting electrons of Rutherford scattering from the nucleus by thermally diffusing. The classical intensity of Rutherford scattering can be expressed as:

$$\sigma_R(\theta) = \frac{e^4 Z^2}{16(4\pi\varepsilon_0 E_0)^2 sin^2 \frac{\theta}{2}} d\Omega \qquad (2.5)$$

Where σ_R is the scattering cross section, E_o is the energy of the incident electron, Z is the atomic number of the atoms in the sample, θ is the scattering angle of the electron, ε_o is the vacuum permittivity, and Ω is the solid angle. As a result, the contrast of the image is proportional to the Z^2, which commonly refers as the Z contrast imaging. Due to screening of the nucleus by the surrounding core electrons the Z^2 dependence can readily transform into a $Z^{1.7}$ dependence.

Moreover, since the image is incoherent, it has all concomitant benefits as in classic (visible) light microscopy, as being independent from variation of specimen thickness or microscopy defocus, making the interpretation of image easier, and capable of achieving a higher resolution than the point resolution in phase-contrast imaging. The easier interpretation implies that in atomic resolution HAADF-STEM atoms are always bright in a dark surrounding, with the brightness scaling with the average $Z^{1.7-2}$ of the imaged atomic columns. In contrast, in atomic resolution TEM atomic columns can be both brighter or darker than the surrounding or can be even off-centered with respected to the maxima or minima in intensity depending on microscope defocus, specimen thickness and specimen structure.

The theory of high-resolution TEM (HR-TEM)

Unlike the incoherent imaging method like HAADF-STEM, HR-TEM imaging is a phase-contrast image formed by interference between transmission electrons and diffraction electrons selected by the objective aperture, which shows the phase differences originating from the interaction between the incident beam and the specimen. The imaging process can be considered as the

propagation of the electron wave function. After the interaction with the thin sample, the electron exit wave ($\varphi_{exitwave}$) can be described as:

$$\varphi_{exitwave}(\boldsymbol{r}) = \varphi_0 \exp\left[-i\sigma_c\phi_p(\boldsymbol{r})\right] \qquad (2.6)$$

Here, φ_o is the incident electron wave function, and ϕ_p is the projected potential in the *z*-direction which is parallel to the incident electron beam and perpendicular to the thin sample, σ_c is the interaction constant, and $\boldsymbol{r}$ is the *x, y* position in the sample.

When the sample is thin enough, the amplitude variation can be neglected (so-called *weak phase object approximation*). In this case, the $\varphi_{exitwave}$ can be simplified to:

$$\varphi_{exitwave} = 1 - i\sigma_c\phi_p(\boldsymbol{r}) \qquad (2.7)$$

Then the wave function as seen in the image can be given as

$$\varphi_{image}(\boldsymbol{r}) = \varphi_{exitwave} \otimes h(\boldsymbol{r}) \qquad (2.8)$$

where the *h(r)* is the point-spread function. The spatial frequencies in the diffraction plane can be expressed as:

$$\Psi_{image}(\boldsymbol{u}) = \Psi_{exitwave}(\boldsymbol{u}) \times H(\boldsymbol{u}) \qquad (2.9)$$

Here the *H(**u**)* is the contrast transfer function (CTF) and **u** is the reciprocal-lattice vector. The Ψ_{image}*(**u**)* and $\Psi_{exitwave}$*(**u**)* representative the Fourier transform of φ_{image}*(**r**)* and $\varphi_{exitwave}$*(**r**)* respectively. The CTF can be written as

$$CTF(\boldsymbol{u}) = A(\boldsymbol{u})E(\boldsymbol{u})\sin\left(\chi(\boldsymbol{u})\right) \qquad (2.10)$$

where *A(**u**), E(**u**), and χ(**u**)* are the aperture function, envelop function, and aberration function, respectively. And the *sin(χ(u))*, which is affected by spherical aberration and defocus, determines the spatial resolution of the final image. As shown in Figure 2.5, the contrast of the HR-TEM image can be inverted by adjusting the defocus. Since the bright or dark spot in the final HR-TEM image do not directly represent the positions of the atomic column, the image simulation is necessary for the interpretation of the final image.
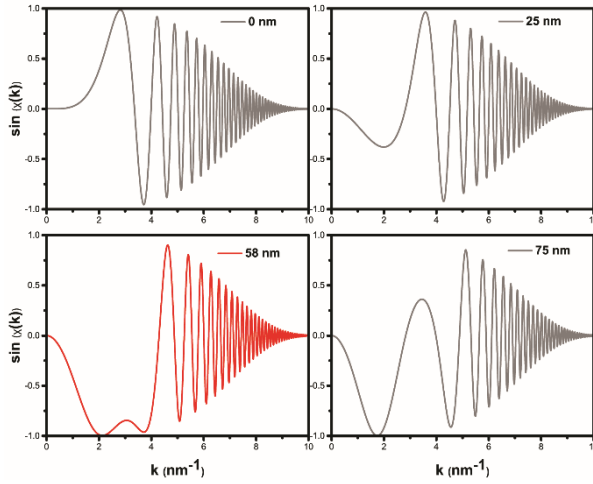
Figure 2.5 the contrast transfer function for a JEOL 2010F TEM operating at 200 kV for various microscope defocus values. The CTF in case of optimum defocus (which is about 1.2 times Scherzer defocus) is shown by red line. In this case a largest possible pass band in spatial frequencies between about 2 and 4 nm^{-1} has an absolute $\sin(\chi(\mu))$ value that is larger than 0.7. The associated first cross-over through the $\sin(\chi(\mu))=0$ axis is a direct measure of the point resolution of the microscope.

2.3 Scanning Probe Microscopy (SPM)

Similar to optical microscopy, the electron microscopy described above collects various signals from the interaction between the electron beam wave and the specimen to create an image, which enhances our ability to 'see' the objects in nano/atomscales. Nevertheless, SPM refers to a branch of microscopy that employs a sharp tip to 'feel' the tip-sample interaction and generate the image of the object in nanoscale ranges.

Scanning tunneling microscopy (STM) invented by G. Binnig et al. in 1982[8], is the first practice of this approach, which detected the tunneling current between the tip and sample and create the topographical image as a function

2

of the tip position. Furthermore, the density of states of the specific position can be obtained by sweeping the bias voltage, which refers to the scanning tunneling spectroscopy. However, according to the theory of the STM, the sample should be conductive in order to generate the tunneling current between the tip and sample, limiting the scope of application. In this case, G. Binnig et al[9] ulteriorly developed the atomic force microscopy (AFM) for imaging the surface of both conducting and insulating samples at the atomic scale. Since the tip of the AFM measures the forces of atoms between the sample and tip rather than the tunneling current in STM, it overcomes the conductive limit of materials. Also, the AFM can be applied to obtain the topographic image of the sample in not only ambient but also liquid environments. Besides, by measuring other interactions between the tip and sample, such as electrostatic forces and magnetic forces, Kelvin probe force microscopy (KPFM) and magnetic force microscopy (MFM) were also developed.

2.3.1 Atomic Force Microscopy (AFM)

The probes of AFM are made of a flexional cantilever with a sharp tip at the end of the cantilever that senses the forces exerted on the tip by the atoms of the sample surface. Since the curvature of the tip is generally from a few nanometers to tens of nanometers and the thermal vibration of the tip, it is relatively hard to obtain atomic resolution in an ambient environment. The cantilever is a critical component for imaging, as it needs to detect minor inter-atomic forces while avoiding the external disturbance from the surroundings. Figure 2.6(a) illustrates the schematic of AFM operation, which can be divided into five main parts including probe, scanner, position-sensitive photodetector (PSPD), feedback and control systems, and computer. Firstly, the sample will be approached by the piezo scanner in proximity to the sharp tip of the cantilever. After reflected by the backside of the cantilever, the focused beam can be detected by the PSPD, which is very sensitive to the position of the laser. Secondly, the probe and sample are driven by the piezo scanner relative to each

other in a raster pattern. The cantilever will be displaced by the atomic forces during the scanning, and such displacement will be amplified by the laser lever and recorded by a segmental photodetector. The differential signal compared with the setpoint is converted to a topographic map of the sample. Finally, the feedback system will move the piezo scanner to maintain the applied force.
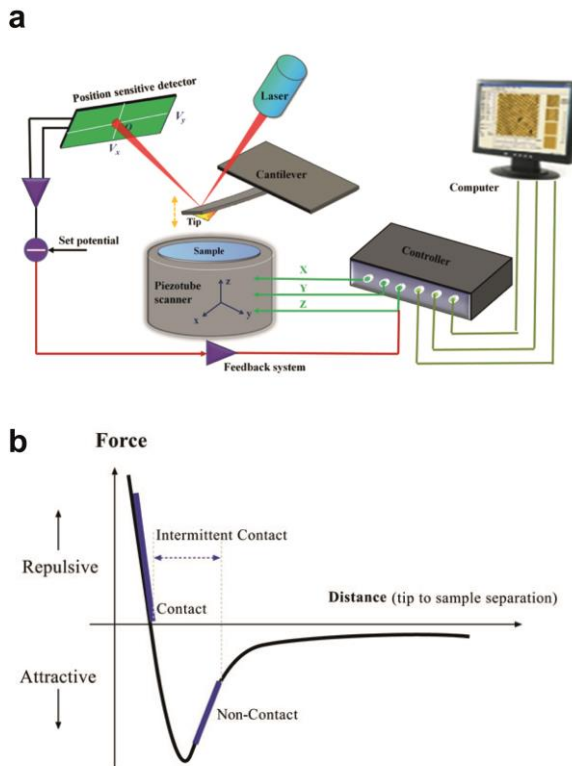
Figure 2.6 (a) Schematic of typical AFM system including the light source, cantilever, and photodetector. (b) Force vs. distance curve highlighting the specific region of different modes. Adapted from[10]

The relationship between the force and distance is depicted in Figure 2.6 (b). With the distance between two atoms decrease, the force will be changed from long-range attractive force to short-range repulsive force. According to the

different force region of the tip and sample during the operation, the AFM operation can be divided into two scanning modes: contact mode and dynamic mode. The difference between these two modes will be discussed below.

2.3.2 Imaging modes

Contact mode

The contact mode is the most basic model for AFM and also the foundation for understanding the additional modes like scanning capacitance mode (SCM). During the operation in contact mode, the tip of the cantilever makes contact with the surface of the sample and the applied atomic forces of the cantilever maintained in the repulsive force region. As a result, the cantilever will be bent upwards. According to Hooke's law, the amount of displacement of the cantilever is proportional to the applied force. As the schematic force-distance curve depicts in Figure 2.7, the cantilever is firstly brought close to the sample surface by the z-piezo until the tip of the cantilever can be attracted to the surface by atomic force (step 1 in Figure 2.7). The important occurrences of the force curve are steps 2 and 4, in which the interaction force between tip and sample is not balanced with the restoring force of the cantilever. The imaging in contact mode is accomplished by simply maintaining the setpoint (point 3 in the force curve) constant during the raster scanning between the tip and sample, where the topography of the sample can be obtained by plotting the displacement of the z-piezo as a function of the x-y position.

The benefits of contact mode can be summarized as 1. The resolution of the contact mode is higher than the tapping mode; 2. Contact mode is suitable for measuring the sample with large terraces and corrugations on the surface; 3. Since the contact mode is static, the feedback system is relatively easy during the scanning. However, there are some noticeable drawbacks for contact mode: 1. The image will be distorted due to the presence of lateral force during the operation. 2. The contact mode is undesirable for measuring soft materials like biological samples, as the sample will be damaged by the normal force and
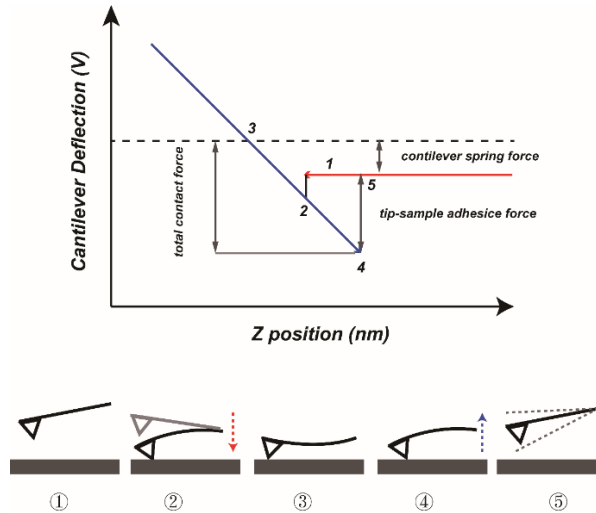
lateral force.

Figure 2.7 The force-distance curve in contact mode of AFM. The approach and withdrawal step were colored by red and blue respectively.

Tapping mode

To address the drawbacks of the contact mode and maintain the high lateral resolution, the tapping mode, which operated in both the repulsive and attractive force region, was developed.[11] During the operation, an AC voltage is applied to the piezo for oscillating the cantilever close to its resonance frequency. The average oscillation amplitudes are in the tens of nanometers, which is very small in comparison to the length of the cantilever. As shown in Figure 2.8, when the tip of the cantilever encounters the heigh changes of the sample surface, the oscillation amplitude of the cantilever would be perturbed due to the atomic forces, which can be detected by the PSPD. The signal generated by the PSPD will be processed by PID (Proportion, integral, derivative) control system. And then, a voltage would be applied to the piezo scanner, making the position of the scanner to be adjusted in the z-direction. When the oscillation amplitude of the cantilever is set back to the setpoint, the

displacement of the scanner would be recorded and displayed as a function of the x-y position of the scanner.
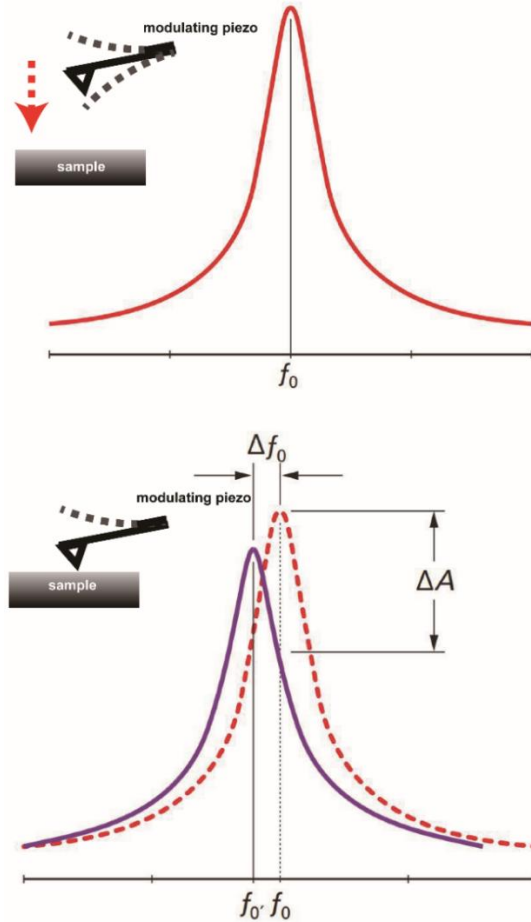
Figure 2.8. Resonance curve of the cantilever in tapping mode of AFM.

Compared with the contact mode, the tapping mode has the following advantages: 1. Since the intermittent contact between the tip and the sample surface of the tapping mode eliminates the influence of the lateral force, no damage occurs during the imaging process. 2. The interaction force between the tip and sample surface can be minimized, which is better for imaging soft materials. 3. The lateral resolution is better than the contact mode. The main

disadvantages are as follows: 1. As a consequence of processing the dynamics of the cantilever, the feedback loop is complex than the contact mode. 2. It is hard to operate in a liquid environment and under high vacuum.

2.3.3 Kelvin Probe Force Microscopy (KPFM)

Kelvin method

The Kelvin method was firstly developed by Lord Kelvin in 1898, which measures the work function difference of the two metals.[12] As it is shown in Figure 2.9 (top panel), when two different metals electrically contact, because of the difference of their work function, electrons will flow from the metal with the lower function to the metal with the higher work function before the Fermi levels line-up to form a steady state, which leads to a contact potential difference (CPD). The CPD is proportional to the work function difference (Φ_A-Φ_B) and can be expressed as:

$$V_{CPD} = \frac{\Phi_A - \Phi_B}{e} \tag{2.11}$$

Where the Φ_A, Φ_B, and e are the work function of two contact materials and the charge of an electron. If an external voltage (V_c) is applied to the system, which realigns their vacuum level back to the same level, the V_c is equal to the V_{CPD}. In this case, if we know the work function of one side (Φ_A), the work function of the other metal could be calculated as $\Phi_B = \Phi_A - eV_c$.

In the Kelvin method, in order to decide whether the vacuum level is aligned, two metal plates are placed in parallel to form a parallel plate capacitor. Consequently, a wire is used to contact them, and the current can be detected by an amperemeter due to the difference of the Fermi levels. After the realignment of their Fermi level, a constant CPD can be formed between them. When the capacitance between two metal plates varies as the distance changes, the amount of charge carried by two plates varies as the potential difference between two plates remains constant, allowing the current to pass through the amperemeter. If one side of the capacitor is fixed and the other side vibrates with the frequency *f*, then the capacitance of the capacitor varies sinusoidally,

where an AC with the frequency f can be detected by an amperemeter. Then a reverse applied potential (V_c) to the metal plates nullifies the contact potential difference between the plates.

The theory of KPFM

KPFM was developed by Nonnemacher et al. based on the Kelvin theory in 1991.[13] In general, KPFM operates in the non-contact mode, with a capacitor forming between the tip and sample surface. Simultaneously, the CPD would be formed between the tip and sample surface by electrical grounding. In this case, the long-range electrostatic force forms between the tip and sample and it can be expressed as:

$$F_e = -\frac{\partial U}{\partial z} = -\frac{1}{2}\frac{\partial C}{\partial z}(\Delta V)^2 \qquad (2.12)$$

where the U is the potential energy of the capacitor, z is the distance between the tip and sample surface, C is the capacitance, and ΔV represents the value of the CPD. According to the Kelvin theory, an adjustable DC voltage would be applied to compensate for the CPD formed between the tip and sample. In the meantime, to accurately determine whether the CPD is compensated, an AC voltage with the frequency ω is applied to the tip. Consequently, the potential between the probe and sample can be described as:

$$\Delta V = V_{CPD} - V_{DC} - V_{AC}\sin(\omega t). \qquad (2.13)$$

And the long-range electrostatic force (F_e) can be expressed as:

$$F_e = F_{DC} + F_\omega + F_{2\omega} \qquad (2.14)$$

where F_{DC} is the electrostatic force caused by the DC voltage, and F_ω and $F_{2\omega}$ are the electric forces with frequency ω and 2ω caused by the AC voltage. These three forces can be respectively expressed as:

$$F_{DC} = -\frac{1}{2}\frac{\partial C}{\partial z}\left[(V_{DC} - V_{CPD})^2 + \frac{1}{2}V_{AC}^2\right] \qquad (2.15)$$

$$F_\omega = -\frac{\partial C}{\partial z}(V_{DC} - V_{CPD})V_{AC}\sin(\omega t) \qquad (2.16)$$

$$F_{2\omega} = \frac{1}{4}\frac{\partial C}{\partial z}V_{AC}^2\cos(2\omega t) \qquad (2.17)$$

Under these three electrostatic forces, the kinetics' parameters (including amplitude A, frequency ω, and phase φ) of the AFM probe would be changed. The topographic image and the image of the CPD will be formed simultaneously by processing the different parts of the error signals generated from the changes of the kinetics' parameter. Since only the F_ω term includes the factor (V_{DC}-V_{CPD}), the F_ω will be equal to zero after nullifying the CPD. As a result, the CPD image of the sample could be measured by adjusted the V_{DC} to nullified A_ω. Since compensation of the CPD is achieved by detecting the amplitude A_ω of the cantilever, it is referred to as amplitude modulation KPFM (AM-KPFM).
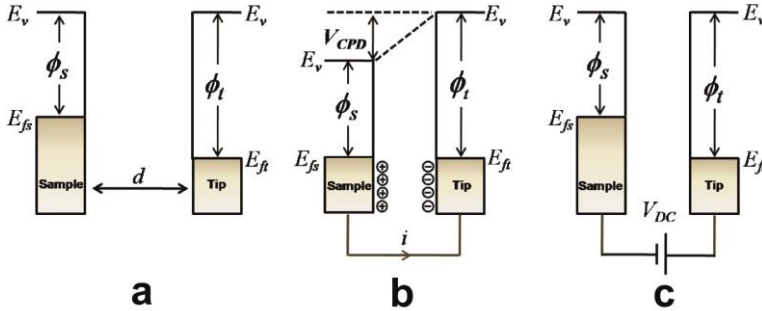

Figure 2.9. (a-c) The theory of Kelvin's methods for measurement of CPD. Adapted from ref[14]

2

Reference

(1) Beck, V. D. Hexapole Spherical Aberration Corrector. *Opt.* **1979**, *53* (4), 241–255.

(2) Rose, H. Correction of Aperture Aberrations in Magnetic Systems with Threefold Symmetry. *Nucl. Instruments Methods* **1981**, *187* (1), 187–199.

(3) Haider, M.; Rose, H.; Uhlemann, S.; Schwan, E.; Kabius, B.; Urban, K. A Spherical-Aberration-Corrected 200kV Transmission Electron Microscope. *Ultramicroscopy* **1998**, *75* (1), 53–60.

(4) Williams, D. B.; Carter, C. B. *Transmission Electron Microscopy: A Textbook for Materials Science*; 2009; Vol. 1–4.

(5) Nellist, P. D.; Pennycook, S. J. The Principles and Interpretation of Annular Dark-Field Z-Contrast Imaging. *Adv. Imaging Electron Phys.* **2000**, *113* (C), 147–203.

(6) Uhlemann, S.; Haider, M. Residual Wave Aberrations in the First Spherical Aberration Corrected Transmission Electron Microscope. *Ultramicroscopy* **1998**, *72* (3–4), 109–119.

(7) Hartel, P.; Linck, M.; Kahl, F.; Müller, H.; Haider, M. On Proper Phase Contrast Imaging in Aberration Corrected TEM. *Microsc. Microanal.* **2014**, *20* (S3), 926–927.

(8) Binnig, G.; Rohrer, H.; Gerber, C.; Weibel, E. Surface Studies by Scanning Tunneling Microscopy. *Phys. Rev. Lett.* **1982**, *49* (1), 57–61.

(9) Binnig, G.; Quate, C. F.; Gerber, C. Atomic Force Microscope. *Phys. Rev. Lett.* **1986**, *56* (9), 930–933.

(10) Maghsoudy-Louyeh, S.; Kropf, M.; Tittmann, B. R. Review of Progress in Atomic Force Microscopy. *Open Neuroimag. J.* **2019**, *12* (1), 86–104.

(11) Zhong, Q.; Inniss, D.; Kjoller, K.; Elings, V. B. Fractured Polymer/Silica Fiber Surface Studied by Tapping Mode Atomic Force Microscopy. *Surf. Sci. Lett.* **1993**, *290* (1–2), L688–L692.

(12) Kelvin, Lord. V. Contact Electricity of Metals. *London, Edinburgh, Dublin Philos. Mag. J. Sci.* **1898**, *46* (278), 82–120.

(13) Nonnenmacher, M.; O'Boyle, M. P.; Wickramasinghe, H. K. Kelvin Probe Force Microscopy. *Appl. Phys. Lett.* **1991**, *58* (25), 2921–2923.

(14) Melitz, W.; Shen, J.; Kummel, A. C.; Lee, S. Kelvin Probe Force Microscopy and Its Application. *Surface Science Reports*. Elsevier B.V. January 1, 2011, pp 1–27.

3

Gas-Phase Synthesis of Tunable-Size Germanium Nanocrystals by Inert Gas Condensation

3

Published as:
Chemistry of Materials 32.4 (2020): 1627-1635.

Abstract

Size-dependent optical properties of germanium (Ge) nanocrystals (NCs) make them as a desirable material for optoelectronic applications. So far, the synthesis of ligand-free and tunable-size Ge NCs by inert gas condensation has been scarcely reported. In this work, we introduce a gas-phase approach to synthesize quantum-confined Ge NCs by inert gas condensation, where the size of the Ge NCs can be readily tuned by controlling the thickness of a Cu plate supporting the Ge target. As explained by simulations using the finite element method, the magnetic field configuration above the target can be manipulated by varying the thickness of the Cu backing plate. In-depth analysis based on transmission electron microscopy (TEM) results reveals the morphology and crystalline structure of Ge NCs. X-ray photoelectron spectroscopy has proven the formation of a substoichiometric Ge oxide shell for the as-deposited Ge NCs. In addition, Raman spectroscopy indicated peak shifts according to the phonon confinement model that yielded nanoparticle sizes in good agreement with the TEM results. Furthermore, the quantum confinement effect for Ge NCs was demonstrated by analysis of the absorption (UV-vis-NIR) spectrum, which indicated that the band gap of the Ge NCs was increased from ~ 0.8 to 1.1 eV with decreasing size of Ge NCs. Comparison with theory shows that the quantum confinement effect on the band gap energy for different-size Ge NCs follows the tight-binding model rather well.

3.1 Introduction

Nowadays, semiconductor nanocrystals (NCs) with size less than the Bohr exciton radius, or quantum dots (QDs) as they are called in the literature, have gained strong interest due to the dependence of their physical properties on the so-called quantum confinement effect, where the band gap energy of the materials can be engineered by the size reduction of the NCs.[1] Based on size-dependent optical and electrical properties, semiconductor NCs are emerging candidates that enable a wide range of important applications, e.g., solar cells,[2] light emitting devices,[3] and photodetectors[4]. Although the binary II-VI, IV-VI, and III-V semiconductor nanocrystals are well developed and remain at the forefront of several developing technologies, the group IV semiconductor NCs have also attracted strong attention as potential alternatives, leading to intense research. The main interest arises from the fact that, in contrast to several quantum dot systems that contain toxic elements, as, for example, Cd and Pb, group IV semiconductor NCs are environmentally friendly and cost efficient.[5] In addition, group IV semiconductor NCs (Si and Ge) are compatible with the current CMOS processing based on Si technology.[6] Although Si remains of high interest for optoelectronics applications, germanium (Ge) is especially attractive due to: (i) the narrower bulk band gap energy (0.67 eV at 300 K) that implies possible tuning to specific wavelengths over a wide range (as much as 3.3 eV); (ii) the relatively larger Bohr exciton radius (~24 nm) than that of Si (4.5 nm) that translates to quantum confinement effects for larger NCs than Si NCs; (iii) the significant potential for indirect to direct (or quasi-direct) transitions that could be achieved at nanoscale ranges; (iv) a larger dielectric constant and a large absorption coefficient (~2×10^5 cm^{-1} at 2 eV)[7], and (v) carrier multiplication for approximately 5-6 nm Ge NCs.[8]

The strategies to synthesize Ge NCs can be clearly grouped into two major categories: solution-phase and gas-phase routes. In recent years, many solution-phase methods, including Zintl salts,[9] sol-gel process,[10,11] microwave-

3

assisted colloid reduction,[12–14] reduction of GeI$_2$[15] and solution-phase thermal decomposition[16,17] have been reported. However, in contrast to the gas-phase methods, the production of high-quality group IV NCs has been proven to be difficult by solution-phase methods[18,19]. One of the main reasons is the high crystallization temperature of Ge NCs due to the strong covalent bonding of Ge[20], which means that the choice of organic solvents will be limited by their boiling point[21]. In addition, in some cases, the use of strong reducing agents (e.g., NaBH$_4$, and LiAlH$_4$ superhydrides), which are environmentally unfriendly, cannot be avoided.[21] Another issue is the use of surfactants, which serves as a stabilizer of NCs in the solution. Moreover, since these organic surface ligands can also produce photoluminescence, the interpretation of the band gap energy from photoluminescence spectra can, in some cases, conceal the genuine signal originating from the size effect of the semiconductor NCs.[21,22] To our knowledge, only a few works have shown that the energy of the photoluminescence peak increases with decreasing size of the Ge NCs', which is induced by the quantum confinement effect instead of surface ligands.[23–26] In contrast, the gas-phase routes are not limited by any use of organic solvents, reducing agents, and surfactants, which is desirable for green and high-purity synthesis of NCs. Overall, the advantages of the gas-phase method are: (i) readily synthesizing NCs for high covalent materials like Si and Ge; (ii) excluding the use of solvents and ligands; (iii) easily achieving size control. A wide variety of possibilities are available for the gas-phase synthesis of NCs[27], such as cluster beam deposition[28–30], nonthermal plasma[31,32], laser pyrolysis[33], and thermal plasmas[34]. Recently, several advances have emerged from gas-phase synthesis of NCs from the IV group via nonthermal plasma[35,36]. In this case, the size of Ge NCs could be controlled by varying the flow rate and employing a Grignard reaction that allowed the surface passivation with alkyl groups instead of Cl groups. Ge NCs with different sizes demonstrated tunable band gap photoluminescence due to the quantum confinement effect.[23]

Besides the nonthermal plasma method, the cluster beam deposition is as a

promising method for the synthesis of high-quality semiconductor NCs. In particular, the inert gas method based on high-pressure magnetron sputtering[30] has emerged as one of the most versatile approaches to control the particle formation processes, where, especially, the size distribution can be tuned by the dynamical parameters of the magnetron source, such as the magnetic field configuration, power, flow of inert gas (Ar, He), and length of the aggregation zone[37]. However, the literature for utilizing the cluster source in the synthesis of semiconductor NCs still remains rather limited since only a few publications[38,39] so far have reported this possibility for semiconductor QDs. Nevertheless, the main deficiency of current research is on how to control the morphology of the semiconductor nanoparticles, since they often adopt a "cauliflower" structure. Although such structures consist of smaller nanoparticles, they do not agree with monodisperse and size-tunable semiconductor NCs and are therefore less suited for optoelectronic applications requiring high-quality semiconductor QDs.

Therefore, significant progress is required toward the size and morphology control of Ge NCs via the gas-phase synthesis based on high-pressure magnetron sputtering.[30] Hence, in this work, we report a gas-phase synthesis based on high pressure magnetron sputtering that provides Ge NCs with 100 % tunable size, ranging from 14.7 to 7.1 nm, enabling significant band gap engineering. For this purpose, we studied extensively the influence of backing plates of different thickness on the magnetic strength above the Ge target surface, where the main focus is on size-tunable synthesis of Ge NCs. The finite element method (FEM) was used to simulate the magnetic field distribution, suggesting that the magnetic field strength above the target surface decreases with increasing thickness of the backing plate, enabling the desired size tuning of the Ge NCs. This strategy eliminates the need for quadrupole mass filter (QMF) to achieve size selection and thereby significantly increases the effective yield of nanoparticles out of the system. Furthermore, it will be shown that the as-deposited Ge NCs have a monodisperse and uniform size distribution with

a band gap that widens with decreasing size as expected from quantum confinement calculations.

## 3.2 Experimental and Simulation Methods

Synthesis of Ge NCs: The Germanium (Ge) nanocrystals (NCs) with different sizes were deposited on transmission electron microscopy (TEM) grids by a home-modified nanoparticle deposition system Nanogen 50 obtained from Mantis Deposition Ltd. (www.mantisdepositon.com). The main chamber, where the samples are placed, was initially evacuated to a base pressure of ~ 1×10^{-8} mbar. The supersaturated Ge vapor was produced by sputtering the Ge target (50.8 mm diameter, 3 mm thickness, purity of 99.99%) with a 20 sccm Ar gas flow (purity 99.9999%) and 0.20 A discharge current. The supersaturated vapor was then cooled by Ar gas to form nuclei, which can subsequently grow into nanoparticles. The formed NCs in the aggregation chamber were then carried by the Ar gas to the sample chamber. For nanoparticles of different sizes, various copper backing plates (diameter 50.8 mm and thickness varying between 1.5 and 6 mm) were used as a separation between the Ge target and the magnetron head. The latter can adjust the magnetic field strength on the target surface, where sputtering takes place. To synthesize a large amount of NCs for further characterization, the precleaned glass substrate was put close to the aperture at the exit of the aggregation chamber.

Materials Characterization: The morphology, size distribution, and electron diffraction of the as-deposited NCs were analyzed by transmission electron microscopy (TEM, JEOL 2010) operated at 200 kV. High-resolution TEM (HRTEM) was performed with a probe- and image-corrected Thermo Fisher Scientific™ Themis Z S/TEM operating at 300 kV. The high-angle annular dark-field scanning transmission electron microscopy (HAADF-STEM) images were recorded with a convergence semiangle of 21 mrad and a beam current of 50 pA. The composition of NCs was further characterized by X-ray

photoelectron spectroscopy (XPS, Surface Science SSX-100 ESCA instrument) with a monochromatic Al K_α X-ray source (hv=1486.6 eV) operating at a base pressure of ~ 5×10^{-10} mbar. The NCs were directly deposited on a substrate coated by 150 nm thick film of gold. The electron takeoff angle with respect to the surface normal was 37°, the diameter of the analyzed area was 1000 μm, and the total experimental energy resolution was set to 1.16 eV. The XPS spectra were analyzed by the least-squares curve fitting program (Winspec, developed at the LISE laboratory of the University Notre-Dame de la Paix, Namur, Belgium). The binding energies (BEs) are reported with a precision of ±0.1 eV, and referenced with respect to the C 1s (BE = 285.6 eV) photoemission peak. Finally, Raman spectra were collected from NCs films deposited on silicon substrates. The Raman spectra were recorded on a Raman microscope (Thorlabs HNL) using the 632 nm line of a He-Ne laser as the excitation wavelength, at approximately 2.5 mW in the range 200-2000 cm^{-1}. The optical absorption of the NCs was obtained by the Shimadzu UV3600 spectrometer. In order to avoid the thickness effect in further measurements, the samples for both Raman spectra and UV-vis-NIR spectroscopy were deposited simultaneously to keep the same deposition conditions.

Finite Element Method (FEM) simulation. The magnetic field configuration and the race track, which develops during sputtering on the Ge target, were modeled by the finite element method (FEM) via the commercial software COMSOL Multiphysics. The magnetic and electric field module of COMSOL Multiphysics was adopted for simulating the magnetic field of the cluster source for the modified nanoparticle deposition Nanogen 50. The magnetic flux densities and the magnetic field strength $B_{//}$ ($\sqrt{B_x^2 + B_y^2}$) were calculated from the simulation results, with the XY plane considered parallel to the target surface. Moreover, the configuration and materials of the simulation model were assigned with the corresponding value of the specific cluster source, and the ambient condition was set as the vacuum. The exterior boundary condition in this simulation was used as the zero magnetic scalar

53

potential condition. To get an accurate simulation, a particularly fine mesh was selected for the magnetron source. Since the nonmagnetic Ge target was used for deposition, the shape and strength of the magnetic field configuration cannot be influenced. Therefore, the magnetic flux densities ($B_{//}$) on the target surface were calculated based on the total thickness (target and backing plate) above the copper shield of the magnetron head (Scheme 1).
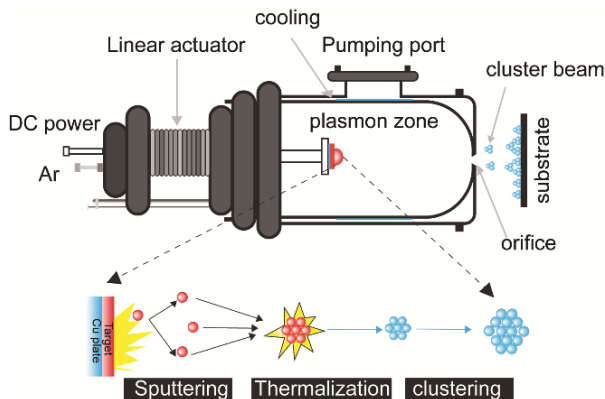
Scheme 3.1 Schematic diagram of the cluster deposition source for Ge NCs as based on high pressure magnetron sputtering.

3.3 Results and discussion

3.3.1 Morphology and Size Control of Ge NCs.

Figure 3.1 (a-d) shows bright-field TEM images of differently sized Ge NCs, which exhibit isolated pseudospherical structures. The corresponding size distribution analysis is shown in the insets of Figure 3.1 (a-d), which demonstrates that the average size can be tuned from 14.7 to 7.1 nm by varying the thickness of the backing plate. The reason for the size tunability of the NCs is that the backing plate thickness directly affects the plasma density, which is strongly related to the NCs growth rate. Any change in the backing plate distance between the target and magnetron effectively changes the magnetic field strength of the magnetron. During magnetron sputtering, as it is shown

in Scheme 3.1, plasma confinement is achieved above the target surface with the help of the magnetron. In the plasma region, collisions between electrons and gas atoms (Ar or He) result in the ionization of the sputtering gas forming excited species (Ar^+ or He^+). Subsequently, the accelerated gas ions impact on the Ge target, resulting in the emission and formation of the cluster seed that strongly affects the cluster production rate and size[40]. Since a stronger magnetic field confinement results in higher ionization, and a lower diffusion rate of atoms away from the source region, the sputtering can be achieved at a high rate with the dense plasma, leading to larger cluster sizes [41]. Therefore, using a thick backing plate can lead to a weaker magnetic field strength above the target surface[42].
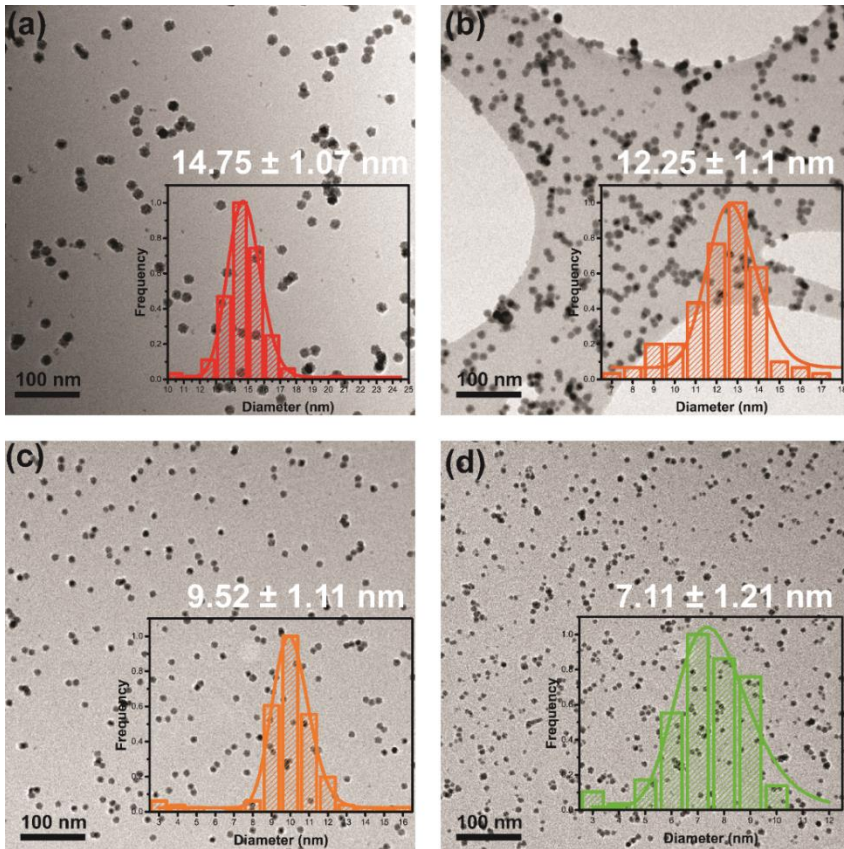
3

3

Figure 3.1 (a-d) Bright-Field TEM images of as-deposited Ge NCs having different sizes as produced by a cluster source based on high pressure magnetron sputtering using different thicknesses (δ) of the backing plates: (a) δ=0 cm, (b) δ=1.5 cm, (c) δ=2 cm, and (d) δ=3 cm. (e) The average diameter of Ge NCs at various thicknesses of the backing plate. Insets: Size histograms of the Ge NCs with curves fitted to the log-normal size distribution model.

To evaluate the variation of magnetic field strength by changing the thickness of backing plates, FEM simulations of the commercial magnetron source were performed. Figure 3.2(b-e) shows the shape and magnitude of the $B_{//}$ ($\sqrt{B_x^2 + B_y^2}$) field on the XY plane of the target surface, when four different

thicknesses (1.5, 3.0, 4.5, 6.0 mm) of the backing plates were used with the z coordinate set to 4.5, 6.0, 7.5, 9.0 mm in multislice, respectively. Similarly, Figure 3.2(f) depicts the profiles of the magnetic field distribution as a function of radial distances along the target surface. Due to the radial symmetry, the profiles in Figure 3.2(f) provide a direct representation of Figures (b-e). Figure 3.2 thus clearly shows that the magnetic flux density is decreasing with increasing axial outward distance. As a result, the electron confinement becomes less tight and a wider race track is expected. Since the supersaturation can be achieved only by sufficient confinement of the vapor, individual atoms or very small clusters will be deposited with reduced magnetic flux density. According to the FEM results, the magnetic field strength can be controlled by the thickness of backing plates, which, in turn, governs the confinement of electrons, and consequently can modulate the size of the Ge NCs. For synthesizing smaller size (<7 nm) Ge NCs, a substantial Cu plate is required. However, then it is difficult to achieve a stable plasma confinement because the magnetic field strength on the Ge target surface becomes too weak. Zhao et al. indicated that the synthesis of smaller Si NCs can be achieved by increasing the amount of inert drift gas (in particular, He), because the drift velocity can then be raised, which causes the residence time of clusters in the aggregation volume to decrease. Nevertheless, in this case, an amorphous structure is anticipated for smaller Si NCs. Notably, a critical ratio of the number density of the Si and Ar atoms (ρ_{Si}/ρ_{Ar}) is needed to heat the Si NCs over the crystallization temperature during the condensation process.[43]
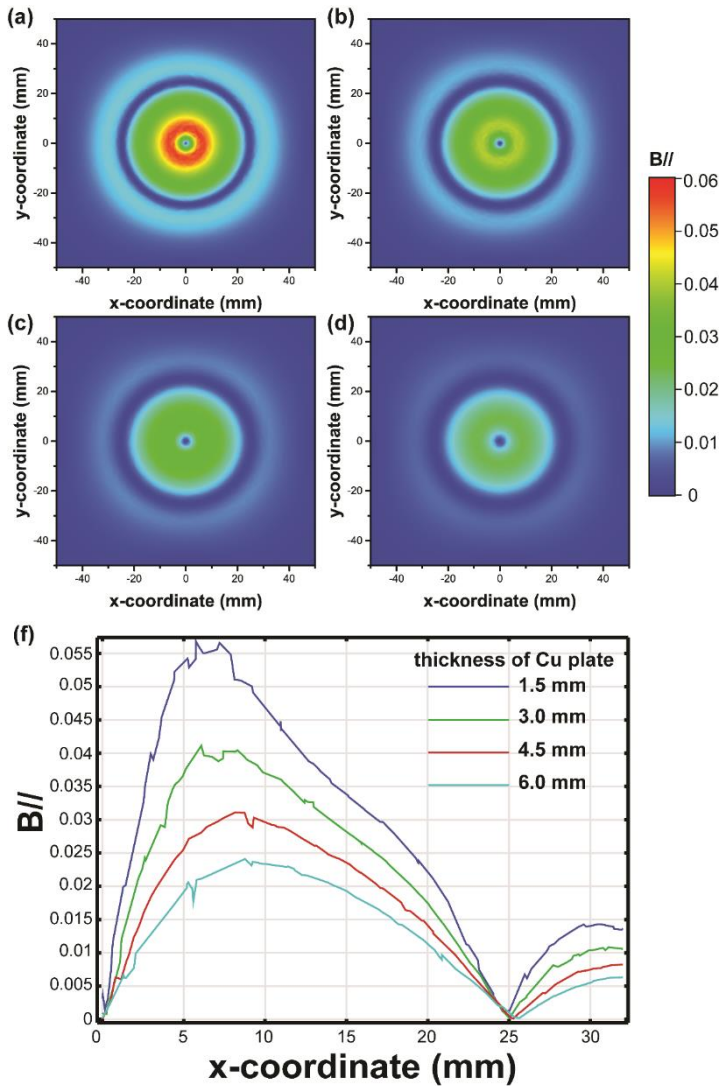
3

Figure 3.2 (a-d) Simulated results of the magnetic field strength ($B_{//}$) for different thickness of Cu plate: (a) 1.5 mm, (b) 3.0 mm, (c) 4.5 mm and (d) 6.0 mm. (e) the $B_{//}$ profile of the magnetic field along the radial direction for the four axial distances.

3.3.2 Structural Characterization of Ge NCs.

As we report in Figure 3.3, the HRTEM characterization was performed in conjunction with the selective area electron diffraction (SAED) to reveal the crystalline details of the Ge NCs. The diffraction pattern in Figure 3.3(b) demonstrates that the crystalline structure of Ge NCs can be indexed with the diamond cubic (*Fd3m*) structure, as the measured interplanar distances of Ge d_{111}, d_{022}, d_{113} are 0.326 nm, 0.198 nm, and 0.169 nm, respectively. Figure 3.3(c) shows exemplary single-crystal Ge NCs oriented along a [212] zone axis The Fast Fourier transform (FFT) in Figure 3.3(d) verifies the diamond cubic crystal structure, containing the (111), (220), and (311) characteristic reflections. Using the line profiles for the (111) and (022) interplanar spacings of Ge NCs, as shown in Figure 3.3(e), the *d*-spacings were calculated to be 1.98 Å for (022) and 3.26 Å for (111). This is in agreement with the spacing distances measured from the SAED pattern. In addition to the majority (~60%) single-crystal Ge NCs (as shown in Figure 3.8), also particles with a polycrystalline structure, oxidation shell, and partially amorphous substructure were identified in HAADF-STEM images of all samples (Figure 3.3(f-h)). This is attributed to the intrinsically high crystallization temperature and oxidation of Ge. Specifically, as Figure 3.3(f) illustrates, as-deposited Ge NCs can also contain a single twin boundary, as indicated by the yellow dashed line. The corresponding FFT pattern demonstrates that the angle between these two domains is around 40°. In fact, such an incomplete crystalline structure of the Ge NCs has been recognized as the major reason that progress in the preparation and further optoelectronic application for group IV NCs has fallen behind those of the groups II-VI and III-V NCs.[24,44,45] Moreover, due to the existence of the oxidation layer, and the partially amorphous structure, the Ge NCs contain many trap states for photogenerated charge carriers that increase the probability of nonradiative recombination.[23,46] As an additional measurement of the material composition, energy-dispersive x-ray spectra were measured and typical Ge peaks were observed (see Appendix, Figure 3.7).
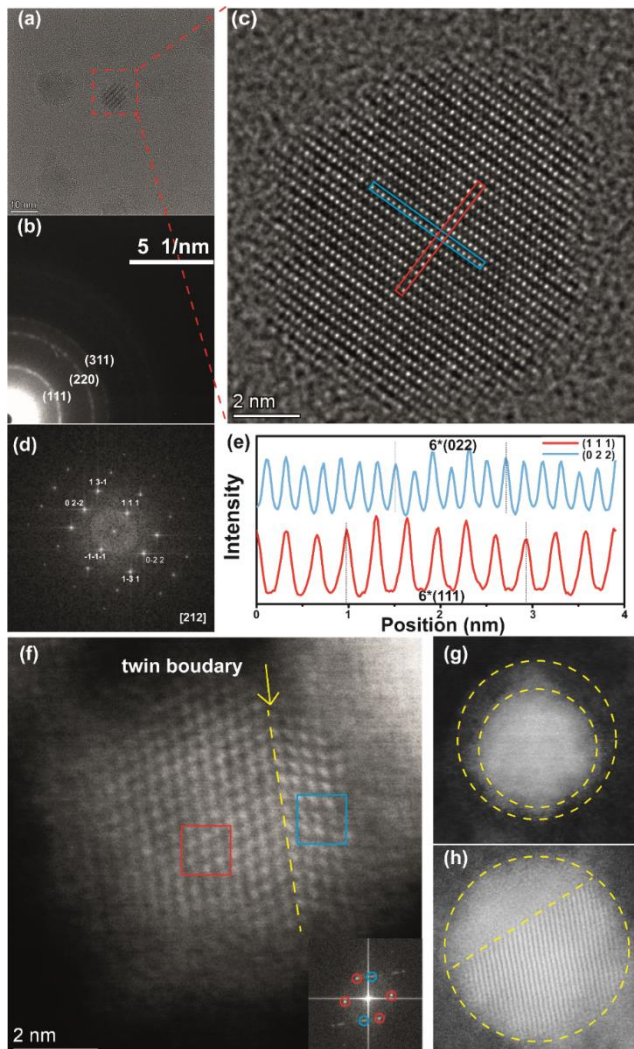
3

Figure 3.3 Representative HRTEM micrographs of Ge NCs: (a) overview of as-deposited Ge NCs, (b) Electron diffraction pattern confirming the diamond cubic crystalline structure of Ge NCs, (c) HRTEM image of Ge NCs taken along a [212] zone axis, (d) line profile along the red and blue line on HRTEM image of figure c, (e) corresponding FFT analysis of the HRTEM image along the [212] zone axis in figure c, (f) twin crystalline structure of Ge NCs, (g) oxidation and (h) partially amorphous Ge NCs.

Further analysis of the stoichiometry and chemical valence for the as-deposited Ge NCs was carried out by X-ray photoelectron spectroscopy (XPS). The survey spectra (Figure 3.4a) demonstrate only the presence of Ge, O, and C in the as-deposited Ge NCs. Figure 3.4b shows the high-resolution XPS spectra of the Ge 3d core- evel region. Due to a non-negligible fraction of Ge NCs bonded with O, a broad emission peak centered at 29.4 eV can be seen. To quantitatively analyze the valence of the as-deposited Ge NCs, the spectra were fitted by multiple Voigt functions. The three main components can be seen at 29.2 eV, 30.5 eV, and 32.0 eV peaks. The emission peak at 29.2 eV is attributed to the Ge-Ge bonds involved in the QD formation. Other higher-energy peaks are related to the presence of GeO (30.5 eV) and GeO_2 (32.0 eV). In addition, the results of the integrated peak area, which are related to each valence state, indicate that the majority components are ~54.0% as Ge, ~31.0% as GeO, and ~15.0% as GeO_2.

3

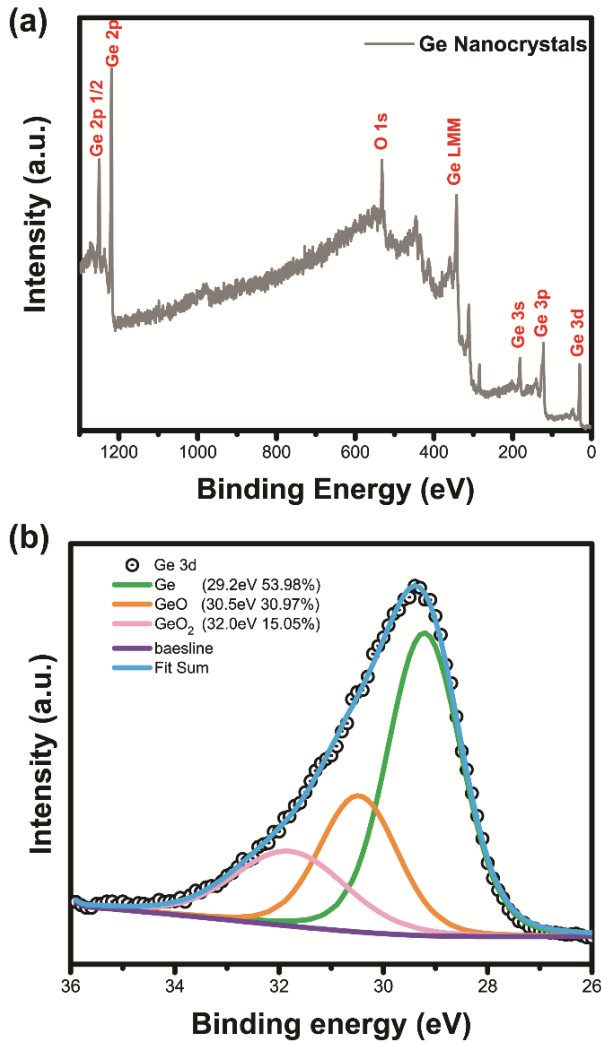**Figure 3.4** XPS spectra of a typical Ge NCs: (a) Survey spectrum, (b) high resolution peak of Ge 3d valence level showing three different fitted Voigt peaks representing Ge, GeO and GeO₂, with Ge being dominant.

3.3.3 Raman Spectroscopy.

The vibrational properties of the as-deposited Ge NCs with different sizes were also characterized by Raman spectroscopy. Since only optical phonons located

at the center of the Brillouin zone are involved in the first-order Raman scattering process for an infinite Ge crystal, there is no momentum exchange during the Raman scattering that leads to a sharp and symmetric vibrational peak at 300 cm^{-1}. However, according to the phonon confinement model,[47,48] the nanoparticles can be considered as a finite crystal and the phonon can be described by a wave packet (instead of plane wave) whose spatial dimensions are commensurate with the crystallite size. As a result, the Raman-active modes will be shifted away from the Brillouin zone center by an effective offset $\Delta q = \sim\pi/D$, where D is the diameter of Ge NCs. Consequently, the Raman peak will be asymmetrically broadened and will shift to lower wavenumbers with decreasing nanoparticle size. Indeed, the first-order Raman spectrum can be described by the phonon confinement model

$$I(\omega) = \int \frac{|C(0,\boldsymbol{q})|^2 d^3\boldsymbol{q}}{[\omega - \omega(\boldsymbol{q})]^2 + (\Gamma_0/2)^2}. \tag{3.1}$$

In Eq. (1) $C(0,\boldsymbol{q})$ is the Fourier coefficient of the weighting function that can be considered nearly constant, $\boldsymbol{q}$ is expressed in units of $2\pi/a_{Ge}$ with a_{Ge} being the lattice constant of Ge (0.568 nm), $\omega(\boldsymbol{q})$ is the phonon dispersion curve, and Γ_0 is the Raman natural line width of bulk Ge.

Figure 3.5(a) shows the typical Raman spectra for the Ge NCs with the four different sizes. According to the phonon confinement model smaller NCs will lead to a shift of the Raman peak to lower wavenumber and also the development of a broader and asymmetric peak (as shown in Figure 3.5(a)). The low-frequency tail of the broad Ge-Ge optical phonon peak can be interpreted as stemming not only from changes in the bond length (due to the increased surface-to-volume ratio of smaller NCs, the fraction of shorter bond lengths from the uncoordinated surface atoms will be increased, which induces Raman scattering at lower frequencies),[14] but also by the existence of the amorphous state or lower crystallinity for smaller NCs, as shown in Figure 3.3(f-h). In order to analyze the relationship between the frequency downshift $\Delta\omega(D)$ of the Raman peak and the diameter D of Ge NCs, the phonon confinement model can be simplified by the bond polarizability model[49] that

leads to the power-law behavior

$$\Delta\omega(D) = -A(a/D)^\gamma \tag{3.2}$$

where a is the lattice parameter of Ge (0.5658 nm). The parameters A and γ are used to describe the vibrational confinement due to the finite size for the Ge NCs. These parameters have the values A = -97.462 cm^{-1} and γ=1.39 for nanometric spheres of diameter D[46]. According to the peak position in Figure 3.5(a), the size of the Ge NCs can be obtained by the phonon confinement model yielding for D the values 15.2 nm, 10.0 nm, 8.95 nm, and 7.28 nm. The differences in the diameter of as-deposited Ge NCs between the calculated results from Eq.(2) and TEM results (cf. Fig.1) are presented in Table 1. Indeed, although for one size a relatively large error occurred, the other values show good consistency between the Raman and TEM measurements for the Ge NCs. The size deviation between the TEM and Raman results can be explained by underestimating the percentage of bigger Ge NCs in the TEM data. This is because, to obtain the size distribution, the instrumental correction of the TEM data tends to underestimate the percentage of bigger Ge NCs in favor of the more numerous smaller NCs.[50] In addition, the peak shift of the optical Ge-Ge phonon demonstrates that the states of Ge NCs preserve their individual character instead of forming bulk Ge films. Finally, as Figure 3.5(b) shows, the calculation of the Raman shifts using Eq. (2) with D the values obtained from the TEM (Table 1) indicates a good agreement with the measured Raman frequency shifts.

Table 3.1 Comparison the size of Ge NCs between the results from TEM and the fitting results of phonon confinement model

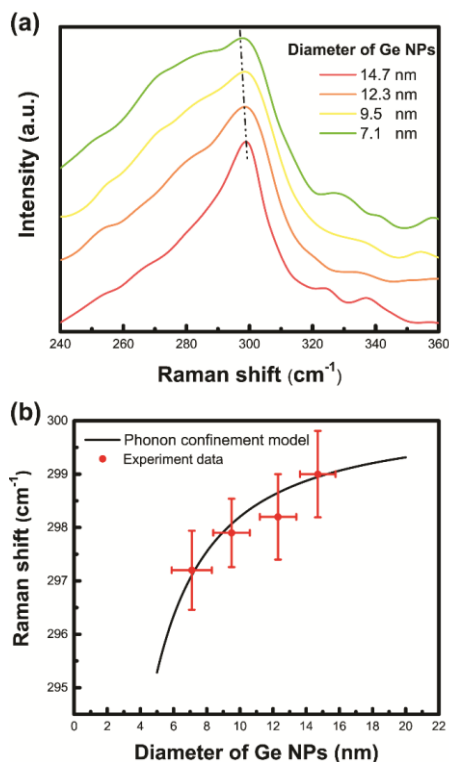|	Crystallite size (nm)			
D_{TEM}	14.75	12.25	9.52	7.11
D_{PCM}	15.20	10.00	8.95	7.28
$\Delta D= /D_{TEM}-D_{PCM}$ /	0.45	2.25	0.57	0.17

Figure 3.5 (a) Raman spectra of the Ge NCs with four different average diameters. (b) Raman shift of the peak position as a function of diameter of Ge NCs.

3.3.4 Quantum Confinement Effects

Furthermore, the optical properties of the Ge NCs were investigated via UV-vis-NIR absorbance measurements. Unlike the direct band gap semiconductors, such as the PbS, the photoluminescence signal for the Ge NCs could not be easily observed limiting the precise determination of the band gap of the NCs. Holman et al. also indicated that the blue-shifted photoluminescence data in many papers originate from the surface ligand on the Ge NCs[22]. Until now, only four reports present convincing photoluminescence data yielding a band gap energy close to that of bulk Ge

with increasing size of the Ge NCs [23–26]. According to the quantum confinement effects, when the size of semiconductor nanocrystals is below the Bohr exciton radius (~24 nm for Ge), the size-dependent effect will manifest itself by band gap broadening of the Ge NCs[21]. As it is shown in Figure 3.6(a), with decreasing size of the Ge NCs the onset of the absorption peak undergoes a blue shift that follows very well the predicted trend of quantum confinement effects. Notably, the quantum confinement theory suggests that because of the geometric restriction of charge carriers at the nanoscale, the momentum conservation could be relaxed for optical transitions [16]. As a result, the probability of band-to-band transition (quasi-direct) can be improved for indirect band gap semiconductor nanocrystals[21]. However, the exciton peak cannot be observed in the absorption spectra for our experiments, suggesting that no conversion occurs from indirect to quasi-direct band gap structure for the Ge NCs (see also Appendix, Figure 3.6(b)).

To analyze more quantitatively the size effects on optical band gaps from absorption spectra, Tauc plots were made[51,52] since this is a common method to interpret the optical band gap for semiconductor materials from the absorption spectrum. The band gap energies can be determined by extrapolating the tangential line from the linear region of the onset of the first major absorption to the intersection point of the abscissa on the energy axis. The approximate indirect band gap energies of the Ge NCs from the Tauc plots (see Figure 3.6(a)) were 0.85 eV for 14.7 nm, 0.95 eV for 12.3 nm, 1.06 eV for 9.5 nm, and 1.12 eV for 7.1 nm, respectively. These band gap energies suggest strong quantum size effects when the size of the Ge NCs is smaller than the Bohr exciton radius, and a clear trend of widening band gap with decreasing the size of Ge NCs. However, the absorption measurements lack the correction of light scattering, which makes it difficult to identify precisely the absorption onset.[14]
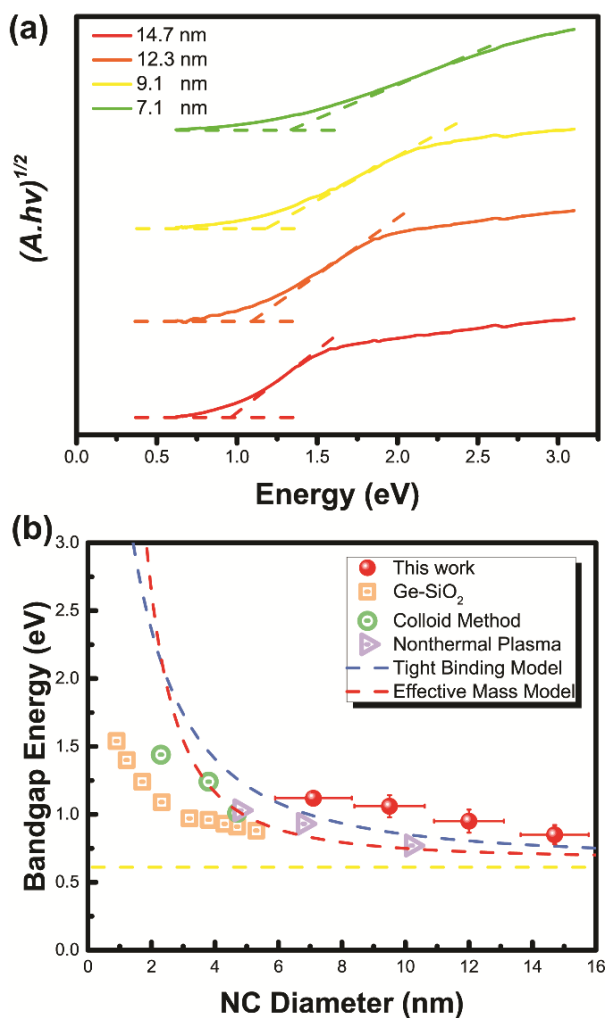
Figure 3.6 (a) Tauc plot from the absorption data used to determine the band gap energy of Ge NCs. (b) Comparison with band gap size versus nanoparticle diameter data from the literature. The band gap energies determined in this work are plotted together with the ones of Ge NPs synthesized with the colloidal method[24], Ge NPs embedded in SiO_2 [53], Ge NPs synthesized with the non-thermal plasma method[23], and predicted band gap values obtained from an effective mass and a tight binding model.

To illustrate the confinement effect of Ge NCs, we summarized the band gap energies as a function of the NCs size along with the data from studies of other groups[23,24,53] as it is shown in Figure 3.6b. In addition, the relationship between the band gap energy and the size of the Ge NCs was also compared to the effective mass model (EMM) [54,55]and a tight-binding (TB) model[56]. In the strong confinement regime, where the size of NCs is smaller than the Bohr radius (~24 nm), the relationship between the band gap energy $E_{g,NC}$ and the particle diameter D based on the EMM is given by

$$E_{g,NC} = E_{g,bulk} + \frac{h^2}{2D^2}\left(\frac{1}{m_e^*} + \frac{1}{m_h^*}\right)$$ (3.3)

where $E_{g,bulk}$ is the bulk band gap energy of Ge (0.67 eV), h is the Planck's constant, and m_e^* and m_h^* are the effective masses of the electrons and holes, respectively. If the effective mass can be calculated using the density of states, then the mass term in Eq. (3) can be correlated with the parabolicity of the band structure. The latter means that the bulk effective mass value of Ge can be used for the nanostructures. Therefore, these definitions yield from Eq. (3) for the band gap of the NCs

$$E_{g,NC} = E_{g,bulk} + \frac{A}{D^2}$$ (3.4)

where the calculated parameter A for Ge is 7.88 eV×nm².[54,57]

The band gap from the *sp³* TB model for spherical dots can be described by the analytic expression[56]

$$E_{g.NC} = E_{g,bulk} + \frac{11863.7}{D^2+2.397D+4.252} + \frac{15143.8}{D^2+6.465D+2.546}$$ (3.5)

Since the EMM is known to overestimate the band gap energy of NCs as small as a few nanometers[53], a more accurate theoretical description can be obtained by the TB model. As it is shown in Figure 3.6b, our experimentally resolved band gap shows a clear dependence on the size of Ge NCs, and a similar trend to that predicted by the TB model. In addition, we observe that all our experimental results are higher than the prediction of the TB model. Such a slight difference can be explained by several deficiencies such as surface oxidation, defects in crystalline Ge clusters, and partly amorphous Ge clusters.

First, the XPS analysis has shown that the as-deposited Ge NCs cannot be expected to be a pure ensemble of Ge NCs. Indeed, the effect of substoichiometric oxides shells on the shift of the band gap energy has been reported in the literature.[58] Second, as it is also mentioned in the HRTEM characterization of the NCs, the deviation of the band gap energy may also result from the existence of uncertain fraction of incomplete crystallites or defects within the Ge NCs. Third, because of the band gap energy determination by extrapolation from the optical absorption tail, the uncertainty in the interpretation of the optical spectrum could also be the source of the error.[59] In any case, the good agreement with the TB model suggests that the as-deposited Ge NCs persist to exhibit the indirect band gap nature also in the quantum confinement regime.

3.4 Conclusions

In summary, a novel gas-phase synthesis procedure for Ge NCs has been established via the gas aggregation cluster source that allows a relatively simple way to tune the size and subsequently the optical absorption of Ge NCs. The size selection can readily be controlled by the adjustment of the equivalent thickness of the target (using various thicknesses for the backing plate) that allows manipulation of the magnetic field configuration on the target surface as it has been explained in terms of the FEM simulations. Therefore, one can avoid the use of mass selection to form size-selected NCs and thus avoid sacrificing the production yield of NCs. HRTEM and Raman spectroscopy demonstrated in close agreement that the size of Ge NCs decreases with increasing the equivalent thickness of the Ge target. HRTEM and SAED measurements demonstrated that most Ge NCs have single crystalline diamond structure. HRTEM also revealed the presence of an oxide shell, as well as more details of the crystalline structure as, for example, the existence of a minor fraction of NCs with a polycrystalline structure. In addition, the XPS study verified the valence state of the Ge NCs, and quantified the number of the

oxidation states of the NCs indicating substoichiometric Ge oxide shells. Furthermore, the data from the UV-vis absorbance measurements demonstrated via the Tauc plots the quantum confinement effect on the band gap of Ge NCs showing a band gap energy that can be tuned by the size of Ge NCs. Finally, we stress that our results follow the TB model prediction for the band gap size rather well. Although high-quality Ge NCs without oxidation and with a homogeneous crystalline phase are still challenging to produce, the cluster deposition method shown here can readily produce tunable-size solid-state Ge NCs, which is promising for further solid-state optoelectronic device investigations. Currently, research is in progress to suppress the oxidation and improve the crystalline quality during deposition, as well as to combine the synthesis with other group IV nanoparticles (e.g., GeSi and GeSn). In addition, our method might also be suitable for other highly covalent systems (e.g., InN or InSb) which could be difficult to synthesize by the solution-phase method.[18]

Reference

(1)   Efros, A. L.; Lockwood, D. J.; Tsybeskov, L. *Semiconductor Nanocrystals: From Basic Principles to Applications*; Springer: New York, 2013.

(2)   Nozik, A. J.; Beard, M. C.; Luther, J. M.; Law, M.; Ellingson, R. J.; Johnson, J. C. Semiconductor Quantum Dots and Quantum Dot Arrays and Applications of Multiple Exciton Generation to Third-Generation Photovoltaic Solar Cells. *Chem. Rev.* **2010**, *110* (11), 6873–6890.

(3)   Keuleyan, S.; Lhuillier, E.; Brajuskovic, V.; Guyot-Sionnest, P. Mid-Infrared HgTe Colloidal Quantum Dot Photodetectors. *Nat. Photonics* **2011**, *5* (8), 489–493.

(4)   Shirasaki, Y.; Supran, G. J.; Bawendi, M. G.; Bulović, V. Emergence of Colloidal Quantum-Dot Light-Emitting Technologies. *Nat. Photonics* **2013**, *7* (1), 13–23. https://doi.org/10.1038/nphoton.2012.328.

(5)   Carolan, D.; Doyle, H. Size and Emission Color Tuning in the Solution Phase Synthesis of Highly Luminescent Germanium Nanocrystals. *J. Mater. Chem. C* **2014**, *2* (18), 3562–3568.

(6)   Vaughn, D. D.; Schaak, R. E. Synthesis, Properties and Applications of Colloidal Germanium and Germanium-Based Nanomaterials. *Chemical Society Reviews*. 2013, pp 2861–2879.

(7)   Philipp, H. R.; Taft, E. A. Optical Constants of Germanium in the Region 1 to 10 Ev. *Phys. Rev.* **1959**, *113* (4), 1002–1005.

(8)   Saeed, S.; de Weerd, C.; Stallinga, P.; Spoor, F. C.; Houtepen, A. J.; DA Siebbeles, L.; Gregorkiewicz, T. Carrier Multiplication in Germanium Nanocrystals. *Light Sci. Appl.* **2015**, *4* (2), e251–e251.

(9)   Taylor, B. R.; Kauzlarich, S. M.; Lee, H. W. H.; Delgado, G. R. Solution Synthesis of Germanium Nanocrystals Demonstrating Quantum Confinement. *Chem. Mater.* **1998**, *10* (1), 22–24.

(10)   Henderson, E. J.; Seino, M.; Puzzo, D. P.; Ozin, G. A. Colloidally Stable Germanium Nanocrystals for Photonic Applications. *ACS Nano* **2010**, *4* (12), 7683–7691.

(11)   Henderson, E. J.; Hessel, C. M.; Veinot, J. G. C. Synthesis and Photoluminescent Properties of Size-Controlled Germanium Nanocrystals from Phenyl Trichlorogermane-Derived Polymers. *J. Am. Chem. Soc.* **2008**, *130* (11), 3624–3632.

(12)   Muthuswamy, E.; Zhao, J.; Tabatabaei, K.; Amador, M. M.; Holmes, M. A.; Osterloh, F. E.; Kauzlarich, S. M. Thiol-Capped Germanium Nanocrystals: Preparation and Evidence for Quantum Size Effects. *Chem. Mater.* **2014**, *26* (6), 2138–2146.

(13)   Muthuswamy, E.; Iskandar, A. S.; Amador, M. M.; Kauzlarich, S. M. Facile Synthesis of Germanium Nanoparticles with Size Control: Microwave versus Conventional Heating. *Chem. Mater.* **2013**, *25* (8), 1416–1422.

(14)   Tabatabaei, K.; Holmes, A. L.; Newton, K. A.; Muthuswamy, E.; Sfadia,

3

R.; Carter, S. A.; Kauzlarich, S. M. Halogen-Induced Crystallinity and Size Tuning of Microwave Synthesized Germanium Nanocrystals. *Chem. Mater.* **2019**, *31* (18), 7510–7521.

(15) Lu, X.; Korgel, B. A.; Johnston, K. P. High Yield of Germanium Nanocrystals Synthesized from Germanium Diiodide in Solution. *Chem. Mater.* **2005**, *17* (25), 6479–6485.

(16) Zaitseva, N.; Dai, Z. R.; Grant, C. D.; Harper, J.; Saw, C. Germanium Nanocrystals Synthesized in High-Boiling-Point Organic Solvents. *Chem. Mater.* **2007**, *19* (21), 5174–5178.

(17) Gerung, H.; Bunge, S. D.; Boyle, T. J.; Brinker, C. J.; Han, S. M. Anhydrous Solution Synthesis of Germanium Nanocrystals from the Germanium(II) Precursor Ge[N(SiMe3)2]2. *Chem. Commun.* **2005**, No. 14, 1914–1916.

(18) Lu, H.; Carroll, G. M.; Neale, N. R.; Beard, M. C. Infrared Quantum Dots: Progress, Challenges, and Opportunities. *ACS Nano*. 2019, pp 939–953.

(19) Rodio, M.; Scarpellini, A.; Diaspro, A.; Intartaglia, R. Tailoring of Size, Emission and Surface Chemistry of Germanium Nanoparticles *via* Liquid-Phase Picosecond Laser Ablation. *J. Mater. Chem. C* **2017**, *5* (46), 12264–12271. https://doi.org/10.1039/C7TC01992K.

(20) Fan, J.; Chu, P. K. Group IV Nanoparticles: Synthesis, Properties, and Biological Applications. *Small* **2010**, *6* (19), 2080–2098.

(21) Carolan, D. Recent Advances in Germanium Nanocrystals: Synthesis, Optical Properties and Applications. *Progress in Materials Science*. Pergamon October 1, 2017, pp 128–158.

(22) Holman, Z. C.; Kortshagen, U. R. Absolute Absorption Cross Sections of Ligand-Free Colloidal Germanium Nanocrystals. *Appl. Phys. Lett.* **2012**, *100* (13), 133108.

(23) Wheeler, L. M.; Levij, L. M.; Kortshagen, U. R. Tunable Band Gap Emission and Surface Passivation of Germanium Nanocrystals Synthesized in the Gas Phase. *J. Phys. Chem. Lett.* **2013**, *4* (20), 3392–3396.

(24) Ruddy, D. A.; Johnson, J. C.; Smith, E. R.; Neale, N. R. Size and Bandgap Control in the Solution-Phase Synthesis of near-Infrared-Emitting Germanium Nanocrystals. *ACS Nano* **2010**, *4* (12), 7459–7466.

(25) Heath, J. R.; Shiang, J. J.; Alivisatos, A. P. Germanium Quantum Dots: Optical Properties and Synthesis. *J. Chem. Phys.* **1994**, *101* (2), 1607–1615.

(26) Lee, D. C.; Pietryga, J. M.; Robel, I.; Werder, D. J.; Schaller, R. D.; Klimov, V. I. Colloidal Synthesis of Infrared-Emitting Germanium Nanocrystals. *J. Am. Chem. Soc.* **2009**, *131* (10), 3436–3437.

(27) Kruis, F. E.; Fissan, H.; Peled, A. Synthesis of Nanoparticles in the Gas Phase for Electronic, Optical and Magnetic Applications—a Review. *J. Aerosol Sci.* **1998**, *29* (5–6), 511–535.

(28) Sattler, K.; Mühlbach, J.; Recknagel, E. Generation of Metal Clusters

3

Containing from 2 to 500 Atoms. *Phys. Rev. Lett.* **1980**, *45* (10), 821–824.

(29)   Pratontep, S.; Carroll, S. J.; Xirouchaki, C.; Streun, M.; Palmer, R. E. Size-Selected Cluster Beam Source Based on Radio Frequency Magnetron Plasma Sputtering and Gas Condensation. *Rev. Sci. Instrum.* **2005**, *76* (4), 045103.

(30)   Haberland, H.; Mall, M.; Moseler, M.; Qiang, Y.; Reiners, T.; Thurner, Y. Filling of Micron-sized Contact Holes with Copper by Energetic Cluster Impact. *J. Vac. Sci. Technol. A Vacuum, Surfaces, Film.* **2002**, *12* (5), 2925–2930.

(31)   Kortshagen, U. R.; Sankaran, R. M.; Pereira, R. N.; Girshick, S. L.; Wu, J. J.; Aydil, E. S. Nonthermal Plasma Synthesis of Nanocrystals: Fundamental Principles, Materials, and Applications. *Chem. Rev.* **2016**, *116* (18), 11061–11127.

(32)   Ahadi, A. M.; Hunter, K. I.; Kramer, N. J.; Strunskus, T.; Kersten, H.; Faupel, F.; Kortshagen, U. R. Controlled Synthesis of Germanium Nanoparticles by Nonthermal Plasmas. *Appl. Phys. Lett.* **2016**, *108* (9), 093105.

(33)   Ehbrecht, M.; Huisken, F. Gas-Phase Characterization of Silicon Nanoclusters Produced by Laser Pyrolysis of Silane. *Phys. Rev. B* **1999**, *59* (4), 2975–2985.

(34)   Rao, N.; Girshick, S.; Heberlein, J.; McMurry, P.; Jones, S.; Hansen, D.; Micheel, B. Nanoparticle Formation Using a Plasma Expansion Process. *Plasma Chem. Plasma Process.* **1995**, *15* (4), 581–606.

(35)   Wheeler, L. M.; Nichols, A. W.; Chernomordik, B. D.; Anderson, N. C.; Beard, M. C.; Neale, N. R. All-Inorganic Germanium Nanocrystal Films by Cationic Ligand Exchange. *Nano Lett.* **2016**, *16* (3), 1949–1954.

(36)   Jurbergs, D.; Rogojina, E.; Mangolini, L.; Kortshagen, U. Silicon Nanocrystals with Ensemble Quantum Yields Exceeding 60%. *Appl. Phys. Lett.* **2006**, *88* (23), 233116.

(37)   Palmer, R. E.; Cai, R.; Vernieres, J. Synthesis without Solvents: The Cluster (Nanoparticle) Beam Route to Catalysts and Sensors. *Acc. Chem. Res.* **2018**, *51* (9), 2296–2304.

(38)   Tang, W.; Eilers, J. J.; Van Huis, M. A.; Wang, D.; Schropp, R. E. I.; Di Vece, M. Formation and Photoluminescence of "Cauliflower" Silicon Nanoparticles. *J. Phys. Chem. C* **2015**, *119* (20), 11042–11047.

(39)   Cardoso, J.; Marom, S.; Mayer, J.; Modi, R.; Podestà, A.; Xie, X.; van Huis, M. A.; Di Vece, M. Germanium Quantum Dot Grätzel-Type Solar Cell. *Phys. Status Solidi Appl. Mater. Sci.* **2018**, *215* (24), 1800570.

(40)   Marek, A.; Valter, J.; Kadlec, S.; Vyskočil, J. Gas Aggregation Nanocluster Source — Reactive Sputter Deposition of Copper and Titanium Nanoclusters. *Surf. Coatings Technol.* **2011**, *205* (SUPPL. 2), S573–S576.

(41)   Vernieres, J.; Steinhauer, S.; Zhao, J.; Chapelle, A.; Menini, P.; Dufour, N.; Diaz, R. E.; Nordlund, K.; Djurabekova, F.; Grammatikopoulos, P.;

3

et al. Gas Phase Synthesis of Multifunctional Fe-Based Nanocubes. *Adv. Funct. Mater.* **2017**, *27* (11), 1605328.

(42)   Xing, L.; ten Brink, G. H.; Kooi, B. J.; Palasantzas, G. Preparation of Tunable-Sized Iron Nanoparticles Based on Magnetic Manipulation in Inert Gas Condensation (IGC). *J. Appl. Phys.* **2017**, *121* (2), 024305.

(43)   Zhao, J.; Singh, V.; Grammatikopoulos, P.; Cassidy, C.; Aranishi, K.; Sowwan, M.; Nordlund, K.; Djurabekova, F. Crystallization of Silicon Nanoclusters with Inert Gas Temperature Control. *Phys. Rev. B* **2015**, *91* (3), 035419.

(44)   Wang, W.; Huang, J.; Ren, Z. Synthesis of Germanium Nanocubes by a Low-Temperature Inverse Micelle Solvothermal Technique. *Langmuir* **2005**, *21* (2), 751–754.

(45)   Kortshagen, U. Nonthermal Plasma Synthesis of Semiconductor Nanocrystals. *J. Phys. D. Appl. Phys.* **2009**, *42* (11), 113001.

(46)   Ghosh, B.; Hamaoka, T.; Nemoto, Y.; Takeguchi, M.; Shirahata, N. Impact of Anchoring Monolayers on the Enhancement of Radiative Recombination in Light-Emitting Diodes Based on Silicon Nanocrystals. *J. Phys. Chem. C* **2018**, *122* (11), 6422–6430.

(47)   Nemanich, R. J.; Solin, S. A.; Martin, R. M. Light Scattering Study of Boron Nitride Microcrystals. *Phys. Rev. B* **1981**, *23* (12), 6348–6356.

(48)   Campbell, I. H.; Fauchet, P. M. The Effects of Microcrystal Size and Shape on the One Phonon Raman Spectra of Crystalline Semiconductors. *Solid State Commun.* **1986**, *58* (10), 739–741.

(49)   Zi, J.; Büscher, H.; Falter, C.; Ludwig, W.; Zhang, K.; Xie, X. Raman Shifts in Si Nanocrystals. *Appl. Phys. Lett.* **1996**, *69* (2), 200–202.

(50)   Bottani, C. E.; Mantini, C.; Milani, P.; Manfredini, M.; Stella, A.; Tognini, P.; Cheyssac, P.; Kofman, R. Raman, Optical-Absorption, and Transmission Electron Microscopy Study of Size Effects in Germanium Quantum Dots. *Appl. Phys. Lett.* **1996**, *69* (16), 2409–2411.

(51)   Tauc, J.; Grigorovici, R.; Vancu, A. Optical Properties and Electronic Structure of Amorphous Germanium. *Phys. status solidi* **1966**, *15* (2), 627–637.

(52)   Tauc, J. Optical Properties and Electronic Structure of Amorphous Ge and Si. *Mater. Res. Bull.* **1968**, *3* (1), 37–46.

(53)   Takeoka, S.; Fujii, M.; Hayashi, S.; Yamamoto, K. Size-Dependent near-Infrared Photoluminescence from Ge Nanocrystals Embedded in SiO2 Matrices. *Phys. Rev. B* **1998**, *58* (12), 7921–7925.

(54)   Barbagiovanni, E. G.; Lockwood, D. J.; Simpson, P. J.; Goncharova, L. V. Quantum Confinement in Si and Ge Nanostructures. *J. Appl. Phys.* **2012**, *111* (3), 034307.

(55)   Trwoga, P. F.; Kenyon, A. J.; Pitt, C. W. Modeling the Contribution of Quantum Confinement to Luminescence from Silicon Nanoclusters. *J. Appl. Phys.* **1998**, *83* (7), 3789–3794.

(56)   Niquet, Y. M.; Allan, G.; Delerue, C.; Lannoo, M. Quantum Confinement in Germanium Nanocrystals. *Appl. Phys. Lett.* **2000**, *77* (8), 1182–1184.

(57)   Cosentino, S.; Barbagiovanni, E. G.; Crupi, I.; Miritello, M.; Nicotra, G.; Spinella, C.; Pacifici, D.; Mirabella, S.; Terrasi, A. Size Dependent Light Absorption Modulation and Enhanced Carrier Transport in Germanium Quantum Dots Devices. *Sol. Energy Mater. Sol. Cells* **2015**, *135*, 22–28.

(58)   Kobayashi, M.; Thareja, G.; Ishibashi, M.; Sun, Y.; Griffin, P.; McVittie, J.; Pianetta, P.; Saraswat, K.; Nishi, Y. Radical Oxidation of Germanium for Interface Gate Dielectric GeO 2 Formation in Metal-Insulator-Semiconductor Gate Stack. *J. Appl. Phys.* **2009**, *106* (10), 104117.

(59)   Millo, O.; Balberg, I.; Azulay, D.; Purkait, T. K.; Swarnakar, A. K.; Rivard, E.; Veinot, J. G. C. Direct Evaluation of the Quantum Confinement Effect in Single Isolated Ge Nanocrystals. *J. Phys. Chem. Lett.* **2015**, *6* (17), 3396–3402.
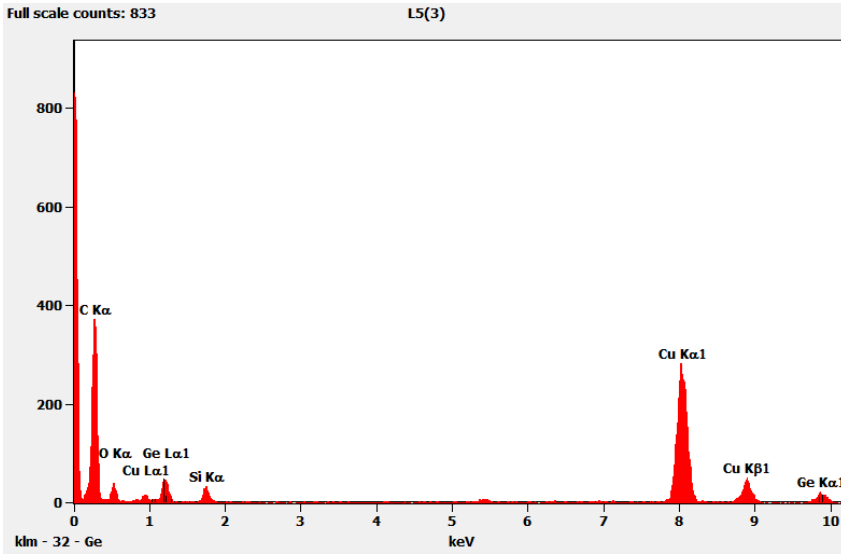
3

Appendix

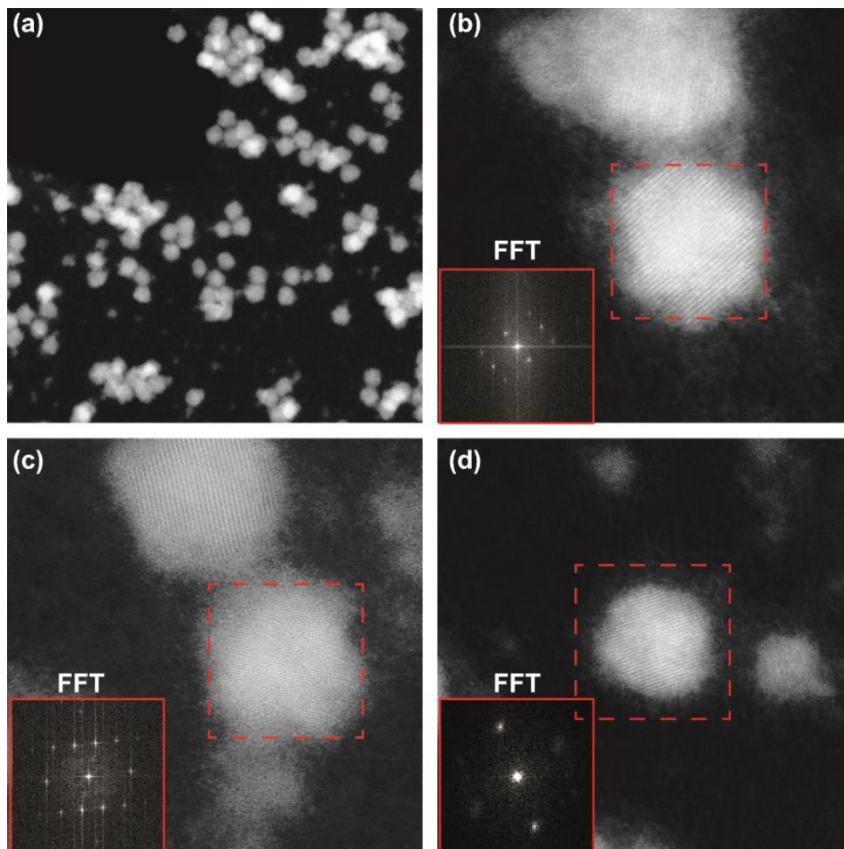**Figure 3.7** Energy dispersive X-ray (EDX) spectrum of as-deposited Ge NCs

Figure 3.8 Representative HR-STEM images of Ge NCs: (a) overview of as-deposited Ge NCs showing the narrow size distribution. (b-d) HR-STEM images of individual as-deposited Ge NCs. The insets are FFT images of the selected Ge NCs illustrating their single crystalline structure.
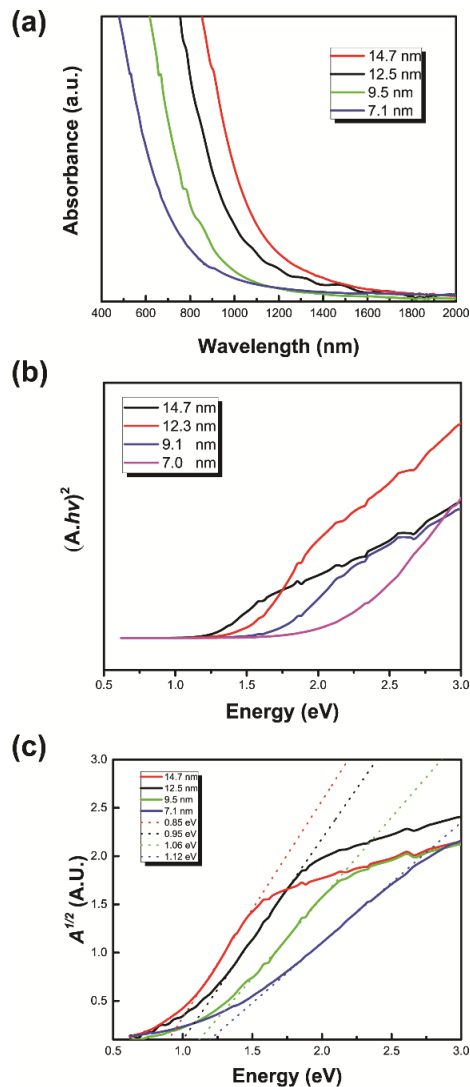
3

Figure 3.9 (a) Absorption spectrum of the as-deposited Ge NCs with different average sizes. (b) Tauc plot of the absorption spectrum with the direct bandgap function $(Ah\nu)^2$. A satisfactory linear fitting could not be identified from the plot indicating that there is no direct bandgap structure for the Ge NCs. (c) Tauc plot of the absorption spectrum with the indirect bandgap function $(Ah\nu)^{1/2}$

It has been suggested that the relationship between the absorption coefficient (α) and the incident photon energy near the optical band edge can be expressed by the Urbach empirical rule, which demonstrates the existence of localized states in the optical energy bandgap. For the absorption spectrum the Urbach equation can be written as[12]

$$\text{abs}(\lambda) = D_3 \exp\left(\frac{hc}{E_{tail}}\lambda\right) \tag{3.6}$$

where D_3 is (αd/2.303, d is the thickness of the sample). The E_{tail} can be obtained by the linear fitting of the Ln(abs) vs 1/λ data, since it can be identified by E_{tail}=1239.83 slope. As it is shown in Figure 3.10, there is no linear region in the curves, which suggests that localized states are not present in the Ge NCs samples.
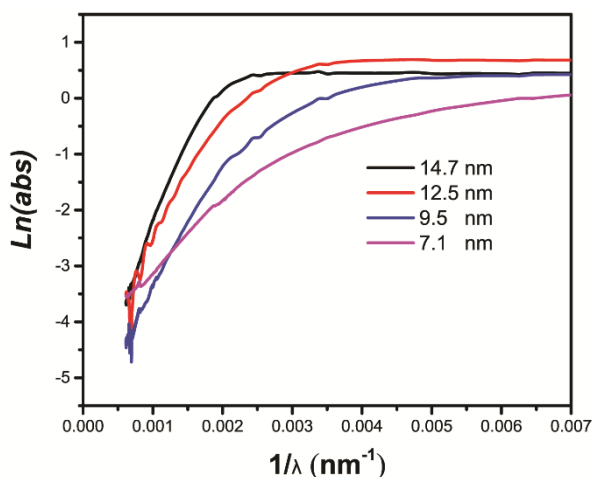

Figure 3.10 Dependence of Ln(abs) vs. 1/ λ for all samples with Ge NCs.

3

4

**Tailoring Growth Kinetics towards Size-Dependent Work Function of
Ge Nanocrystals Synthsized by Inert Gas Condensation**

4

Abstract

Understanding the size-dependent electronic properties of germanium nanocrystals (Ge NCs) is of fundamental importance for improving the efficiency of optoelectronic devices based on such NCs. Here, Ge NCs with tunable size were synthesized by magnetron-sputtering cluster beam deposition, where the size of the as-deposited Ge NCs can be finely controlled between 6 and 36 nm by helium gas flow rates and variable magnetic field configurations above the target surface. Because the size of the as-deposited Ge NCs highly depends on the nucleation process inside the plasma region, a detailed comparison between these two process parameters on the size control was formulated from the perspective of the growth kinetic mechanism. Furthermore, the local surface potential of different-sized Ge NCs deposited on n-type silicon substrates was measured by Kelvin probe force microscopy. The surface potential fluctuation of n-type Si covered by Ge NCs shows a strongly size-dependent relationship with the size of the Ge NCs, where the surface potential fluctuation increases when their size reduces. Because the surface potential fluctuation between the intrinsic Ge NCs and the n-type silicon substrate tends to get smaller as the NCs' size decreases due to the quantum confinement effect, the number of charges transferred between the electronic bands will reduce as the size of Ge NCs decreases. The latter exactly explains the observed experimental results. Therefore, this work offers a perspective to understand the behavior of charge transfer, which plays an important role in the performance of optoelectronic devices.

4.1 Introduction

Semiconductor nanocrystals (NCs) have been the subject of relentless research due to their size-dependent physical properties, which make them potential candidates for electronic and optoelectronic applications.[1,2] Based on the quantum confinement theory, when the radius of NCs is scaled down below their Bohr exciton radius, the band gap energy of semiconductor NCs can be

tuned by varying their size.[3] Although the binary NC systems that are made up of group III-V or II-VI elements have been well developed, group IV semiconductor NCs also remain of strong interest that continue to inspire intense research. One main interest that arises for the group IV NCs, especially for Si NCs, stems from the fact that they are compatible with the existing microelectronic industry and as a result reduce the cost of technological integration. Moreover, because group IV NCs exclude the use of toxic heavy-metal elements, for example, Cd and Pd, they are deemed suitable for further biological applications.[4,5] Among the group IV NCs, germanium (Ge) NCs are highly promising due to their relatively larger Bohr exciton radius[6] (~24 nm) and absorption coefficient[7] (~2×10^5 cm^{-1} at 2 eV), which makes them attractive especially for optoelectronic applications, such as light-emitting devices[8] and solar cells[9].

Furthermore, in many microelectronic applications, the exchange of charge at the interface of the device is one of the essential processes for further development.[10,11] In the case of a quantum dot (QD) sensitized solar cell, the process of carrier dissociation and charge transport at the interface between the QD and the carrier transportation layer is crucial for the overall efficiency of the device.[12,13] Hence, improving the efficiency of such devices strongly depends on the level of understanding of the relationship between the nanostructure and its electronic properties. Therefore, the work function of nano-objects is an important parameter for devices, because it is relevant for the barrier height that affects the carrier mobility.[14] However, when the bulk materials are reduced to nanometer-sized objects such as the NCs, the investigation of the local electronic properties of these nano-objects becomes increasingly challenging.[15] In addition, due to the inevitable imperfections during the fabrication of NCs, the electronic properties of NCs are also affected by defects and impurities.[16]

Although the surface potential or work function can be characterized by conventional spectroscopic techniques such as photoelectron spectroscopy

(PES),[17] due to the limitations in the spatial resolution of spectroscopic methods, the properties of the individual nanostructure cannot be resolved. Nevertheless, in recent years, scanning probe techniques, such as Kelvin probe force microscopy (KPFM) and/or electrostatic force microscopy (EFM), have been widely used to characterize the electronic properties of semiconductor NCs[13,18] and biological materials[19]. Even though scanning tunneling microscopy is a prevalent method for studying the electronic properties of NCs,[20–22] it is restricted to conductive materials (i.e., metal or highly conductive semiconductor). Moreover, the presence of tip-induced band bending can result in the inaccurate interpretation of results. On the other hand, KPFM measurements can overcome these limitations. Because the latter is an atomic force microscopy (AFM)-based technique, it is appropriate to investigate the electrical properties of various systems such as metallic nanoparticles,[23,24] semiconductor NCs,[25,26], and organic materials[27] from the meso- to nanoscopic levels.[10,17] Currently, several studies have demonstrated that KPFM can be applied to characterize the electrostatic properties of semiconductor NCs,[28] involving the size-dependent work function of InAs NCs grown on GaAs[14] and the charge states of Si NCs[29]. However, most of the studies investigated mainly homogeneous thin films of colloidal NCs, from which it is hard to access information on individual NCs, and they also cannot exclude the side effects of ligands.[13,16]

Therefore, so far, only limited research has been focused on the investigation of electrostatic properties of Ge QDs grown by molecular beam epitaxy, which shows only one-dimensional confinement below the Bohr exciton radius of Ge.[30,31] Hence, gas-phase Ge NCs represent a desirable three-dimensional (3D) model that enables the study of the properties of free-standing Ge NCs forming 3D confined QDs. In this regard, the routes for synthesizing Ge NCs can be divided into solution-phase methods, such as the sol-gel process,[32,33] microwave-assisted reduction[34,35], thermal decomposition[36,37], and gas-phase methods including nonthermal plasma,[38] and cluster beam deposition[39,40]. The

several advantages of the gas-phase method compared to the solution-phase method for synthesizing Ge NCs include environmentally friendly routes, easy size control, and ligand-free NCs. The elimination of the side-effects of surface ligands enables the investigation of the electrostatic properties of individual Ge NCs.

Therefore, in this work, the gas-phase Ge NCs were synthesized by a high-pressure magnetron sputtering cluster source, and they were used as a model candidate to investigate the size-dependent electrical properties of free-standing NCs by KPFM. Initially, the size of as-deposited Ge NCs can be tuned by changing the helium gas flow rate and placing backing plates behind the target during the deposition.[39] The effect of these two parameters on the size and crystallinity of the NCs was analyzed and discussed from the growth kinetic mechanism point of view. Subsequently, the work function of Ge NCs deposited with different sizes on n-type Si substrates was studied by KPFM demonstrating a shift of the Fermi level as a function of the size of the NCs. The results obtained by KPFM can be well interpreted as a function of the size of the Ge NCs by the quantum confinement theory.

4.2 Methods

Nanocrystal synthesis. The different size Ge NCs were directly deposited on Si substrates by a home-modified nanoparticle system Nanogen 50 obtained from Mantis Deposited Ltd. (www.mantisdeposited.com).[39] The Ge NCs were directly synthesized by high-pressure magnetron sputtering from a Ge target (50.8 mm diameter, 3 mm thickness, and purity of 99.99%) under Ar gas flow (99.9999%) and a 0.20 A discharge current. The main chamber, where the substrate was placed, was initially evacuated to a base pressure of $\sim 1 \times 10^{-8}$ mbar. The deposition yield can be monitored by a quartz crystal microbalance (QCM) placed next to the substrate holder. The average size of Ge NCs could be tuned from 36 to 20 nm by controlling the ratio of added helium (He) gas flow with respect to main sputtering gas (Ar), and without putting any backing

4

plates. However, for smaller Ge NCs (< 16 nm) various copper backing plates, with their thickness varying between 1.5 and 6 mm, were placed in between the Ge target and the magnetron head, as well as the Ar flow rate was maintained at 20 sccm, to achieve the desired size tuning of the as-deposited NCs. The latter is achieved because one can adjust the magnetic field strength on the target surface where the sputtering takes place.[39]

Transmission Electron Microscopy. The morphology and crystalline structure of the Ge NCs deposited on carbon films were directly characterized after deposition using a transmission electron microscope (JEOL 2010) operated at 200 kV. High-resolution transmission electron microscopy (HR-TEM) images were also recorded using the Thermo Fisher Scientific Themis Z S/TEM with a probe and an image corrector operating at 300 kV.

Atomic and Kelvin Probe Force Microscopy. The morphology and electrical properties of as-deposited Ge NCs were characterized using a Multimode 8 AFM system (Bruker, Santa Barbara, CA) under ambient conditions. The morphology of as-deposited Ge NCs was imaged in tapping mode using a sharp silicon tip (cantilever resonance frequency ~ 325 kHz and spring constant 40 N/m). For the KPFM measurements, the samples were imaged in a lift mode, also known as amplitude-modulation KPFM (AM-KPFM), using a Pt coated silicon tip (cantilever resonance frequency ~ 75 kHz and spring constant 2.8 N/m). The typical radius of a coated tip is below 20 nm, and it has a similar size as the Ge NCs under investigation. In this case, because the local electrostatic interaction from the cantilever surface can be minimized in the lift mode, reasonable accurate results could be expected.[41,42] In the lift mode, during the first pass, the sample is scanned to obtain the topographical information. Subsequently, during the second pass, the cantilever is raised to a user-defined height, following the stored topography data, where the surface potential is measured. In order to minimize the error of the tip convolution that originates from the side-capacitance effect[43] and maintain a sufficient signal-to-noise ratio when the lift height is too high, as

well as, at the same time, to avoid topography contributions due to van der Waals interactions at shorter ranges, several experiments at different lift heights were conducted. The result of the relationship between the measured ΔCPD and the lift height is shown in the appendix (Figure 4.7), which indicates that 25 nm is an effective lift height for the KPFM measurements.

During the KPFM measurement, both a DC voltage V_{dc} and an AC voltage $V_{ac}\sin(\omega t)$ were applied to the tip as shown in Figure 4.8.[17] The V_{dc} is adjusted to compensate for the electrostatic forces (by nullifying the first harmonic), and this is recorded as the contact potential difference (CPD) between the AFM tip and the sample. The latter is defined as

$$V_{CPD} = \frac{\Phi_{sample} - \Phi_{tip}}{e} \tag{4.1}$$

Furthermore, the surface potential fluctuation of n-type Si covered by Ge NCs is termed as ΔCPD for the Ge NCs. Also, the ΔCPD of the Ge NCs with respect to the substrate can be defined as

$$\Delta V_{CPD\left(\frac{NC}{Sub}\right)} = \frac{\Phi_{sub} - \Phi_{tip}}{e} - \frac{\Phi_{NC} - \Phi_{tip}}{e} = \frac{(\Phi_{sub} - \Phi_{NC})}{e} \tag{4.2}$$

where the Φ_{sub} and Φ_{NC} are the work functions of the substrate and as-deposited Ge NCs, respectively. In practice, the tip-sample can be considered as a capacitor, and the electrostatic force of the tip-sample is expressed as:

$$F_{es} = -\frac{1}{2}\frac{dC}{dz}[(V_{dc} - V_{CPD}) + V_{ac}\sin(\omega_{AC}t)]^2 \tag{4.3}$$

where the dC/dz is the gradient of the capacitance between the tip and the sample surface. F_{es} can be divided into three components, wherein the first harmonic component of F_{es}, F_{ω}, depends on the V_{CPD} as:

$$F_{\omega} = -\frac{dC}{dz}(V_{dc} - V_{CPD})V_{ac}\sin(\omega_{AC}t) \tag{4.4}$$

Therefore, the feedback loop is employed to nullify F_{ω} by adjusting V_{dc} and measuring the V_{CPD} between the tip and the sample.

4

4.3 Results & discussion

Overview TEM images of different-sized as-deposited Ge NCs are shown in Figure 4.1 (a-c), which also showcase the dependence of the average size evolution on the ratio of the He/Ar gas mixture for a constant total gas flow rate. The insets of Figure 4.1 (a-c) show the corresponding statistical analysis of the size distribution with both the mean size and standard deviation, indicating relatively monodisperse size distributions. These results demonstrate that the size of Ge NCs decreases with increasing the rate of the He gas flow. The mean sizes of as-deposited Ge NCs, as derived from the TEM images, are 36.8 ± 3.5, 32.2 ± 3.0, and 24.4 ± 2.5 nm for 0 (Ar/He: 30/0), 10 (Ar/He: 20/10), and 25 (Ar/He: 5/25) sccm gas flow rates, respectively. Moreover, the different-sized Ge NCs were simultaneously deposited on n-doped Si substrates, where their size was characterized by AFM (Figure 4.1 (d-f)). The resulting mean size calculated by the AFM topography images are 36.0 ± 3.5, 32.5 ± 2.7, and 21.0 ± 2.1 nm, respectively. Table 1 shows a comparison of the results obtained after analysis of the size distributions from both the TEM and AFM images demonstrating a good agreement between both techniques.
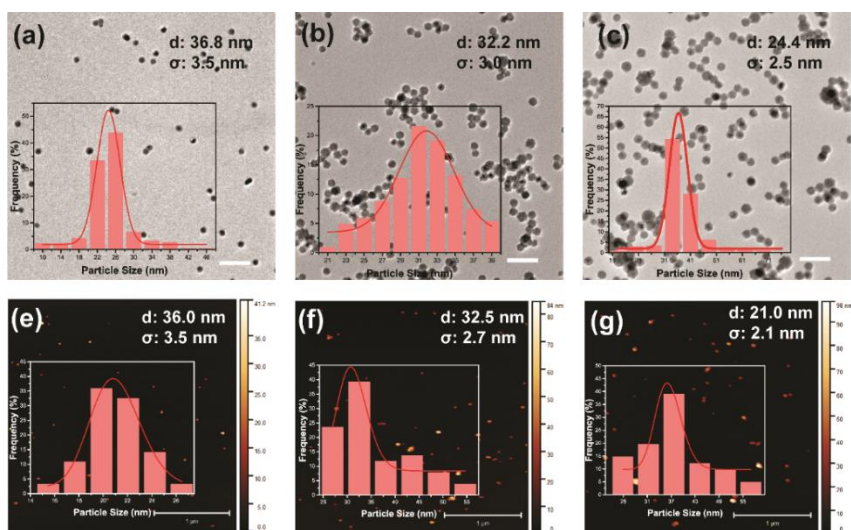
4

Figure 4.1 Size distribution analysis of the Ge NCs deposited by gas-phase condensation via tuning of the Ar/He gas ratio: 30/0 sccm (left column); 20/10 (middle column); and 25/5 (right column). (a-c) Overview TEM images of three different-sized Ge NCs (scale bar is 100 nm); and (e-g) AFM height topography image of the Ge NCs measured in the tapping mode (scale bar is 1 μm). Inset: Size histograms of the Ge NCs with curves fitted to the Gaussian size distribution model.

Table 4.1. Comparison of the resulting mean size of Ge NCs, as obtained from TEM and AFM images, using different He gas flow rates (for a constant total He+Ar gas flow rate) during Ge NCs production.

	Helium gas flow rate (sccm)		
	0	10	25
D_{TEM} (nm)	36.5 ± 3.5	32.2 ± 3.0	24.4 ± 2.5
D_{AFM} (nm)	36.8 ± 3.5	32.2 ± 2.7	21.0 ± 2.1

The explanation for the influence of the He gas flow rate on the size distribution of as-deposited Ge NCs is that the drift velocity of NCs increases by increasing

the He gas rate, which leads to a decrease of the residence time of Ge nanoclusters in the growth area.[44,45] As extensively described in the literature[46,47], the free gas-phase Ge atoms are generated by the impact of accelerated Ar^{+} ions on the target surface resulting in plasma confinement on the target surface. Afterward, the formation process of nanoparticles can be divided into three regimes. In the initial stage, a three-body collision between sputtered Ge atoms and cold Ar atoms induces the formation of unstable nuclei seeds (e.g., dimers), where Ar atoms are more efficient than the He atoms for the formation of the dimer bond. Subsequently, the dimers serve as the nuclei seeds for more Ge atoms in the supersaturated state landing on their surface. The latter contributes to the rapid growth of stable nanoclusters. Finally, the collision between nanoclusters leads to further growth of nanoparticles. Hence, the tunable size of as-deposited Ge nanoparticles can be achieved by interrupting the condensation process at a specific stage. During the condensation process, the primary role of He gas is to serve as the transport gas for nanoclusters, which can entrap the clusters more effectively in the gas streamlines reducing the residence time of clusters in the aggregation volume.[48] However, as stated above, due to the comparatively lower efficiency of He for dimer formation than Ar, as it is shown in Appendix Figure 4.6, with an increase in the supply rate of He gas, the deposition yield of Ge NCs will decrease. Because the function of Ar gas is not only to serve as the carrier gas for drifting nanoparticles to the exit of the source but also as the sputtering gas for facilitating the nucleation process, there is a non-obvious effect of the Ar flow rate on the size of the synthesized nanoparticles.[48]

Furthermore, as in our previous report,[39] the size distribution of Ge NCs can also be tuned by adjusting the magnetic field strength above the target surface. This is achieved by placing copper backing plates with different thicknesses behind the target. Figure 4.2 shows an overview of the tunable size range of as-deposited Ge NCs, from ~36 nm to ~7 nm, by adjusting the two relatively effective parameters (He/Ar gas mixture and magnetic field strength) for

cluster beam deposition. In general, the size-control mechanism of the two methods is similar, which is by the modification of the nucleation process of nanoparticle growth that takes place within the plasma region. Unlike the effect of helium gas flow, a stronger magnetic field induces an increased ionization of gas atoms (Ar^+) and reduces the diffusion rate of Ge atoms away from the source resulting in bigger Ge nanoparticles.[49,50] Note that there is a clear lower limit for the tunable size range for the as-deposited Ge NCs by regulating the individual parameters. For instance, the size of Ge NCs cannot be further decreased when the Ar/He ratio exceeds 25/5 sccm, because dimers cannot be formed by sputtering in pure He gas. Similarly, when the magnetic field above the target surface is too weak, by inserting a relatively thicker backing plate, then achieving a confinement region with stable plasma is extremely challenging and the nuclei "seeds" cannot be formed in the plasma region.

Certainly, the smaller size of Ge nanoparticles can be achieved by integrating these two approaches by both increasing the He gas rate and using copper backing plates. Nevertheless, in this scenario, the as-deposited Ge nanoparticles tend to appear to be in an amorphous state. Because the magnetic field projection on the Ge target decreases by placing a thicker backing plate, the accelerating path of the ionized gas atom will be shortened leading to less kinetic energy for the atoms in the plasma. As previously reported, the lower kinetic energy induces the formation of amorphous $Ge_2Sb_2Te_5$ nanoparticles.[51] On the other hand, in a previous work for the deposition of Si nanoparticles, it was indicated that a critical ratio of the number density of the Si and Ar atoms (ρ_{Si}/ρ_{Ar}) is essential for heating over the crystallization temperature during the condensation process.[44]

Furthermore, the crystalline structure of as-deposited Ge NCs with different sizes was characterized by HRTEM and selected area electron diffraction (SAED). As shown in Figure 4.2 (b-d), the HRTEM images of Ge NCs deposited by three different conditions, which are marked in Figure 4.2 (a), indicate that Ge NCs of all sizes are crystalline. Specifically, Figure 4.2 (b) shows the typical

single crystalline Ge NCs, here, for example, oriented along the [113] zone axis. Consequently, the interplanar d-spacings of the NC calculated from the fast Fourier transform (FFT), as is shown in the inset of Figure 4.2b, are 0.326, 0.283, and 0.202 nm corresponding to the (111), (200), and (220) crystal planes of Ge. In addition, the SAED pattern in Figure 4.2e reveals the {111}, {220} and {311} planes, which demonstrate that the as-deposited Ge NCs have the diamond cubic (*Fd-3m*) crystal structure. Although the majority of as-deposited NCs are single crystals, Ge NC with a partial amorphous state is also found in the HRTEM image in Figure 4.2d. The latter can lead to some deviation of the band structure.
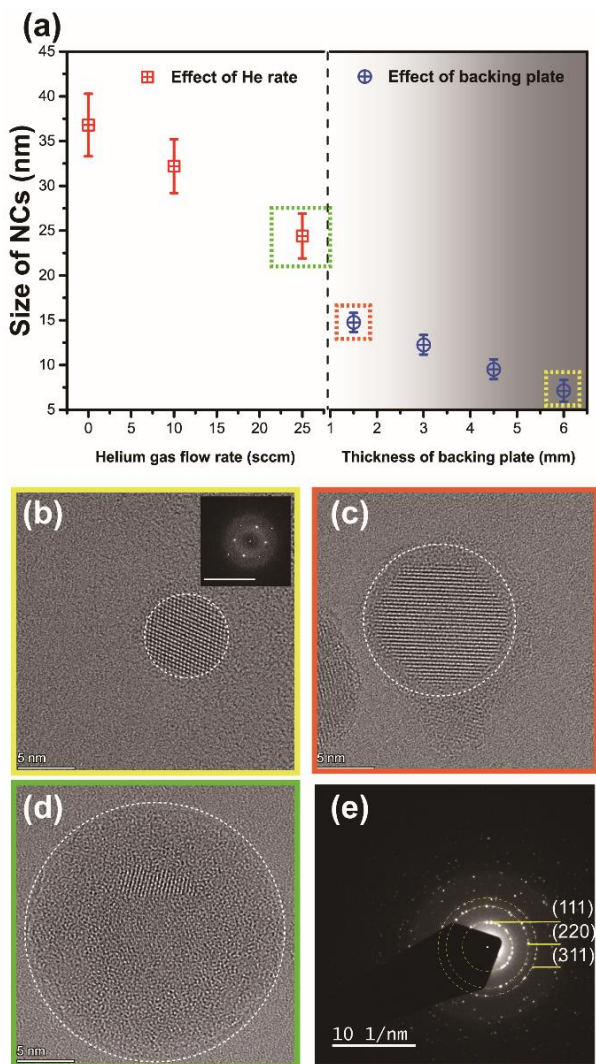
4

Figure 4.2 (a) Average diameter of the Ge NCs synthesized by tuning the He gas flow rate (left panel) and the thickness of the backing plate (right panel), individually. The size distribution analysis is based on TEM images. (b-d) HRTEM images of Ge NCs with different sizes as obtained from different experimental conditions marked in (a). (e) SAED images of as-deposited Ge NCs.

In order to correlate the size of the NCs and electrical properties, Figure 4.3 shows typical AFM topography and the corresponding KPFM images of as-deposited Ge NCs on the n-doped Si substrate. Similarly, as shown in Figure 4.1, monodisperse Ge NCs of ~ 7 nm height are observable in Figure 4.3 (a). Note that due to the convolution effect from the tip shape, the lateral dimensions of Ge NCs are inaccurate to obtain their sizes from the AFM images. Because the majority of as-deposited Ge NCs are monodisperse with a spherical like shape in the TEM images (Figure 4.1), the NCs can be considered as nanodots in the AFM images. Thus, their diameter can be calculated by fitting a parabolic function to the peak of the height (Figure 4.3c). Similarly, the Ge NCs are also distinct in the KPFM images as dark spots (Figure 4.3b). The latter can be interpreted as the negative charging of the Ge NCs by the free carriers from the n-type Si substrate, even if the n-type Si substrate has a very thin native oxide layer. This is because for a very thin oxide layer sufficient charge carrier transport can take place by tunneling through the SiO_X layer, which has been proven by the experiment and simulation.[52] In addition, for the relatively thick oxide layer (2-5 nm), the defects inside the oxide layer can act as the pathway for carrier transportation.[52,53] Furthermore, Figure 4.8 in appendix shows the result of KPFM measurements for Ge NCs deposited on a p-type Si substrate. In contrast to Figure 4.3b, where the Ge NCs manifest as dark features, the Ge NCs deposited on a p-type Si substrate manifest as bright features in the KPFM image. As the Fermi level of the p-type Si is lower than that of the Ge NCs, the positive carries would be transferred from the p-type Si substrate to the Ge NCs. For simplicity, the average (CPD) value of the n-type Si substrate was set to be zero in all results, and a similar approach was applied to measure the ΔCPD of the NCs with respect to the n-type Si substrate (Figure 4.3d).
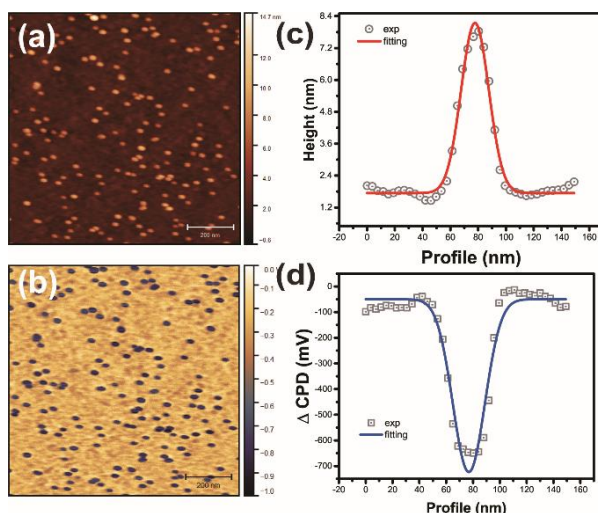
Figure 4.3 Determination of the height and ΔCPD for individual Ge NCs. (a) AFM image and the corresponding ΔCPD map (b) of the Ge NCs deposited on an n-type Si substrate. Example cross-section (c) and surface potential (d) profile of the lines marked in (a, b).

The nominal size range to synthesize Ge NCs by adjusting the ratio of the Ar/He gas rate is roughly 16 ~ 30 nm, and this leads to some NCs with a size above the Bohr exciton radius of Ge (~ 24 nm). According to the quantum confinement effect, the band gap for this size of NCs cannot be tuned by varying their size. In this case, the Ge NCs below 16 nm in diameter, which were deposited by tuning the thickness of the backing plate, were considered for further KPFM measurements. In order to avoid interference from any discrepancy from the substrates and deposition, the Ge NCs with different sizes were deposited together onto single substrates. Figure 4.4(a, b) shows topographic and surface potential fluctuations of the n-type Si covered by Ge NCs, which are simultaneously measured by KPFM. In Figure 4.4c, a size variation between 5 and 16 nm is shown from the fitted results of the height profile for five typical Ge NCs. Accordingly, the corresponding ΔCPD fitted value of these NCs is shown in Figure 4.4d, which reveals a clear correlation with the size of Ge NCs.

To investigate the observed size dependence, a systematic analysis of the ΔCPD values was performed on 30 differently sized NCs. As shown in Figure 4e, where the ΔCPD values of the NCs are plotted as a function of their height (which represents also the size of the NCs), the surface potential fluctuation increases with the decreasing size of the NCs.
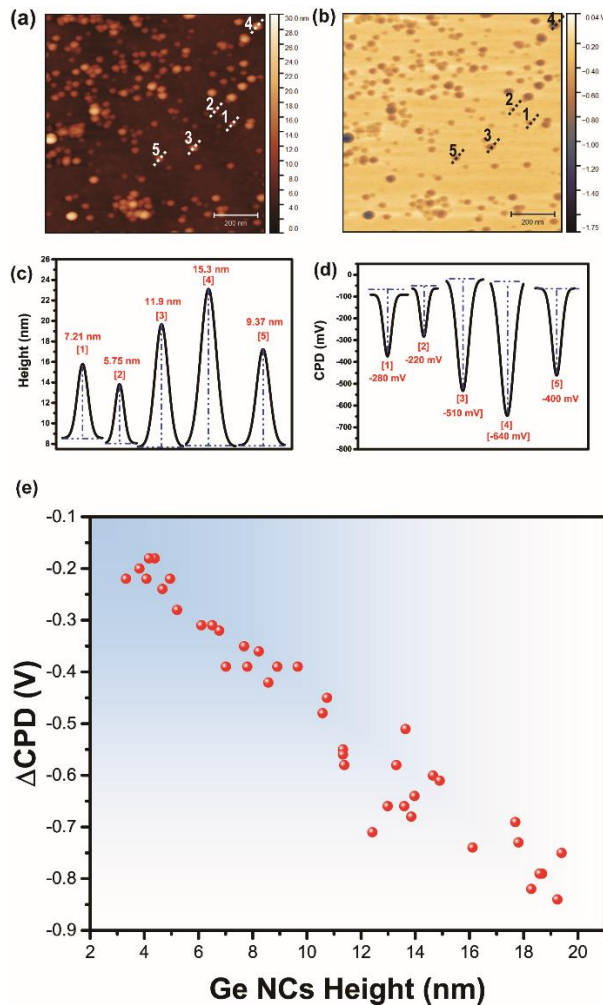
4

Figure 4.4 Simultaneously measured height topography (a) and the

corresponding CPD image (b) of different-sized Ge NCs deposited on an n-type Si substrate. The scale bar is 200 nm. The fitted curves of the cross-section height profiles (c) and the corresponding CPD profiles (d) for five differently sized NCs marked in the (a, b). (e) Dependence of the ΔCPD on the height of the NCs.

The size dependence of the surface potential fluctuation for the Ge NCs can be explained by the quantum confinement theory. Recently, several similar phenomena have been shown by quantum confinement theory for other systems such as Si NCs[11], metal chalcogenide NCs[13], and InAs NCs[14,25]. For instance, by fitting the X-ray photoelectron spectroscopy (XPS) spectrum into a calculated density of states (DOS) model, it was demonstrated that the Fermi position of the PbS QD film depends on the QD size,[54] and similar results were also observed by KPFM measurements[13]. According to the quantum confinement theory, when the size of the Ge NCs is smaller or comparable to the Bohr exciton radius (~ 24 nm), the valence and conduction bands (VB/CB) will shift to yield a wider band gap for the Ge NCs. Consequently, based on the sp^3 tight-binding calculation[55,56], the energies of the VB maximum (E_v) and CB minimum (E_c) as a function of the Ge NCs' diameter can be described quantitatively as follows:

$$E_v(d) = -\frac{15143.8}{d^2 + 6.465d + 2.546} \; meV \qquad (4.5)$$

$$E_c(d) = E_g(bulk) + \frac{11863.7}{d^2 + 2.391d + 4.252} \; meV \qquad (4.6)$$

where d is the diameter (in nm) of the Ge NCs. The calculated trends of the energies for the VB maximum and the CB minimum from the tight-binding model are plotted in Figure 4.5. The latter demonstrates that the shift of the conduction band is, for the size range from 2 to 12 nm considered here, more pronounced than the shift of the valence band. Because no doping elements were incorporated during the deposition process of Ge, the as-deposited Ge NCs can be considered as intrinsic semiconductors with their Fermi level close

to the middle of the band gap. In this case, the Fermi level of the as-deposited Ge NCs will increase with the decrease of their diameter. Because the Fermi level of the n-type Si substrate is pinned, the amount of the negative charge transfer from the substrate to the NCs depends on the variation of the Fermi levels for different sized Ge NCs. Consequently, as the energy diagram in Figure 4.5 illustrates, when the Ge NCs reduce in size, the Fermi level of the NCs is shifting increasingly closer to the Fermi level of the substrate, resulting in the decrease of the electrostatic energy of the ionized Ge NCs. In this case, the size-dependent effect manifests itself by increasing the surface potential fluctuation in KPFM images as the size of the Ge NCs decreases.

Furthermore, Figure 4.9 in appendix, which shows the comparison between the normalized surface potential fluctuation for various sizes Ge NCs and the theoretical model, demonstrates that the surface potential fluctuation for different size Ge NCs is comparable to the calculated results by the tight-binding model. However, the accurate extraction of the electrostatic potential for Ge NCs is affected by several factors including the side-capacitance and experimental conditions. For the lift-mode KPFM, as the magnitude of the measured electrostatic potential is highly dependent on the geometry of probe and lift height, the observed surface potential is a weighted average over all potentials from the localized sample surface. Despite the fact that the optimal experiments for the effects of lift height are carried out and the results are shown in Figure 4.7, the side-capacitance effects cannot be fully excluded during the measurement, making the quantitative analysis for the electrostatic potential relatively difficult. Although the surface potential fluctuation can be interpreted as the charging of the Ge NCs surface states by the free carries from the Si substrate, the behavior of the charge carriers in semiconductors is influenced by the temperature, which causes an offset between the theoretical calculation and the experimental data.

Notably, the difference of the surface potential fluctuations for similar size NCs originate from several deficiencies such as defects and surface oxidation during

their deposition, which can be considered as the trap states for surface charges. Since the topography images of the Ge NCs were performed by tapping mode, these trap states from the deficiencies of Ge NCs could be continuously induced by the charges from the tip, and the surface itself could manifest the surface potential fluctuations due to the local variation in the oxide charges. However, unlike the other semiconductor NCs such as Si NCs, based on the experimental observation (as it is shown in appendix Figure 4.10), the partial Ge NCs remain in un-oxidized states after 1 month of storage in air. Besides, doping for NCs would lead to a reduction of surface potential fluctuations due to the internal passivation mechanism, where the surface states could be occupied by donors of the NCs. In contrast to intrinsic NCs, where the net charges of the NCs generate a dipole perpendicular to the substrate,[57] the doping NCs would form a dipole with a random distribution inside the NCs.
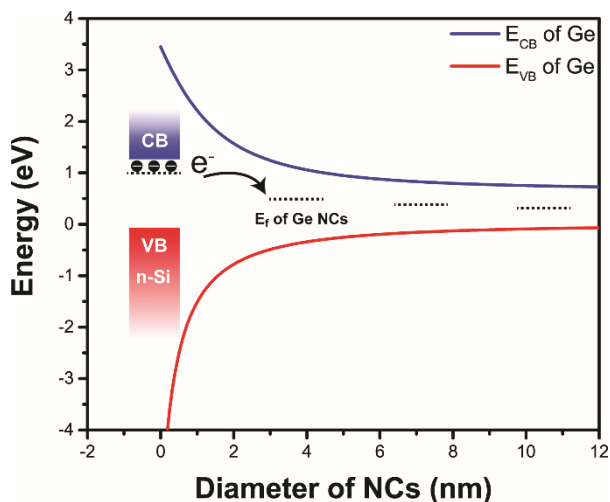

Figure 4.5 The predicted energy of the conduction band maximum and valence band minimum of Ge as a function of the diameter of the NCs based on the tight-binding model calculation. Inset: schematic diagram of the relative position of the Fermi level between the substrate and the Ge NCs with different

sizes.

4.4 Conclusions

In summary, tunable size Ge NCs were synthesized by magnetron-sputtering based cluster beam deposition, where the size of the as-deposited Ge NCs can be finely controlled by He gas flow rates and variable magnetic field configurations above the Ge target surface. Specifically, Ge NCs with a reduced size were obtained by an increase of the He gas flow rate during the deposition, which modifies the condensation process of the NCs. In addition, by comparing the effects of varying the He gas flow rates and the thickness of backing plates between the target and the magnetron head on the growth mechanism of the NCs, we discussed their influence on NC size and crystallinity. The analysis of HRTEM images and SAED patterns revealed that the Ge NCs have the diamond cubic crystal structure. Furthermore, the local electrical properties of different size free-standing Ge NCs were characterized by KPFM. The latter revealed a clear size-dependent relationship of the surface potential of the NCs. In particular, the surface potential fluctuation of n-type Si covered by Ge NCs increased linearly with a decrease of the NCs height in good agreement with the quantum confinement effect. The measured size-dependent relationship can be explained as an increase in the number of charges transferred from the substrate to the NCs, which can be tuned by the size of Ge NCs. Based on the band energy calculation from the tight-binding theory, the energy of the Fermi level of the intrinsic Ge NCs will increase when their size reduces, which is consistent with the experimental results. The results obtained here are essential for pushing forward the understanding of charge exchange at the interfaces between semiconductor QDs and substrates that are of high importance to current and future nanoscale electronic devices.

References

(1)   Wang, Y.; Herron, N. Nanometer-Sized Semiconductor Clusters: Materials Synthesis, Quantum Size Effects, and Photophysical Properties. *J. Phys. Chem.* **1991**, *95,* 525-532.

(2)   Zhang, Q.; Uchaker, E.; Candelaria, S. L.; Cao, G. Nanomaterials for Energy Conversion and Storage. *Chem. Soc. Rev.* **2013**, *42* (7), 3127–3171.

(3)   Takagahara, T.; Takeda, K. Theory of the Quantum Confinement Effect on Excitons in Quantum Dots of Indirect-Gap Materials. *Phys. Rev. B: Condens. Matter Mater. Phys.* **1992**, *46* (23), 15578–15581.

(4)   Prabakar, S.; Shiohara, A.; Hanada, S.; Fujioka, K.; Yamamoto, K.; Tilley, R. D. Size Controlled Synthesis of Germanium Nanocrystals by Hydride Reducing Agents and Their Biological Applications. *Chem. Mater.* **2010**, *22* (2), 482–486.

(5)   Fan, J.; Chu, P. K. Group IV Nanoparticles: Synthesis, Properties, and Biological Applications. *Small* **2010**, *6* (19), 2080–2098.

(6)   Carolan, D. Recent Advances in Germanium Nanocrystals: Synthesis, Optical Properties and Applications. *Prog. Mater. Sci.* **2017,** *90,* 128-158

(7)   Philipp, H. R.; Taft, E. A. Optical Constants of Germanium in the Region 1 to 10 Ev. *Phys. Rev.* **1959**, *113* (4), 1002–1005.

(8)   Ruddy, D. A.; Johnson, J. C.; Smith, E. R.; Neale, N. R. Size and Bandgap Control in the Solution-Phase Synthesis of near-Infrared-Emitting Germanium Nanocrystals. *ACS Nano* **2010**, *4* (12), 7459–7466.

(9)   Wheeler, L. M.; Nichols, A. W.; Chernomordik, B. D.; Anderson, N. C.; Beard, M. C.; Neale, N. R. All-Inorganic Germanium Nanocrystal Films by Cationic Ligand Exchange. *Nano Lett.* **2016**, *16* (3), 1949–1954.

(10)   Liscio, A.; Palermo, V.; Samorì, P. Nanoscale Quantitative Measurement of the Potential of Charged Nanostructures by Electrostatic and Kelvin Probe Force Microscopy: Unraveling Electronic Processes in Complex Materials. *Acc. Chem. Res.* **2010**, *43* (4), 541–550.

(11)   Borowik; Kusiaku, K.; Deresmes, D.; Théron, D.; Diesinger, H.; Mélin, T.; Nguyen-Tran, T.; Roca I Cabarrocas, P. Mapping Charge Transfers between Quantum Levels Using Noncontact Atomic Force Microscopy. *Phys. Rev. B: Condens. Matter Mater. Phys.* **2010**, *82* (7), 073302.

(12)   Mora-Seró, I.; Giménez, S.; Fabregat-Santiago, F.; Gómez, R.; Shen, Q.; Toyoda, T.; Bisquert, J. Recombination in Quantum Dot Sensitized Solar Cells. *Acc. Chem. Res.* **2009**, *42* (11), 1848–1857.

(13)   Benetti, D.; Cui, D.; Zhao, H.; Rosei, F.; Vomiero, A. Direct Measurement of Electronic Band Structure in Single Quantum Dots of Metal Chalcogenide Composites. *Small* **2018**, *14* (51), 1801668-1801677.

4

(14)   Yamauchi, T.; Tabuchi, M.; Nakamura, A. Size Dependence of the Work Function in InAs Quantum Dots on GaAs(001) as Studied by Kelvin Force Probe Microscopy. *Appl. Phys. Lett.* **2004**, *84* (19), 3834–3836.

(15)   Tekiel, A.; Miyahara, Y.; Topple, J. M.; Grutter, P. Room-Temperature Single-Electron Charging Detected by Electrostatic Force Microscopy. *ACS Nano* **2013**, *7* (5), 4683–4690.

(16)   Zhang, Y.; Zherebetskyy, D.; Bronstein, N. D.; Barja, S.; Lichtenstein, L.; Schuppisser, D.; Wang, L. W.; Alivisatos, A. P.; Salmeron, M. Charge Percolation Pathways Guided by Defects in Quantum Dot Solids. *Nano Lett.* **2015**, *15* (5), 3249–3253.

(17)   Melitz, W.; Shen, J.; Kummel, A. C.; Lee, S. Kelvin Probe Force Microscopy and Its Application. *Surf. Sci. Rep.* **2011,** *66,* 1-27.

(18)   Mélin, T.; Deresmes, D.; Stiévenard, D. Charge Injection in Individual Silicon Nanoparticles Deposited on a Conductive Substrate. *Appl. Phys. Lett.* **2002**, *81* (26), 5054–5056.

(19)   Clack, N. G.; Salaita, K.; Groves, J. T. Electrostatic Readout of DNA Microarrays with Charged Microspheres. *Nat. Biotechnol.* **2008**, *26* (7), 825–830.

(20)   Banin, U.; Cao, Y. W.; Katz, D.; Millo, O. Identification of Atomic-like Electronic States in Indium Arsenide Nanocrystal Quantum Dots. *Nature* **1999**, *400* (6744), 542–544.

(21)   Millo, O.; Balberg, I.; Azulay, D.; Purkait, T. K.; Swarnakar, A. K.; Rivard, E.; Veinot, J. G. C. Direct Evaluation of the Quantum Confinement Effect in Single Isolated Ge Nanocrystals. *J. Phys. Chem. Lett.* **2015**, *6* (17), 3396–3402.

(22)   Wolf, O.; Dasog, M.; Yang, Z.; Balberg, I.; Veinot, J. G. C.; Millo, O. Doping and Quantum Confinement Effects in Single Si Nanocrystals Observed by Scanning Tunneling Spectroscopy. *Nano Lett.* **2013**, *13* (6), 2516–2521.

(23)   Dabera, G. Di. M. R.; Walker, M.; Sanchez, A. M.; Pereira, H. J.; Beanland, R.; Hatton, R. A. Retarding Oxidation of Copper Nanoparticles without Electrical Isolation and the Size Dependence of Work Function. *Nat. Commun.* **2017**, *8* (1), 1894.

(24)   Zhang, Y.; Pluchery, O.; Caillard, L.; Lamic-Humblot, A. F.; Casale, S.; Chabal, Y. J.; Salmeron, M. Sensing the Charge State of Single Gold Nanoparticles via Work Function Measurements. *Nano Lett.* **2015**, *15* (1), 51–55.

(25)   Biaye, M.; Amit, Y.; Gradkowski, K.; Turek, N.; Godey, S.; Makoudi, Y.; Deresmes, D.; Tadjine, A.; Delerue, C.; Banin, U.; et al. Doped Colloidal InAs Nanocrystals in the Single Ionized Dopant Limit. *J. Phys. Chem. C* **2019**, *123* (23), 14803–14812.

(26)   Xu, J.; Zhang, P.; Li, W.; Chen, K.; Xu, J. Nanoscale Quantification of Charge Injection and Transportation Process in Si-Nanocrystal Based Sandwiched Structure. *Nanoscale* **2013**, *5* (20), 9971–9977.

(27)   Fuchs, F.; Caffy, F.; Demadrille, R.; Meíin, T.; Grévin, B. G. High-

Resolution Kelvin Probe Force Microscopy Imaging of Interface Dipoles and Photogenerated Charges in Organic Donor– Acceptor Photovoltaic Blends. *ACS Nano* **2016**, *10*, 739−746.

(28) Shusterman, S.; Raizman, A.; Sher, A.; Parltiel, Y.; Schwarzman, A.; Lepkifker, E.; Rosenwaks, Y. Nanoscale Mapping of Strain and Composition in Quantum Dots Using Kelvin Probe Force Microscopy. *Nano Lett.* **2007**, *7* (7), 2089−2093.

(29) Banerjee, S.; Salem, M. A.; Oda, S. Conducting-Tip Atomic Force Microscopy for Injection and Probing of Localized Charges in Silicon Nanocrystals. *Appl. Phys. Lett.* **2003**, *83* (18), 3788−3790.

(30) Singha, R. K.; Manna, S.; Bar, R.; Das, S.; Ray, S. K. Surface Potential, Charging and Local Current Transport of Individual Ge Quantum Dots Grown by Molecular Beam Epitaxy. *Appl. Surf. Sci.* **2017**, *407*, 418−426.

(31) Kondratenko, S. V.; Lysenko, V. S.; Kozyrev, Y. N.; Kratzer, M.; Storozhuk, D. P.; Iliash, S. A.; Czibula, C.; Teichert, C. Local Charge Trapping in Ge Nanoclustersdetected by Kelvin Probe Force Microscopy. *Appl. Surf. Sci.* **2016**, *389*, 783−789.

(32) Henderson, E. J.; Seino, M.; Puzzo, D. P.; Ozin, G. A. Colloidally Stable Germanium Nanocrystals for Photonic Applications. *ACS Nano* **2010**, *4* (12), 7683−7691.

(33) Henderson, E. J.; Hessel, C. M.; Veinot, J. G. C. Synthesis and Photoluminescent Properties of Size-Controlled Germanium Nanocrystals from Phenyl Trichlorogermane-Derived Polymers. *J. Am. Chem. Soc.* **2008**, *130* (11), 3624−3632.

(34) Muthuswamy, E.; Iskandar, A. S.; Amador, M. M.; Kauzlarich, S. M. Facile Synthesis of Germanium Nanoparticles with Size Control: Microwave versus Conventional Heating. *Chem. Mater.* **2013**, *25* (8), 1416−1422.

(35) Tabatabaei, K.; Holmes, A. L.; Newton, K. A.; Muthuswamy, E.; Sfadia, R.; Carter, S. A.; Kauzlarich, S. M. Halogen-Induced Crystallinity and Size Tuning of Microwave Synthesized Germanium Nanocrystals. *Chem. Mater.* **2019**, *31* (18), 7510−7521.

(36) Zaitseva, N.; Dai, Z. R.; Grant, C. D.; Harper, J.; Saw, C. Germanium Nanocrystals Synthesized in High-Boiling-Point Organic Solvents. *Chem. Mater.* **2007**, *19* (21), 5174−5178.

(37) Gerung, H.; Bunge, S. D.; Boyle, T. J.; Brinker, C. J.; Han, S. M. Anhydrous Solution Synthesis of Germanium Nanocrystals from the Germanium(II) Precursor Ge[N(SiMe3)2]2. *Chem. Commun.* **2005**, No. 14, 1914−1916.

(38) Ahadi, A. M.; Hunter, K. I.; Kramer, N. J.; Strunskus, T.; Kersten, H.; Faupel, F.; Kortshagen, U. R. Controlled Synthesis of Germanium Nanoparticles by Nonthermal Plasmas. *Appl. Phys. Lett.* **2016**, *108* (9), 093105.

(39) Zhu, X.; Ten Brink, G. H.; De Graaf, S.; Kooi, B. J.; Palasantzas, G. Gas-Phase Synthesis of Tunable-Size Germanium Nanocrystals by Inert Gas

4

Condensation. *Chem. Mater.* **2020**, *32* (4), 1627–1635.

(40) Cardoso, J.; Marom, S.; Mayer, J.; Modi, R.; Podestà, A.; Xie, X.; van Huis, M. A.; Di Vece, M. Germanium Quantum Dot Grätzel-Type Solar Cell. *Phys. Status Solidi A.* **2018**, *215* (24), 1800570.

(41) Zerweck, U.; Loppacher, C.; Otto, T.; Grafström, S.; Eng, L. M. Accuracy and Resolution Limits of Kelvin Probe Force Microscopy. *Phys. Rev. B: Condens. Matter Mater. Phys.* **2005**, *71* (12), 125424.

(42) Jacobs, H. O.; Leuchtmann, P.; Homan, O. J.; Stemmer, A. Resolution and Contrast in Kelvin Probe Force Microscopy. *J. Appl. Phys.* **1998**, *84* (3), 1168–1173.

(43) Borowik, Ł.; Kusiaku, K.; Théron, D.; Mélin, T. Calculating Kelvin Force Microscopy Signals from Static Force Fields. *Appl. Phys. Lett.* **2010**, *96* (10), 103119.

(44) Zhao, J.; Singh, V.; Grammatikopoulos, P.; Cassidy, C.; Aranishi, K.; Sowwan, M.; Nordlund, K.; Djurabekova, F. Crystallization of Silicon Nanoclusters with Inert Gas Temperature Control. *Phys. Rev. B: Condens. Matter Mater. Phys.* **2015**, *91* (3), 035419.

(45) Grammatikopoulos, P.; Steinhauer, S.; Vernieres, J.; Singh, V.; Sowwan, M. Nanoparticle Design by Gas-Phase Synthesis. *Adv. Phys. X* **2016**, *1* (1), 81–100.

(46) Yves Huttel. *Gas-Phase Synthesis of Nanoparticles*; John Wiley & Sons: New York, 2017.

(47) Haberland, H.; Mall, M.; Moseler, M.; Qiang, Y.; Reiners, T.; Thurner, Y. Filling of Micron-sized Contact Holes with Copper by Energetic Cluster Impact. *J. Vac. Sci. Technol. A Vacuum, Surfaces, Film.* **1994**, *12* (5), 2925–2930.

(48) Khojasteh, M.; Kresin, V. V. Influence of Source Parameters on the Growth of Metal Nanoparticles by Sputter-Gas-Aggregation. *Appl. Nanosci.* **2017**, *7* (8), 875–883.

(49) Vernieres, J.; Steinhauer, S.; Zhao, J.; Chapelle, A.; Menini, P.; Dufour, N.; Diaz, R. E.; Nordlund, K.; Djurabekova, F.; Grammatikopoulos, P.; et al. Gas Phase Synthesis of Multifunctional Fe-Based Nanocubes. *Adv. Funct. Mater.* **2017**, *27* (11), 1605328.

(50) Palmer, R. E.; Cai, R.; Vernieres, J. Synthesis without Solvents: The Cluster (Nanoparticle) Beam Route to Catalysts and Sensors. *Acc. Chem. Res.* **2018**, *51* (9), 2296–2304.

(51) Chen, B.; Ten Brink, G. H.; Palasantzas, G.; Kooi, B. J. Size-Dependent and Tunable Crystallization of GeSbTe Phase-Change Nanoparticles. *Sci. Rep.* **2016**, *6* (1), 39546.

(52) Zhang, Z.; Zeng, Y.; Jiang, C.-S.; Huang, Y.; Liao, M.; Tong, H.; Al-Jassim, M.; Gao, P.; Shou, C.; Zhou, X.; et al. Carrier Transport through the Ultrathin Silicon-Oxide Layer in Tunnel Oxide Passivated Contact (TOPCon) c-Si Solar Cells. *Sol. Energy Mater. Sol. Cells* **2018**, *187*, 113–122.

(53) Marchat, C.; Connolly, J. P.; Kleider, J.-P.; Alvarez, J.; Koduvelikulathu,

L. J.; Puel, J. B. KPFM Surface Photovoltage Measurement and Numerical Simulation. *EPJ Photovoltaics* **2019**, *10*, 3.

(54)   Miller, E. M.; Kroupa, D. M.; Zhang, J.; Schulz, P.; Marshall, A. R.; Kahn, A.; Lany, S.; Luther, J. M.; Beard, M. C.; Perkins, C. L.; et al. Revisiting the Valence and Conduction Band Size Dependence of PbS Quantum Dot Thin Films. *ACS Nano* **2016**, *10* (3), 3302–3311.

(55)   Niquet, Y. M.; Allan, G.; Delerue, C.; Lannoo, M. Quantum Confinement in Germanium Nanocrystals. *Appl. Phys. Lett.* **2000**, *77* (8), 1182–1184.

(56)   Niquet, Y.; Delerue, C.; Allan, G.; Lannoo, M. Method for Tight-Binding Parametrization: Application to Silicon Nanostructures. *Phys. Rev. B: Condens. Matter Mater. Phys.* **2000**, *62* (8), 5109–5116.

(57)   Mélin, T.; Diesinger, H.; Deresmes, D.; Stiévenard, D. Probing Nanoscale Dipole-Dipole Interactions by Electric Force Microscopy. *Phys. Rev. Lett.* **2004**, *92* (16), 166101.
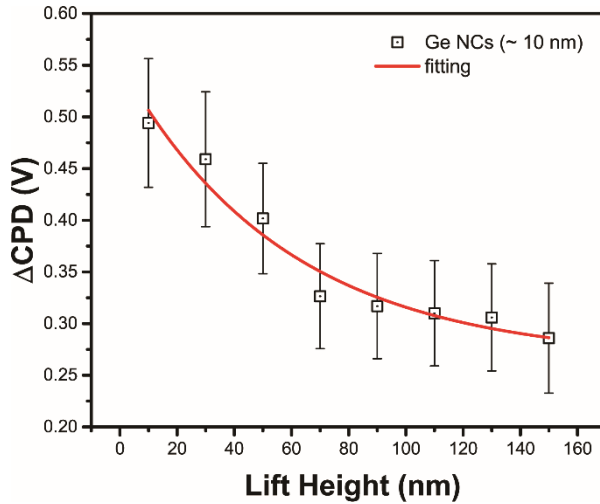
4

Appendix

Figure 4.6 Measured CPD of Ge NCs as a function of the lift height during the KPFM measurement. The red solid line is single exponential fitting.
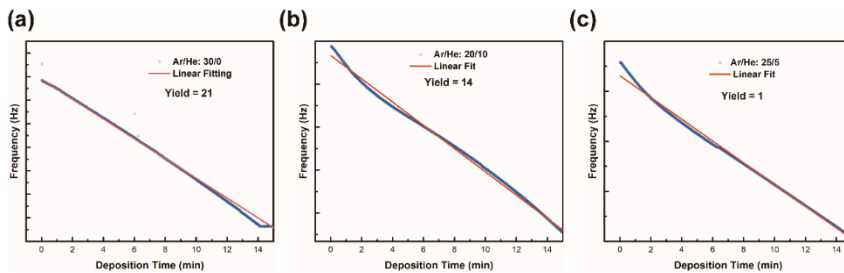

Figure 4.7 The oscillation frequency shift of the QCM (Quartz Crystal Microbalance) as a function of the sputtering time. The deposition yield is calculated from the slope of linear fitting for different Ar/He gas flow ratios: (a) 30/0 sccm; (b) 20/10 sccm; (c) 25/5 sccm.
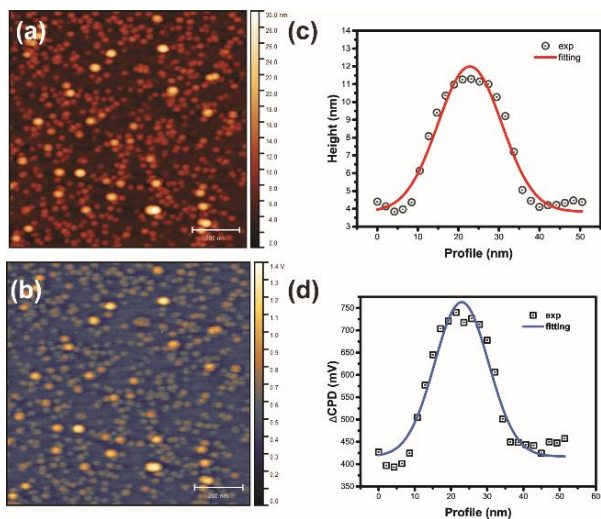
Figure 4.8 (a) AFM image and the corresponding ΔCPD map (b) of the Ge NCs deposited on p-type Si substrate. A height profile cross-section is also shown in (c) and the corresponding surface potential in (d) for the lines marked in (a, b).
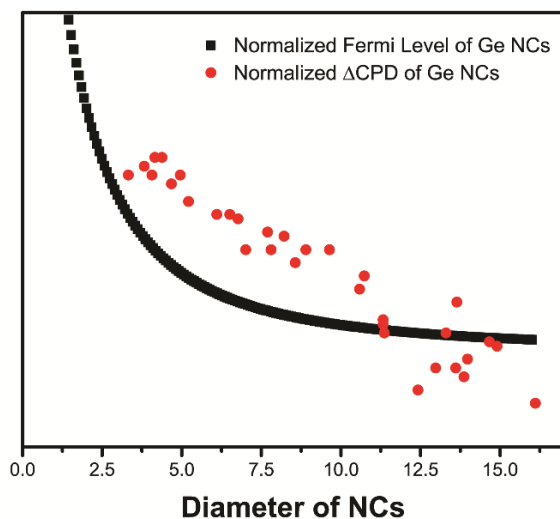

Figure 4.9 Comparison between the normalized ΔCPD of Ge NCs, and the calculated Fermi Level by the tight-binding model.
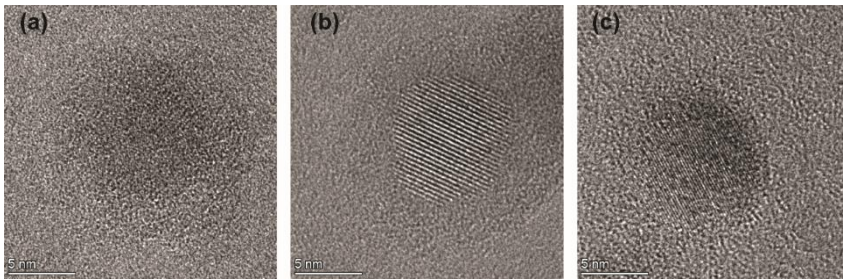
Figure 4.10 Various states of Ge NCs after 1 month storage in air. (a) fully oxidized, (b) partial oxidized, and (c) un-oxidized Ge NCs respectively.

4

5

Crystallization Study of Antimony Nanoparticles Synthesized by Inert Gas Condensation

5

Abstract

Nanostructured phase change materials (PCMs), such as nanoparticles and nanowires, are viewed as promising candidates for non-volatile memory to address fundamental issues related to downscaling towards higher device densities. However, one of the fundamental challenges in scaling the conventional compounds like $Ge_2Sb_2Te_5$ into nanostructures is the undesirable deviations from the optimal chemical composition during the switching. Instead of complex alloy optimization to improve PCM performance, it is also possible to work with pure antimony (Sb). However, for Sb it is known that under normal conditions, i.e. standard film thickness of at least 10 nm, the amorphous phase is not sufficient stable against spontaneous crystallization at room temperature. However, recent work now demonstrates that confinement of Sb in ultra-thin films down to 3 nm in the memory can greatly improve amorphous phase stability. Still, all work on Sb in this respect only focus on thin films. Here the focus is on, monoatomic Sb nanoparticles, which were synthesized by magnetron-sputtering inert gas condensation. The phase of as-deposited Sb NPs can be controlled between crystalline and amorphous states by varying the applied discharge current. Furthermore, the size distribution analysis based on transmission electron microscopy (TEM) images demonstrates that decreasing the discharge current during the deposition reduces the diameter of the Sb NPs. Crystallization studies of amorphous Sb NPs were performed by in-situ heating within the TEM, demonstrating that the amorphous state of Sb can be stabilized well by nanostructure confinement in NPs.

5

5.1 Introduction

In recent decades, the advancement of information technology drives the exponentially increasing demands for data storage and processing. To satisfy these needs, research increasingly starts to dedicate itself to the development of non-volatile memory for data storage.[1] In this regard, phase change materials (PCMs) are promising candidates, since the large contrast in electrical resistivity and optical reflectivity between the amorphous and crystalline phases can be used to store the "0" and "1" binary digital information.[2] Meanwhile, the rapid and rewriteable switching between the two states of the PCMs can be utilized to improve the speed of data storage.

The existing PCMs can be categorized into three classes based on their composition in the Ge-Sb-Te phase diagram. The first class is the ternary GeSbTe alloy lying on the pseudo-binary GeTe-Sb_2Te_3 tie line like the $Ge_2Sb_2Te_5$ (GST). The second class is the Ge or In doped Sb alloy, such as the $Ge_{15}Sb_{85}$. The crystallization mechanism of these two families is nucleation-driven via the formation of a critical nuclei. The third class is the SbTe alloy near the eutectic composition with Ag and In doping such as the $Ag_4In_3Sb_{67}Te_{26}$ (AIST), where the crystallization is growth-driven occurring from the crystalline interface. In order to improve the performance of PCMs memory in terms of the data storage density, access time and power efficiency, the memory unit of PCMs device needs to be continued miniaturized, as the sub-nanosecond switching time can be achieved for the nanoscale PCMs memory cell.[3] However, the risk of composition deviation for conventional alloys (e.g. GST and AIST), which not only degrades the performance of memory devices after millions of switching cycles but also impedes the further application in in-memory or neuromorphic-computing chips. Also, achieving precise stoichiometry for conventional PCMs devices, which are aggressively miniature down to nanoscales is a major challenge.

The monatomic metal materials with phase change properties, such as antimony (Sb) and Tellurium (Te)[4], can be dedicated to address the challenges

described above. At room temperature, pure amorphous Sb is very unstable, crystallizing spontaneously at room temperature and even 'explosively' for thicker films. However, recent works have demonstrated that an ultra-thin Sb film (3~10 nm) with interfacial nano-confinement exhibits a stable amorphous state at room temperature. The property of phase transition between the crystalline and amorphous state[5] can be used as non-volatile memory, neuromorphic computing device[6], and as an optoelectronic device[7]. The benefit by the rapid crystallization of Sb and the operation speed of such a memory device, which is currently constrained by the crystallization process of the PCMs, can be improved. Geometrical confinement effects, which severely restricted the structural dynamics near the glass transition point, can be explained as the origin of stabilizing the glassy state of the Sb thin film.[8,9]

Nevertheless, some further challenge of Sb as PCM, especially that the amorphous state can only be stabilized for around 100 seconds at the operation temperature (60-70 °C), needs to be addressed before Sb can be actually used in non-volatile devices.[5,10] Three-dimensional nano-confinement seems to be one of the possible solutions for stabilizing the amorphous state of Sb further, as the local mobility of atoms could be greatly restrained by narrowing the confinement between interfaces with neighboring materials.[9] Indeed, for GeTe NPs the crystallization temperature (T_c) strongly increase for decreasing size of NPs. However, for GST NPs the Tc decreases very weakly with decreasing NP size.[11] In addition, three-dimensional nanostructures are relatively hard to fabricate via top-down techniques. In this case, the gas-phase NPs were synthesized by a bottom-up approach, i.e. using gas phase aggregation nanocluster beam, where the size distribution, shape, and phase states of the as-deposited NPs can be readily controlled.[12] Hence, this approach serves as a model system for studying the properties of phase transitions in PCM NPs.

5.2 Experimental methods

Synthesis of Sb nanoparticles

The Sb nanoparticles with different phase states and size distribution were deposited by a home-modified cluster beam system based on magnetron sputtering (obtained from Mantis Deposited Ltd.). Both the main chamber and the aggregation chamber were initially evacuated to a base pressure of around 1×10^{-7} mbar to prevent oxidation of NPs during the deposition. With the help of a magnetic field, the supersaturated Sb vapor was formed by sputtering the Sb target (purity of 99.99% and 50.8 mm diameter) with Ar gas (purity of 99.9999%), which subsequently condensates into the nuclei that gradually grow to form Sb NPs. Note that the NPs with different phase states were prepared by varying the sputtering ion current corresponding to the sputtering power. Carbon TEM grids as the substrates for NPs deposition were placed inside the main chamber during the deposition. A quartz crystal microbalance (QCM) was mounted next to the substrate holder for monitoring the deposition yield.

Characterization of Sb NPs

The morphology and size distribution of Sb NPs were after deposition quickly (typically within one day) analyzed by transmission electron microscopy (TEM, JEOL 2010). The phase state of as-deposited Sb NPs was characterized by combining selected area electron diffraction (SAED) with high-resolution TEM (HR-TEM). The phase transition of as-deposited amorphous Sb NPs was studied via in-situ heating in TEM, where a heating holder (Gatan Model 625) with a temperature controller (Gatan Model 901) was used for this purpose. To mitigate the effect of the electron beam on the crystallization process during heating, the electron beam was moved to the window edge of the copper grid. Specifically, the SAED pattern of Sb NPs was obtained when the temperature of holder reached to the preset point for 5 minutes, and the electron beam was shifted to the grid's window edge at other times.

5.3 Results and Discussion

Control of crystallinity

5

Regulating the phase state of Sb NPs is crucial for studying NP crystallization. Nevertheless, directly synthesizing amorphous Sb NPs by the wet chemical method is relatively challenging due to the lack of a stable amorphous state for Sb at room temperature. Therefore the Sb NPs were synthesized by magnetron-sputtering inert gas condensation, which has been demonstrated that the phase state and size distribution of as-deposited NPs can be easily controlled during the deposition.[11,13] As it is shown in Figure 5.1, both crystalline and amorphous NPs were successfully deposited by varying the discharge current applied for the sputtering, resulting in a change in system power input. Because the deposition is operated with a very low discharge current, the temperature of the plasma zone remains below the melting temperature of Sb and sputtered Sb clusters, which can be considered in a solid-state, randomly coalesce to form NPs. In such conditions, the energy of nanoparticles acquired from the plasma zone is insufficient to surpass the energy barrier of crystalline transition, in which the amorphous phase NPs were deposited analogously to sputtered amorphous films.

The phase state of as-deposited Sb NPs was determined by high-resolution transmission electron microscopy (HRTEM). Specifically, the crystalline structure of as-deposited Sb NPs can be verified as trigonal (*R-3m*) by indexing the electron pattern in Figure 5.1 (c), and the line profile by azimuthal integrating the diffraction spots as it is shown in the inset of Figure 5.1 (c) indicates that the measured inter-planar spacing of Sb NPs d_{012}, d_{-120} and d_{024} are 0.311 nm, 0.218 nm, and 0.153 nm, respectively. Figure 5.1 (e), on the other hand, displays the amorphous character of Sb NPs deposited by low discharge current due to lack of lattice fringes, which is also corroborated by the diffusion halo pattern of electron diffraction displayed in Figure 5.1 (f).
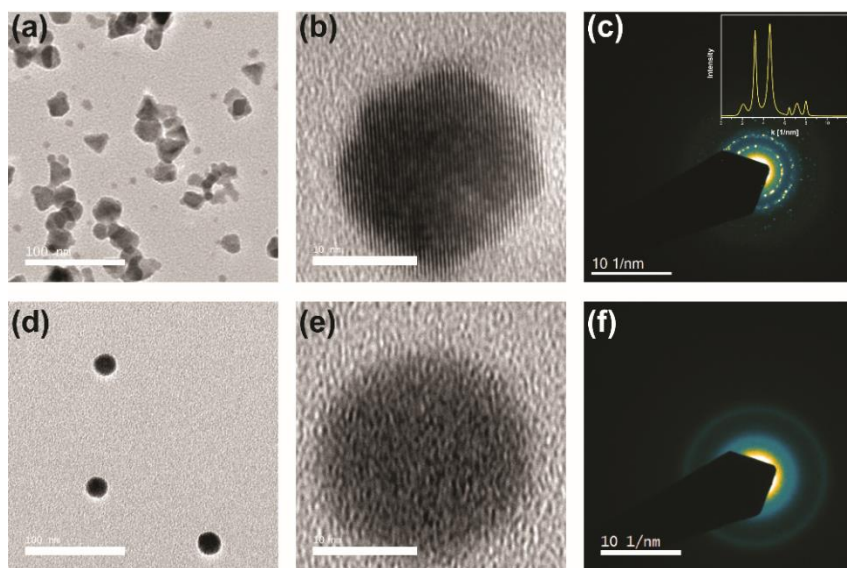
5

Figure 5.1 Morphology and crystalline structure characterization of as-deposited Sb NPs (top panel: crystalline Sb NPs; bottom panel: amorphous Sb NPs). (a, d) bright-field TEM images of as-deposited Sb NPs, (b, e) High-resolution TEM images of as-deposited NPs, (c,f) SAED pattern of as-deposited NPs.

Interestingly, in addition to the influence on the phase state of as-deposited Sb NPs, subtle variations in applied discharge current can also have a major effect on the shape of the as-deposited NPs by comparing the TEM images between crystalline and amorphous NPs, which is likely similar to the one observed in synthesizing gas-phase Fe NPs.[14] Consequently, Zhao et al. elucidated the formation mechanisms of shape-dependent Fe NPs during deposition by employing a combination of molecular dynamics and kinetic Monte Carlo simulation.[15] In general, the ultimate shape of as-deposited Sb NPs is determined by the competition between sputtered rates of Sb atoms from the target surface and the surface diffusion rates of atoms on certain planes of existing nanoclusters. Since the high discharge current applied for the deposition causes a high plasma temperature[16], the rates of sputtered Sb atoms are accelerated. Meanwhile, though, the surface diffusion rates of newly

5

sputtered atoms, which land on the surface of existing nanoclusters, are also enhanced, allowing the equilibrium shape to be achieved. In this case, the majority of Sb NPs deposited by a high discharge current had a trigonal shape as it is shown in Figure 5.1 (a). However, for amorphous Sb NPs as it is shown in Figure 5.1 (b), which were deposited by an extremely low discharge current, the energy of sputtered Sb atoms is insufficient to diffuse on the specific planes of nanoclusters, resulting in as-deposited Sb NPs with a spherical shape to minimize surface energy. In addition, the absence of a core-shell structure in the HRTEM images, as shown in Figure 5.1 (b, e), indicates that the NPs were not significantly oxidized.

Analysis of the size distribution

Figure 5.2 shows typical TEM images of as-deposited Sb NPs synthesized with varied discharge currents, as well as their corresponding size distribution, which exhibits a well-dispersed distribution fitted by a Gaussian rather than log-normal function. The fitted mean diameters of as-deposited Sb NPs were 18.9 ± 2.9, 12.7 ± 1.3, and 13.4 ± 1.1 nm for discharge currents 0.15, 0.075, and 0.055 A, respectively. Notably, because the plasma is highly unstable when 0.055 A is used as discharge current, a relatively large current (0.2 A) was used to initiate the plasma to attain a reasonable deposition yield, resulting in the distinct bimodal distribution observed in Figure 5.2 (g, h). In general, when the discharge current for deposition is reduced, the size of as-deposited Sb NPs is projected to decrease. At higher discharge current, as the amount of sputtered Sb atoms in the plasma zone is increased, sputtered atoms tend to form large Sb NPs, a feature that is also observed in synthesizing Ni[17] and Ag[18] NPs. Furthermore, as it is shown in Figure 5.2 (c, f, i), the amorphous character and the close to spherical shape persist for this range of discharge currents during deposition.
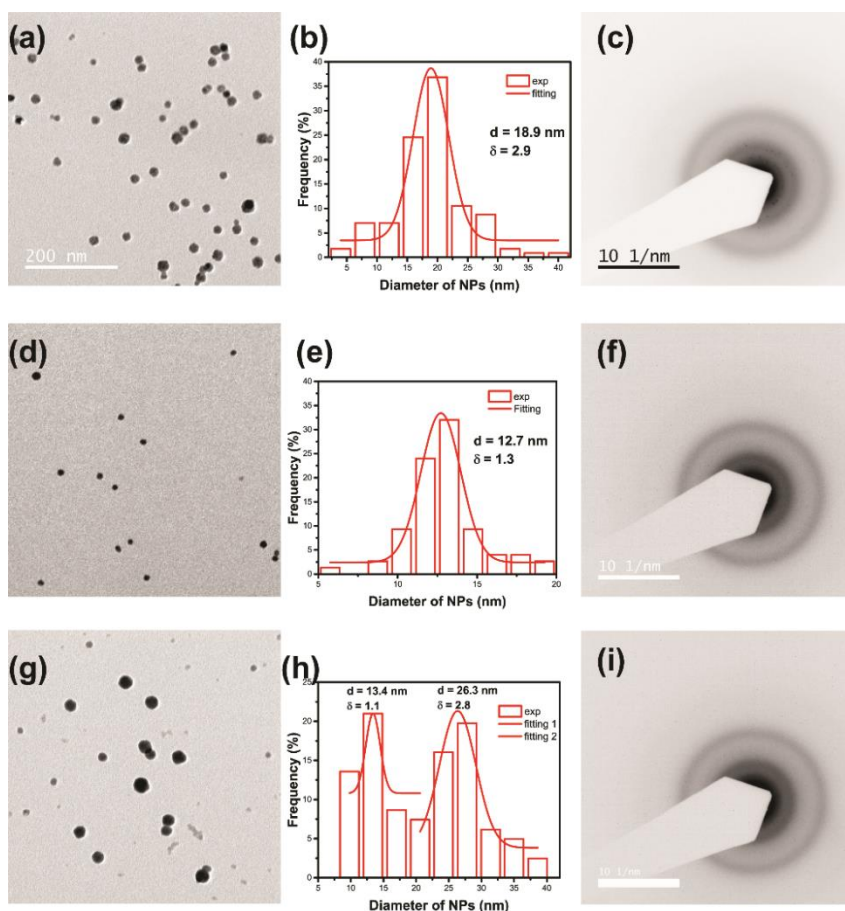
5

Figure 5.2 Size distribution and structure analysis of NPs deposited with different current inputs. (top panel: 0.15 A; middle panel: 0.075 A; bottom panel: 0.055 A)

When the Ar gas flow is constant, the dc voltage is only sensitive to the discharge current, resulting in a general reduction in sputtering power when decreasing the discharge current.[17] Because the amount of sputtered Sb atoms is highly dependent on the magnetron power, increasing the magnetron power results in faster cluster nucleation rates.[19] Inversely, as it is shown in Figure 5.3, the deposition yield of Sb NPs drops dramatically with the reduction of the
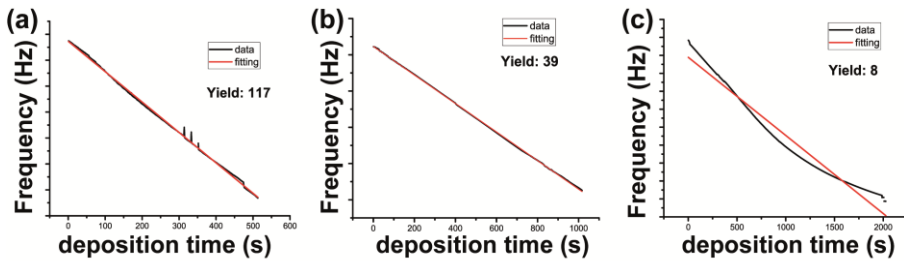
5

discharge current.

Figure 5.3 The oscillation frequency shift of the QCM (Quartz Crystal Microbalance) as a function of the sputtering time. The deposition yield is fitted from the slope for different current inputs: (a) 0.15 A; (b) 0.075 A; (c) 0.055 A.

Crystallization of as-deposited Sb NPs

As stated above, the Sb NPs for evaluating crystallization characteristics were deposited using 0.075 A as a discharge current to obtain amorphous state NPs, and a satisfactory deposition yield. Since it is directly related to the stability of the amorphous phase, crystallization is one of the most important properties to investigate when phase change materials are scaled down to nanometer sizes. However, because of the relatively low mass of nanoparticles, conventional methods, such as differential scanning calorimetry, cannot assess the crystallization properties of Sb NPs. Therefore, the crystallization process of Sb NPs was carried out by in-situ heating in the TEM. Specifically, after heating inside the TEM chamber, the diffusion halo for amorphous Sb NPs transferred into diffraction spots in the SAED pattern, as illustrated in Figure 5.4. Moreover, the shape of Sb NPs changes from close to spherical to trigonal after heating. In particular, Figure 5.4 (h) shows the transient state of Sb NPs during in-suit heating, in which the left part of the Sb NP appears to have the trigonal shape, as indicated by the yellow line of Figure 5.4 (h), while the right part remains spherical.
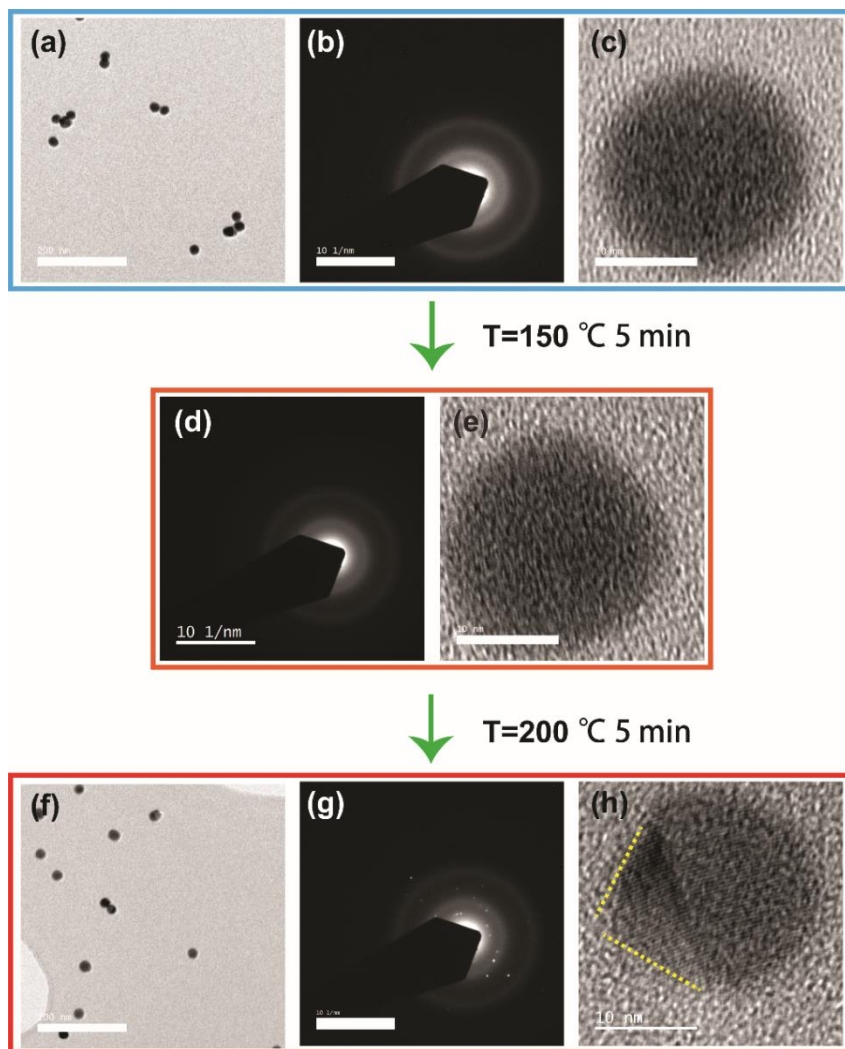
Figure 5.4 Crystallization of Sb NPs in TEM using in-situ heating (top panel shows amorphous as-deposited Sb NPs; middle panel shows the crystallinity of Sb NPs after heating 5 minutes at 150 ℃; the bottom panel shows the crystalline Sb NPs following heating at 200 ℃). In particular, (a, f), (b, d, g), and (c, e, h) show bright-field TEM images, SAED patterns, and high-resolution TEM images, respectively.

Due to a lack of crystallization data from the series temperature heating experiments, a precise crystallization temperature (T_c) of Sb NPs could not be derived from the results of in-situ heating. However, as it is shown in Figure 5.4 (d, e), since the Sb NPs remain in an amorphous state after 5 minutes heating at 150 °C, the T_c of Sb NPs can be demonstrated to be in the range from 150 to 200 °C, which shows that the stability of the amorphous state of Sb can be improved dramatically by nanoscale confinement. These as-deposited NPs have a diameter of about 13 nm. In comparison, thin films with a thickness of 10 nm or more are crystalline when deposited at temperature. These preliminary results seem to indicate that, for stabilizing the amorphous phase of Sb, confinement in three dimensions is even more effective than confinement in one dimension.

5.4 Conclusions

For the synthesis of gas-phase Sb NPs with controllable phase states and size, a facile approach based on magnetron-sputtering inert gas condensation was established. By adjusting the discharge current during the deposition, either crystalline or amorphous Sb NPs can be synthesized, and a stable amorphous state at room temperature can be achieved by three-dimensional nanoscale confinement. Furthermore, the morphology and crystalline structure of Sb NPs were characterized by HRTEM and SAED, and the shape difference between the crystalline and amorphous Sb NPs was explained using the theory of diffusion kinetics. The size of as-deposited Sb NPs can be easily tuned by adjustment of the discharge current. Finally, the stability of as-deposited amorphous Sb NPs was studied by in-situ heating in TEM, which clearly demonstrates that the crystallization temperature of Sb can be significantly improved by three-dimensional nanoscale confinement. For NPs with a diameter of about 13 nm the crystallization temperature was found to be in-between 150 and 200 °C.

5

References

(1)   Zhang, W.; Mazzarello, R.; Wuttig, M.; Ma, E. Designing Crystallization in Phase-Change Materials for Universal Memory and Neuro-Inspired Computing. *Nat. Rev. Mater.* **2019**, *4* (3), 150–168.

(2)   Wuttig, M.; Yamada, N. Phase-Change Materials for Rewriteable Data Storage. *Nat. Mater.* **2007**, *6* (11), 824–832.

(3)   Rao, F.; Ding, K.; Zhou, Y.; Zheng, Y.; Xia, M.; Lv, S.; Song, Z.; Feng, S.; Ronneberger, I.; Mazzarello, R.; et al. Reducing the Stochasticity of Crystal Nucleation to Enable Subnanosecond Memory Writing. *Science (80-.).* **2017**, eaao3212.

(4)   Blum, N. A.; Feldman, C. Mössbauer Study of Amorphous and Crystalline Tellurium. *Solid State Commun.* **1974**, *15* (6), 965–968.

(5)   Salinga, M.; Kersting, B.; Ronneberger, I.; Jonnalagadda, V. P.; Vu, X. T.; Le Gallo, M.; Giannopoulos, I.; Cojocaru-Mirédin, O.; Mazzarello, R.; Sebastian, A. Monatomic Phase Change Memory. *Nat. Mater.* **2018**, *17* (8), 681–685.

(6)   Jiao, F.; Chen, B.; Ding, K.; Li, K.; Wang, L.; Zeng, X.; Rao, F. Monatomic 2D Phase-Change Memory for Precise Neuromorphic Computing. *Appl. Mater. Today* **2020**, *20*, 100641.

(7)   Cheng, Z.; Milne, T.; Salter, P.; Kim, J. S.; Humphrey, S.; Booth, M.; Bhaskaran, H. Antimony Thin Films Demonstrate Programmable Optical Nonlinearity. *Sci. Adv.* **2021**, *7* (1), eabd7097.

(8)   Ellison, C. J.; Torkelson, J. M. The Distribution of Glass-Transition Temperatures in Nanoscopically Confined Glass Formers. *Nat. Mater.* **2003**, *2* (10), 695–700.

(9)   Watanabe, K.; Kawasaki, T.; Tanaka, H. Structural Origin of Enhanced Slow Dynamics near a Wall in Glass-Forming Systems. *Nat. Mater.* **2011**, *10* (7), 512–520.

(10)   Zhang, W.; Ma, E. Single-Element Glass to Record Data. *Nat. Mater.* **2018**, *17* (8), 654–655. https://doi.org/10.1038/s41563-018-0114-5.

(11)   Chen, B.; Ten Brink, G. H.; Palasantzas, G.; Kooi, B. J. Size-Dependent and Tunable Crystallization of GeSbTe Phase-Change Nanoparticles. *Sci. Rep.* **2016**, *6* (1), 39546.

(12)   Palmer, R. E.; Cai, R.; Vernieres, J. Synthesis without Solvents: The Cluster (Nanoparticle) Beam Route to Catalysts and Sensors. *Acc. Chem. Res.* **2018**, *51* (9), 2296–2304.

(13)   Zhu, X.; Ten Brink, G. H.; De Graaf, S.; Kooi, B. J.; Palasantzas, G. Gas-Phase Synthesis of Tunable-Size Germanium Nanocrystals by Inert Gas Condensation. *Chem. Mater.* **2020**, *32* (4), 1627–1635.

(14)   Vernieres, J.; Steinhauer, S.; Zhao, J.; Chapelle, A.; Menini, P.; Dufour, N.; Diaz, R. E.; Nordlund, K.; Djurabekova, F.; Grammatikopoulos, P.; et al. Gas Phase Synthesis of Multifunctional Fe-Based Nanocubes. *Adv. Funct. Mater.* **2017**, *27* (11), 1605328.

(15)   Zhao, J.; Baibuz, E.; Vernieres, J.; Grammatikopoulos, P.; Jansson, V.;

5

Nagel, M.; Steinhauer, S.; Sowwan, M.; Kuronen, A.; Nordlund, K.; et al. Formation Mechanism of Fe Nanocubes by Magnetron Sputtering Inert Gas Condensation. *ACS Nano* **2016**, *10* (4), 4684–4694.

(16)   Quesnel, E.; Pauliac-Vaujour, E.; Muffato, V. Modeling Metallic Nanoparticle Synthesis in a Magnetron-Based Nanocluster Source by Gas Condensation of a Sputtered Vapor. *J. Appl. Phys.* **2010**, *107* (5), 054309.

(17)   Hihara, T.; Sumiyama, K. Formation and Size Control of a Ni Cluster by Plasma Gas Condensation. *J. Appl. Phys.* **1998**, *84* (9), 5270–5276.

(18)   Polonskyi, O.; Solař, P.; Kylián, O.; Drábik, M.; Artemenko, A.; Kousal, J.; Hanuš, J.; Pešička, J.; Matolínová, I.; Kolíbalová, E.; et al. Nanocomposite Metal/Plasma Polymer Films Prepared by Means of Gas Aggregation Cluster Source. In *Thin Solid Films*; 2012; Vol. 520, pp 4155–4162.

(19)   Ahadi, A. M.; Zaporojtchenko, V.; Peter, T.; Polonskyi, O.; Strunskus, T.; Faupel, F. Role of Oxygen Admixture in Stabilizing TiOx Nanoparticle Deposition from a Gas Aggregation Source. *J. Nanoparticle Res.* **2013**, *15* (12).

5

SUMMARY

Semiconductor nanoparticles have been intensively researched as functional building blocks in a wide range of fields, including optoelectronic device, data storage, and catalysis, since novel physical and chemical properties could be achieved when the bulk materials are scaled down to the nanoscale. The latter implies that the development of nanoparticles will certainly result in substantial advances in the semiconductor industry. In any case, the intrinsic properties of nanoparticles are dramatically different from the bulk material due to the quantum confinement effect and/or their large surface area.

The quantum confinement effect refers to the fact that electrons and holes in nanocrystals are significantly confined as the size of the nanocrystals is reduced with respect to their Bohr radius, increasing the energy of band-to-band excitation. Furthermore, because spatial confinement may have a significant impact on atom viscosity and relaxation time, the crystalline transition temperature of nanoparticles could be adjusted. Compared with colloidal nanoparticles, the gas-phase nanoparticles offer several advantages, including easy size control, the absence of the side-effect of chemical ligands, and environmental friendliness. In this case, gas-phase semiconductor nanoparticles, which were synthesized by magnetron-sputtering inert gas condensation, were chosen as a desirable three-dimensional (3D) model for studying the size-dependent properties of semiconductor materials in this thesis.

Therefore, in chapter 3, gas-phase Ge NCs were synthesized by the gas aggregation cluster source. The size selection approach is based on adjusting the thickness of copper backing plate to modify the magnetic field configuration above the target surface, which can be illustrated using finite element method modeling. Based on TEM and Raman spectroscopy results, the size of as-deposited Ge NCs decreases with increasing the thickness of copper backing plates. Meanwhile, the crystalline structure of as-deposited Ge NCs

6

was observed by HRTEM and SAED measurements. The Tauc plots based on the results from the UV-vis absorbance measurements indicated the quantum confinement effect on the bandgap of Ge NCs, revealing a bandgap energy that can be controlled by the size of NCs. And, our results closely match the TB model prediction for the bandgap magnitude.

Furthermore, since understanding the electrostatic properties of semiconductor nanocrystals is important for improving the efficiency of quantum dot-based microelectronic devices, in chapter 4, KPFM was utilized to investigate localized electrostatic properties of Ge NCs with different sizes. Specifically, because the decrease of the size of the nanocrystals can be attributed to the increase of the Fermi level for the intrinsic Ge NCs, the number of charges transferred from the substrate to the NCs decreases. The latter reflected a decrease in the measured contact potential difference from KPFM due to the size reduction. Moreover, the experimental results are consistent with the trend of the band energy calculation from the tight-binding theory.

Finally, in Chapter 5, we provide a proof-of-concept that employs three-dimensional nanoscale confinement to stabilize the amorphous phase of Sb. Specifically, a gas-phase routine to produce Sb nanoparticles, (since the nanoparticles can be referred to both crystalline and amorphous spherical nanostructure, nanoparticle is used in this part instead of nanocrystal) with crystallinity and size control is established, which is based on magnetron-sputtering inert gas condensation. The phase states between the crystalline and amorphous as-deposited Sb NPs can be easily tuned by adjusting the sputtering discharge current, and the shape difference between these two phases of Sb NPs was observed by HRTEM. Furthermore, the diameter of as-deposited Sb NPs reduces with decreasing the sputtering discharge current. The stability of the amorphous Sb NPs were characterized by in-suit heating in TEM, which demonstrates that the stability of the amorphous state for Sb can be significantly improved by scaling down into nanoscales.

6

SAMENVATTING

Halfgeleider nanodeeltjes zijn intensief onderzocht als functionele bouwstenen in een breed scala aan toepassingen zoals opto-elektronische apparaten, dataopslag en katalyse omdat er nieuwe fysische en chemische eigenschappen bereikt kunnen worden wanneer de bulkmaterialen worden verkleind tot de nanoschaal. Het laatste impliceert dat de ontwikkeling van nanodeeltjes zeker zal leiden tot substantiële vooruitgang in de halfgeleider industrie. In ieder geval zullen de intrinsieke eigenschappen van nanodeeltjes dramatisch verschillen van het bulkmateriaal vanwege het kwantum opsluitingseffect en/of hun grote oppervlak.

Het kwantum opsluitingseffect refereert naar het feit dat elektronen en elektrongaten in nanokristallen aanzienlijk worden ingesloten naarmate de grootte van de nanokristallen kleiner wordt met betrekking tot hun Bohr-straal waardoor de bandkloof toeneemt. Bovendien, omdat ruimtelijke opsluiting een significante invloed kan hebben op atoomviscositeit en relaxatietijd, is de kristallijne transitie temperatuur van de nanodeeltjes veranderd. Vergeleken met colloïdale nanodeeltjes, hebben de gas-fase geproduceerde nanodeeltjes verschillende voordelen waaronder makkelijke grootteregeling, de afwezigheid van de bijwerking van chemische liganden, en het milieuvriendelijkere aspect. In dit proefschrift, de in gas-fase geproduceerde, halfgeleider nanodeeltjes, gemaakt door middel van inert gas magnetronsputter condensatie, zijn gekozen als een geschikt, driedimensionaal model voor het bestuderen van de grootte afhankelijke eigenschappen van halfgeleider materialen.

In hoofdstuk 3 is daarom uitgelegd hoe de Ge nanokristallen gemaakt zijn door middel van de gasaggregatieclusterbron. De grootte van de kristallen is veranderd door het aanpassen van de dikte van een koperen onderplaat om het magnetische veld boven het target oppervlak te beïnvloeden, wat geïllustreerd kan worden met behulp van de eindige-elementenmethode. Met behulp van transmissie elektronenmicroscopie en Raman spectroscopie kan

6

geconcludeerd worden dat de grootte van, de zoals gedeponeerde, Ge nanokristallen afneemt naar mate de dikte van de onderplaat toeneemt. Ondertussen is de kristallijne structuur van de nanokristallen onderzocht met hoge resolutie transmissie elektronenmicroscopie en geselecteerde gebiedsdiffractie. Tauc plots gebaseerd op de resultaten van UV/VIS-spectrofotometrie gaven aan dat het kwantum opsluitingseffect zeker een invloed had op de bandkloof van de Ge nanokristallen, afhankelijk van de grootte van de nanokristallen. De resultaten komen nauw overeen met voorspellingen van het sterke binding model (tight-binding model) voor de bandkloof grootte.

Bovendien, omdat het begrijpen van de elektrostatische eigenschappen van halfgeleider nanokristallen belangrijk is voor het verbeteren van de efficiëntie van kwantum-dot gebaseerde micro-elektrische apparaten, is Kelvin probe kracht microscopie (KPFM) in hoofdstuk 4 gebruikt om gelokaliseerde elektrostatische eigenschappen van de, verschillend in grootte, Ge nanokristallen te onderzoeken. In het specifiek zijn het aantal ladingen die zijn overgedragen van het substraat naar de nanokristallen onderzocht. Door de afname van de grootte van de nanokristallen neemt Fermi-niveau van de Ge nanokristallen toe en daardoor neemt het aantal ladingen die worden overgedragen tussen het substraat en de nanokristallen af. Dit weerspiegelt zich als een afname in het gemeten contactpotentiaalverschil van de KPFM als gevolg van de afname in grootte van de nanokristallen. Ook zijn deze experimentele resultaten consistent met de berekeningen van de band energie aan de hand van het tight-binding model.

Ten slotte wordt er in hoofdstuk 5 een proof of concept aangeboden dat driedimensionale opsluiting op de nanoschaal gebruikt om de amorfe fase van Sb te stabiliseren. Specifiek wordt er een routine aangeboden om Sb nanodeeltjes te produceren (omdat de bolvormig gestructureerde nanodeeltjes beide kristallijn en amorf genoemd kunnen worden wordt nu 'nanodeeltje' gebruikt in plaats van 'nanokristal'). Deze nanodeeltjes worden, met hoge

6

beheersing van de kristalliniteit en grootte, gemaakt met het in inert gas condensatie magnetronsputteren. De fases van de nanodeeltjes kunnen makkelijk aangepast worden door het aanpassen van de ontladingsstroom die nodig is voor het sputteren. Vervolgens is met hoge resolutie transmissie elektronenmicroscopie het verschil in vorm van de nanodeeltjes in de verschillende fases bekeken. Bovendien neemt de grootte van de nanodeeltjes af met een afnemende ontladingsstroom. De stabiliteit van de Sb nanodeeltjes is geanalyseerd door middel van ter plaatse verhitting in de transmissie elektronenmicroscoop. Het demonstreert dat de stabiliteit van de amorfe fase van de Sb nanodeeltjes significant verbetert door het schalen naar het nanoregime.

6

6

Acknowledgements

First of all, I would like to convey the appreciation to my supervisor, Prof. George Palasantzas, for your mentoring and guiding during my PhD journey. When I was trying to apply the CSC scholarship, I was very impressed by your prompt reply and support. From then on, I knew that I could rely on you for any difficulties, not only from research, but also from my daily life, which proved that I was right after these four years. Under your supervision, I try to enter into a field without any background knowledge before. With your encouragement, I gradually build up my own confidence and experience in this field. In addition, I am very grateful that you always gave me freedom for the research. I learned quite a lot from you. Thank you very much.

Secondly, I would like to thank my second supervisor, Prof. Bart J. Kooi. I am very grateful for your suggestion about my research and comments for my papers. Also, the discussion about TEM with you always help me to understand the hard theory behind it. Moreover, I am very impressed about your breadth of knowledge, which also encourage me to explore some unknow field. Thank you very much.

And then, many thanks go to Gert, who help me to solve countless technical problems. Also, I appreciate the discussion not only about research but also culture difference between us. Moreover, I would like to thank Sytze, who also give me a big support for TEM learning. Also, I pretty like to discuss with you and can gain a lot of benefits after discussion with you.

I would like thank the assessment committee members: Prof. Meike Stöhr (RUG), Prof. Maria Antonietta Loi (RUG), Prof. Harold Zandvliet (UT), for going through my thesis and your kind suggestions and comments.

I would like thank all the members in Nanostructure Materials and Interface Group. Firstly, I would like to thank Chinese colleagues in the group: Bin, Lijuan, Xukai, Weiteng, Heng, Hui for their encourage, experience sharing and talks when I feel sad. And then, many thanks to Julien for helping me translate the Dutch summary of my thesis. Finally, I would like to thank Jamo, Paul,

Xiaotian Zhu

Groningen

August, 2021